CHARACTERIZATION OF THE NEAR-PLUME REGION

OF A LOW-CURRENT HOLLOW CATHODE

by

Daniel Joseph Asselin

A Thesis

Submitted to the Faculty

of the

WORCESTER POLYTECHNIC INSTITUTE

in partial fulfillment of the requirements for the

Degree of Master of Science

in

Mechanical Engineering

April 2011

APPROVED:

_____

Dr. John J. Blandino, Advisor
Associate Professor, Mechanical Engineering Department

_____

Dr. Nikolaos A. Gatsonis, Committee Member
Professor, Mechanical Engineering Department

_____

Dr. David J. Olinger, Committee Member
Associate Professor, Mechanical Engineering Department

_____

Mr. Bruce Pote, Committee Member
Busek Co., Inc., Natick, MA

_____

Dr. Simon W. Evans, Committee Member
Assistant Professor, Mechanical Engineering Department

_____

Dr. Mark W. Richman, Graduate Committee Representative
Associate Professor, Mechanical Engineering Department

Abstract

Electric propulsion for spacecraft has become increasingly commonplace in recent decades as designers take advantage of the significant propellant savings it can provide over traditional chemical propulsion. As electric propulsion systems are designed for very low thrust, the operational time required over the course of an entire mission is often quite long. The two most common types of electric thrusters both use hollow cathodes as electron emitters in the process of ionizing the propellant gas. These cathodes are one of the main life-limiting components of both ion and Hall thrusters designed to operate for tens of thousands of hours. Failure often occurs as a result of erosion by sputtering from high-energy ions generated in the plasma. The mechanism that is responsible for creating these high-energy ions is not well understood, and significant efforts have gone into characterizing the plasma produced by hollow cathodes.

This work uses both a Langmuir probe and an emissive probe to characterize the variation of the plasma potential and density, the electron temperature, and the electron energy distribution function in the near plume region of a hollow cathode. The cathode used in this experiment is typical of one used in a 200-W class Hall thruster. Measurements were made to determine the variation of these parameters with radial position from the cathode orifice. Changes associated with varying the propellant and flow rate were also investigated.

Results obtained from the cathode while running on both argon and xenon are shown. Two different methods for calculating the plasma density and electron temperature were used and are compared. The density and temperature were not strongly affected by reductions in the propellant flow rate. The electron energy distribution functions showed distinct shifts toward

higher energies when the cathode was operated at lower flow rates. The plasma potential also displayed an abrupt change in magnitude near the cathode centerline. Significant increases in the magnitude of plasma potential oscillations at lower propellant flow rates were observed. Ions formed at the highest instantaneous plasma potentials may be responsible for the life-limiting erosion that is observed during long-duration operation of hollow cathodes.

Acknowledgements

The following individuals deserve special recognition for making the completion of this thesis possible.

My thesis advisor, Prof. John Blandino, for his guidance and assistance throughout my six years at WPI. His remarkable skill and virtually limitless patience as an educator and research advisor were directly responsible for the success of this work and my academic development.

All of the members of my thesis committee for their time and willingness to help guide my research.

Nick Behlman, for getting me started in this research and providing a solid foundation on which to expand it.

Busek, Co., Inc. for supplying the cathode used in this experiment.

Bruce Pote and the engineering and technical staff at Busek for their work in keeping this experiment running and troubleshooting the many problems that arose.

Dan Goebel of the Jet Propulsion Laboratory, for his electronics and data acquisition expertise.

Barbara Furhman for her expert handling of the many purchase orders submitted throughout this project.

Worcester Polytechnic Institute, for supporting me through six years and two degrees.

Table of Contents

List of Figures

List of Tables

1 Introduction

1.1 Overview of Electric Propulsion

In any plan for a space mission, one of the primary design drivers is the velocity change that must be imparted to the spacecraft to reach its intended destination. For any propulsion system, this number will dictate the amount of propellant to be carried, the size and mass of the propellant tanks and distribution hardware, and consequently the total mass that must be launched into space. The launch mass, in turn, drives the selection of a booster with sufficient performance to meet the mission requirements. As larger boosters are inherently more expensive to procure, it is in the interest of any spacecraft designer to reduce the spacecraft launch mass as much as possible.

From a mass-utilization standpoint, traditional chemical propulsion systems are inefficient when compared to electric thrusters. While they are capable of producing a large ΔV very quickly, a large quantity of propellant is required. In contrast, electric thrusters use far less propellant to produce the same change in velocity but do so much more slowly as a result of the much lower thrusts that they produce. In space, however, this small thrust, applied over many months or years, is sufficient to achieve a ΔV much greater than that achievable with any chemical propulsion system. As a result, many previously impractical mission designs have become possible through the mass savings that electric propulsion enables [1]

The thrust of a rocket engine may be calculated by Equation (1), which states that the thrust is equal to the product of the mass flow rate of propellants through the engine and a quantity called the equivalent exhaust velocity. (The equivalent exhaust velocity incorporates the thrust contribution from pressure effects acting on the engine.)

$$T = \dot{m}c \qquad (1)$$

A commonly used measure of efficiency for rocket engines is the specific impulse, defined as the ratio of the impulse delivered to a vehicle to the weight of the propellant consumed in the process. The most efficient chemical rocket engines have a specific impulse of about 450 s., while one class of electric thrusters routinely achieves 3,000 s. and higher. Specific impulse is related to the equivalent exhaust velocity by the following equation, where I_t is the total impulse, w_p is the weight of the propellant consumed, $\dot{w}_p$ is the weight flow rate of the propellant, and g is the acceleration due to gravity on Earth [2].

$$I_{sp} = \frac{I_t}{w_p} = \frac{T}{\dot{w}_p} = \frac{\dot{m}c}{\dot{m}g} = \frac{c}{g} \qquad (2)$$

This shows that thrusters with higher values of specific impulse also have higher exhaust velocities. For a fixed quantity of propellant, the only way to increase the impulse supplied to the spacecraft is to increase the exhaust velocity. Thrusters that employ a chemical reaction to accelerate the exhaust gases have a theoretical maximum exhaust velocity, which is limited by the energy released in the combustion process. In contrast, electric thrusters use electricity to achieve a very high exhaust velocity and hence I_{sp}.

Many type of electric thrusters have been developed that rely on a variety of methods for producing thrust. These fall into several broad categories, including electrothermal, electrostatic, and electromagnetic, referring to the method used to accelerate the propellant. Among electrostatic thrusters are two common types, ion thrusters and Hall thrusters, that ionize and accelerate the propellant, typically xenon, to produce thrust [1].

Ion thrusters contain a system for ionizing the propellant and creating the plasma, typically by electron bombardment, a system of grids for accelerating the ions out of the thruster

to produce thrust, and a neutralizer cathode that emits electrons outside the thruster in order to neutralize the space charge in the plume and to avoid the buildup of electrical charges on the spacecraft. One of the first successful uses of ion thrusters for primary spacecraft propulsion was on the Deep Space 1 (DS-1) mission, a technology-demonstration project developed by NASA and launched in 1998. Among electric thrusters, ion thrusters are highly efficient and offer very high values of I_{sp}. A schematic showing the principal features of a typical ion thruster appears in Figure 1 below [1].

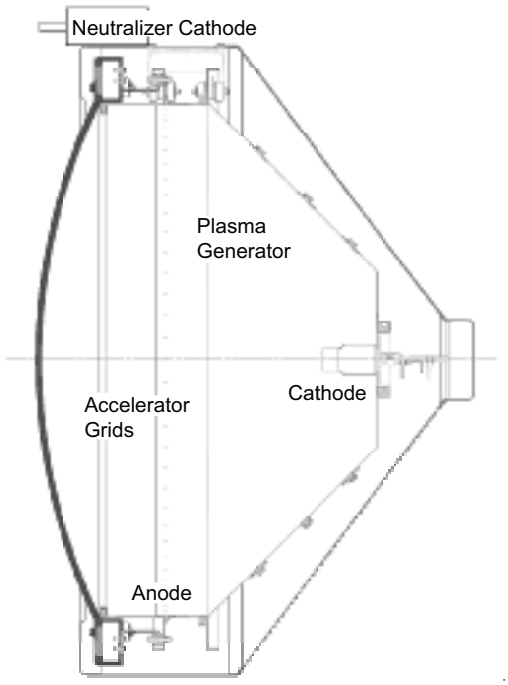

Figure 1: Cross-Section of an Ion Thruster [1]

Hall thrusters use a somewhat different configuration to produce and accelerate the ionized gas. They are simpler in construction and operation than ion thrusters and produce higher thrust for a given power level. This comes, however, at the expense of specific impulse and efficiency. In a Hall thruster, the propellant is injected through an annular anode where it is ionized by electron bombardment. The electrons themselves are trapped axially in the thruster by the application of a transverse magnetic field. This increases their residence time in the discharge

region and creates a region where local space charge produces an axial electric field. The ions are then accelerated out of the thruster to produce thrust. The main features of a Hall thruster are illustrated in Figure 2 below [1].

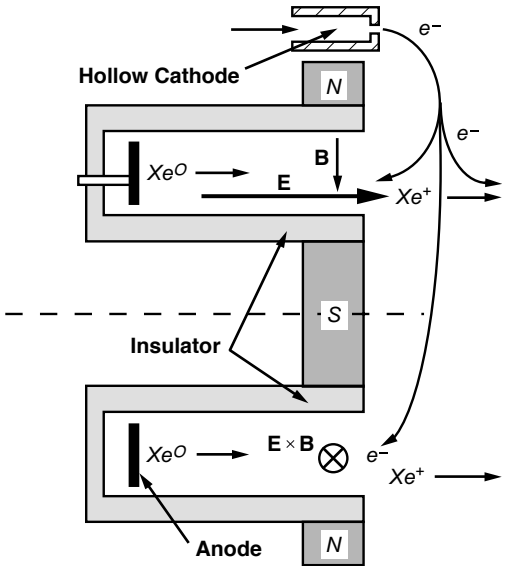

Figure 2: Cross-Section of a Hall Thruster [1]

1.2 Hollow Cathodes

1.2.1 Operation

In both ion and Hall thrusters, the most common method used to ionize the propellant is electron bombardment. Naturally, this requires an electron source. Ion thrusters also require a second electron source to neutralize the ions as they leave the thruster. In both cases, a hollow cathode is the usual choice.

During the early development work on electric thrusters, simple tungsten filaments were used as the electron source. Unfortunately, this choice suffers from several drawbacks. Firstly, tungsten has a relatively high work function. Thermionic electron emission can be predicted by the Richardson-Dushman equation, given below [1].

$$J = AT^2 \exp\left(\frac{-e\phi}{k_B T}\right) \qquad (3)$$

Here, J is the emitted current density, T is the temperature of the emitter, e is the elementary charge, ϕ is the work function of the material, k_B is Boltzmann's constant, and A is a constant with a theoretical value of $120 \frac{A}{cm^2 K^2}$. As work function increases, higher temperatures are needed to achieve sufficient electron emission. For a tungsten filament, this requires relatively high heater power, which has a deleterious effect on the thruster efficiency.

Secondly, the filament has a tendency to evaporate at these high operating temperatures, shortening its useful life and consequently the operating lifetime of the thruster. The tungsten can also be damaged by sputtering from ions in the thruster beam. For deep space missions that require thruster operating times on the order of many months to years, the reliability of tungsten-wire emitters was insufficient [1].

A more efficient and longer-lasting choice for electron emitters is the hollow cathode. Shown in Figure 3, a hollow cathode has several distinguishing features.

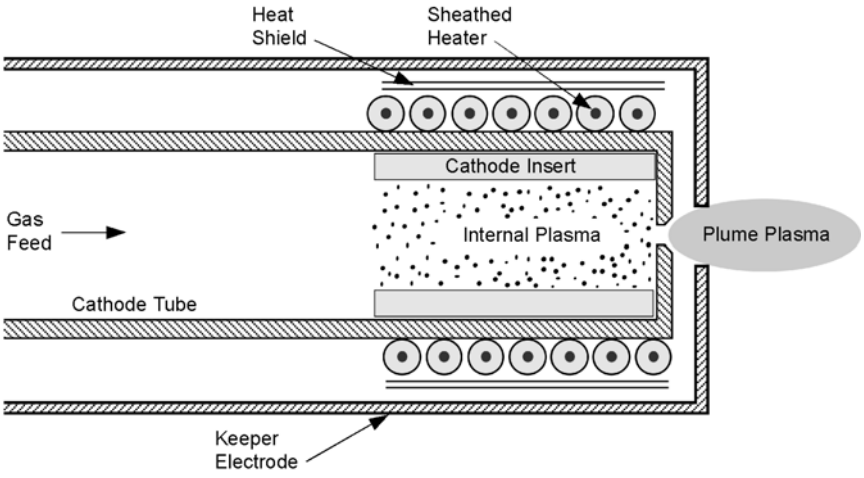

Figure 3: Schematic of a Hollow Cathode [1]

The emitter takes the form of a cathode insert, which can be composed of a low work function material for improved efficiency. A common design for so-called dispenser cathodes is the use of an insert consisting of a porous tungsten matrix impregnated with a mixture of barium oxide. For example, a 411-BaO-W cathode would consist of barium, oxygen, and tungsten in the molar ratio of 4:1:1. This cathode has a work function of about 2 eV at temperatures in excess of 800°C [1]. The insert is located inside a hollow tube (called a cathode tube), through which the propellant is introduced. The insert is raised to a temperature sufficient for electron emission by a heater coil that is wrapped around it. While this configuration is sufficient for the operation of a hollow cathode, the cathode is often surrounded by another electrode called the keeper. The keeper is biased with a positive potential and serves to protect the cathode body from sputtering from high-energy ions. It also enables the cathode to be started by striking a discharge between the insert plasma and the keeper electrode [1].

Unlike tungsten filaments, there is no need to maintain continuous heating of the cathode insert via an external power supply. Instead, the plasma discharge in hollow cathodes is self-heating. There are three primary mechanisms through which this can occur. The first, primarily

relevant to low-current cathodes with a small orifice, is orifice heating. The small orifice increases the gas pressure inside the cathode insert which also increases the resistance to the discharge passing through the orifice. This leads to a large amount of the discharge power being transferred to the orifice walls and eventually back to the insert itself. In most cathodes, ion heating is the primary means of sustaining the electron discharge. With this mechanism, ions in the insert region bombard the insert surface, maintaining a sufficiently high emitter temperature. In cathodes with very high plasma densities, sufficiently energetic electrons in the tail of the energy distribution exist which are capable of reaching the insert surface directly. This last mechanism is known as electron heating [1].

Cathodes operate in two characteristic modes, known as spot mode and plume mode. The former is quiescent and is characterized by relatively low oscillations in the plasma potential. Spot mode is named for the recognizable bright "spot" that is located some distance downstream from the emitter orifice. As the propellant flow rate is reduced for a given discharge current, the cathode begins to transition to the plume mode. This mode is avoided in operation because it is noisier, with larger plasma potential fluctuations that can manifest themselves in the cathode power supplies. Visually, the plasma spot moves back towards the cathode orifice, and the plasma forms a widely-diverging cone [1]. There is no abrupt transition between the modes; rather, the transition is continuous.

1.2.2 Prior Work

Because hollow cathodes are a central component of many common electric thruster designs, they have been the subject of extensive research at many institutions. Longer-duration missions will require thrusters capable of operating without interruption for many months or

years. Consequently, much research has been devoted to gaining an understanding of how cathodes fail.

Deep Space 1 (DS-1) was NASA's first effort to launch an operational ion thruster as the main propulsion system for a spacecraft. As part of the thruster development program associated with DS-1, a flight spare ion engine for that mission was installed in a vacuum chamber at the Jet Propulsion Laboratory and left operating nearly continuously for a period totaling 30,352 hours. The test was ultimately ended in order to perform destructive analyses of the engine. Among the many components that were evaluated during the test were both the discharge cathode and the neutralizer cathode.

The discharge cathode is responsible for producing the electron current that ionizes the xenon propellant. During the extended life test, significant erosion of the keeper electrode was observed, beginning with pitting after approximately 5,000 hours of operation. Erosion continued, eventually exposing the entire cathode orifice plate and heater, at all power levels except the very lowest thrust setting. This damage is shown in Figure 4. A short circuit between the keeper electrode and the cathode body also appeared during the test, leading to a rapid increase in the keeper erosion rate [3].

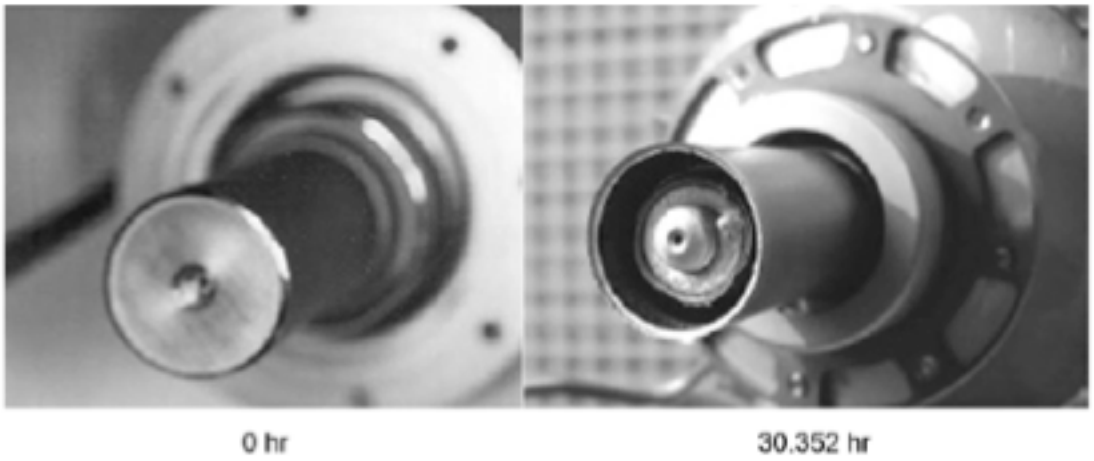

Figure 4: Keeper Erosion During DS-1 Extended Life Test [3]

Many explanations for this behavior have been proposed. Most focus on the production of high-energy ions that are able to penetrate the sheath surrounding the keeper electrode. Some mechanisms for the production of these ions include the formation of higher plasma potential "hills," charge exchange between ions and neutrals, multiple ionizations of the propellant atoms, and oscillations in the plasma potential that permit higher-energy ions to be produced [4].

Research at the Jet Propulsion Laboratory has attempted to address the source of these high-energy ions. It is well known that cathodes can operate in at least two distinct modes. The first, known as spot mode, is characterized by quiescent operation. The plasma potential is relatively stable and signals from probes inserted in the plasma contain relatively little noise. If the cathode is required to source excessive discharge current for a given propellant flow rate, or if the flow rate is low for a given current, large oscillations in the plasma potential and in probe signals can be observed [5]. Operation in this so-called "plume mode" can produce ions that have energies well above the discharge voltage. Although the life tests avoided operation in plume mode, it is theorized that these high-energy ions, produced as a result of large potential fluctuations, are largely responsible for the rapid keeper erosion observed in extended life tests.

In a series of tests designed to explore the origins of these energetic ions, a radially scanning emissive probe was employed to measure the plasma potential variations in the near-keeper plasma generated in both an NSTAR thruster and a NEXIS thruster. This probe was mounted on a pneumatic plunger to allow it to move rapidly through the plume region of the plasma. The emissive probe was operated in the floating mode, in which the floating potential of the emissive probe approaches the plasma potential as strong thermionic electron emission is reached [5]. In addition to the emissive probe, a retarding potential analyzer (RPA) was used to measure the ion energy directly. Two throttle settings were considered for the NSTAR thruster, one at 8.2 A and 26 V and the other at 13.1 A and 25.5 V. The NEXIS thruster was primarily operated at 25 A and 26 V.

Results from the RPA showed that relatively few high-energy ions were produced in the axial direction, directly downstream from the cathode orifice plate. In contrast, however, very large peaks in the ion energy distribution were observed in the radial direction at energies significantly in excess of the discharge voltage [5]. Increasing the discharge current resulted in a large increase in the number of high-energy ions produced, including those with energies sufficient to cause the observed keeper electrode erosion by sputtering.

The plasma potential was measured both inside and outside of the cathode using a scanning Langmuir probe. For the highest current setting, the plasma potential was on the order of 6 V for a 25-V discharge voltage. Outside the cathode orifice, the potential had increased to approximately 12-14 V and continued to increase to the anode potential axially downstream of the orifice. Electron temperature showed little variation with axial position. Density was found to be very high in the insert region ($>10^{15}$ cm^{-3}) and to increase with increased discharge current [5]. Furthermore, increased discharge current has the added effect of moving the location of

maximum density further downstream away from the orifice. Density decreases rapidly in both the axial and radial directions. Measurements from the emissive probe showed that the plasma potential actually reaches a minimum immediately downstream of the cathode orifice. No evidence of a potential hill, thought to be one of the possible mechanisms for the production of high-energy ions, was found. In fact, ions produced in the region just downstream of the orifice, despite their tendency to backstream toward the keeper electrode, would have insufficient energy (<20 eV) to produce the observed erosion rates [5].

The emissive probe was also used to investigate whether oscillations in the plasma potential could produce sufficiently energetic ions to explain the high erosion rates. This probe also observed the plasma potential minimum just downstream of the cathode exit. Moving radially, the plasma potential was observed to increase to values above the discharge voltage before decreasing back to the anode potential near the wall. Oscillations in the measured plasma potential were found to be in the range 50-500 kHz. The magnitude of these oscillations was approximately ±5 V on axis, increasing to ±20 V one cm from the axis. Higher discharge currents increased the magnitude of these oscillations [5]. It is thought that these fluctuations are related to turbulent ion acoustic waves or ionization instabilities.

It is possible to estimate the frequency of any ionization instabilities if the ionization cross-sections for the propellant gas are known. These are well documented for xenon. The rate of ion production is given by Equation (4), which provides an estimate for the frequency of the ionization instability. This approximation is given by Equation (5).

$$\frac{dn_i}{dt} = n_e n_o < \sigma v_e > \qquad (4)$$

$$f \approx \frac{n_e < \sigma v_e >}{\left(n_i / n_0\right)} \qquad (5)$$

where n_e is the electron density, σ is the ionization cross section, v_e is the electron velocity, and n_i / n_0 is the ionization fraction. Here, the brackets indicate that the term enclosed is to be averaged over the distribution function. For the cathodes studied in the JPL research, an ionization fraction of 10%-50% was observed, corresponding to an ionization frequency of approximately 80 kHz. These data correlate well with the frequencies observed in the plasma potential oscillations [5].

These ionization instabilities are often referred to as predator-prey oscillations. As ionization occurs, the available neutral gas density becomes depleted. This causes a concurrent decrease in the plasma density and the electron flux. As a result, neutral gas can again reach the ionization region, where the ionization rate increases once more until the available gas is depleted. This process repeats. The result is fluctuations in the plasma potential and discharge current [6].

A second possible explanation for the production of ions with energies significantly in excess of the steady-state plasma potential is that of charge-exchange collisions between ions and neutrals. Because the plasma potential has been observed to reach a minimum on the cathode centerline, ions are able to gain energy by falling down this potential gradient [7]. If a charge-exchange collision occurs at the minimum value of this potential well, the resulting neutral particle will be able to move to higher-potential regions of the plasma without further loss of kinetic energy. If the neutral is then reionized in one of these high-potential regions, the possibility exists for the generation of ions with much greater energies [7]. Figure 5 is a schematic representing this process.

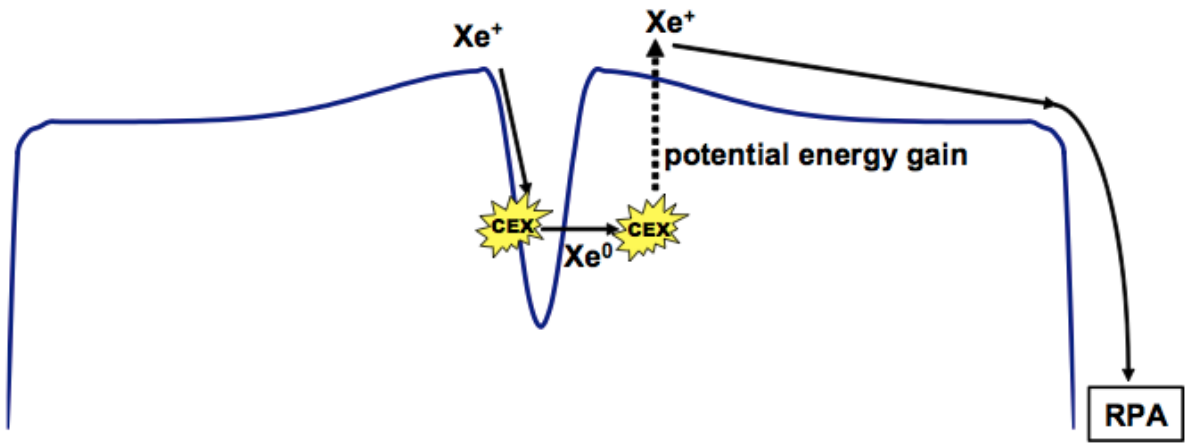

Figure 5: Charge Exchange Ion Production [7]

Despite the success achieved with the use of these experimental techniques, there are some regions of the plasma that cannot be studied reliably through the use of traditional probes. One of the most important is the orifice itself. During the NSTAR thruster extended life test, the neutralizer cathode orifice was found to have eroded to nearly twice its original diameter [3]. This form of erosion, like those associated with the keeper electrode and orifice plate, can also cause the failure of the cathode. It is possible for sputtering products to become lodged in the orifice, blocking the flow of the propellant gas. Very advanced wear of the orifice can contribute to short circuits between the keeper electrode and the cathode common. Finally, there is the added risk that changes in the orifice geometry may lead to performance problems for the cathode. These problems might range from manageable losses of efficiency to more severe operation in the plume mode, which leads to much higher erosion rates and more rapid failure of the cathode [4]. Consequently, an understanding of the behavior of the plasma in the orifice region is important to designing cathodes that are more resistant to the processes that contribute to erosion and hardware failure. Unfortunately, the diameter of the cathode orifice is often too small to make traditional probe diagnostics of the plasma. A photograph showing the orifice

geometry after approximately 8,200 hours of operation compared to its original dimensions is shown below in Figure 6 [4].

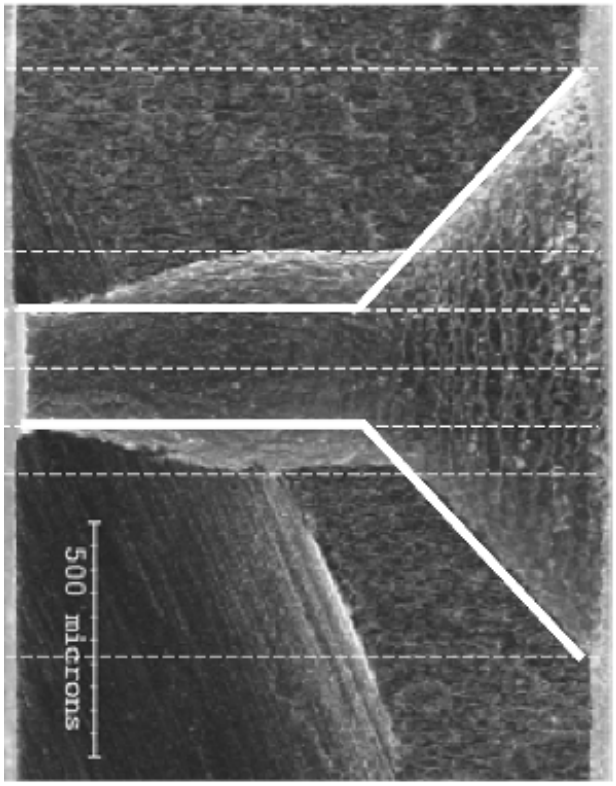

Figure 6: Cathode Orifice Geometry, Before and After 8,200-hour Life Test [4]

Ioannis Mikellides et al. at the Jet Propulsion Laboratory have embarked on an extensive effort to model the behavior of the plasma in this region using numerical simulations [4]. The simulations consist of a two-dimensional model that includes electrons, neutral gas atoms, and singly charged ions. The model solves the continuity, momentum, and energy conservation equations for the electrons and ions. From these, it is possible to obtain the particle densities, the electron temperature, and the plasma potential [4].

The primary driver of the production of high-energy ions is the plasma potential. Because the extent of the orifice erosion increases along the channel, it is theorized that the potential must also increase along this path. The plasma potential rise is primarily caused by the interaction of

two competing forces. One is the electron resistance caused by the presence of an electric field, and the other is the neutral pressure-gradient force. The resistive heating experienced in the channel strongly influences plasma potential and the maximum energy of the ions that can be produced in the region. The maximum value of the plasma potential occurs at the point where these two forces balance [4].

Erosion rates are computed using experimentally-derived sputtering yields for a tungsten electron emitter insert. Results of the simulations indicate that the majority of the erosion occurred in the first few thousand hours of operation. As the erosion proceeded and enlarged the orifice channel, it is theorized that the current density was reduced, causing a concomitant reduction in the electric field and a decrease in the plasma potential. The ions generated in this region, now less energetic, were unable to produce the high erosion rates observed with a narrower channel [4]. This decrease in energy led to a decrease in the sputtering yield of approximately three orders of magnitude, reducing erosion rates to negligible levels.

It is important to note that this erosion behavior was observed only in the much smaller neutralizer cathode and not in the discharge cathode. The discharge cathode's orifice is 3.5 times larger than that used on the neutralizer cathode, reducing the current density sufficiently to make ion sputtering of the insert surface insignificant [4].

Research conducted at the University of Michigan has investigated one of NASA's newest thrusters, the NEXT ion thruster. NEXT has been designed to produce twice the thrust of the previous generation NSTAR thruster, used on Deep Space 1 [8]. It was also designed to equal NSTAR's operating lifetime. The purpose of the work by Herman and Gallimore was to obtain electron energy distribution functions in several regions of the thruster, in an effort to determine

the mechanisms causing discharge cathode erosion. The NEXT thruster was operated at approximately 25 V discharge voltage and at discharge currents ranging from 7-19 A.

The specific Langmuir probe used in this research is known as the HARP—the high-speed axial reciprocating probe. This system uses servo motors to move probes at speeds up to 250 cm/s. This allows the residence time of the probe inside the discharge to be maintained under 100 ms in order to prevent probe heating and self-emission [8]. The thruster itself is moved relative to the probe on a translation table.

The electron energy distribution function was computed using two methods. The first is the Druyvesteyn method, which relates the second-derivative of the probe characteristic curve to the distribution function and will be discussed in section 2.1.4. Because numerical differentiation is a noisy process, many runs were averaged together to reduce the error [8]. Another method that does not rely on numerical processing of the collected probe data is called the harmonic method. This method superimposes a small alternating current signal on the probe voltage. The increase in the DC current caused by this added signal is proportional to the second derivative, which allows direct calculation of the data needed to use the Druyvesteyn formula [8]. When calculating the second derivative of the probe trace numerically, a boxcar moving average smoothing algorithm was applied to the raw signal and after the first and second derivatives are computed [8].

In practice, the Druyvesteyn method and the harmonic method produced comparable results for the electron energy distribution functions. The structure of the discharge was found to be such that the low-potential cathode plume transitions to the higher potential bulk plasma with a double layer gradient structure. Electron temperatures in the plume were approximately 2-4 eV. Outside the plume, the electron temperature increases up to 7 eV. The variation of the plasma

potential with radial position was much more abrupt and contained larger gradients than similar measurements made in the axial direction. Cases were considered both with and without ion beam extraction. In the discharge only mode, without beam extraction, the EEDFs contain a single peak at energies of 5-8 eV. In the bulk plasma, the high-energy tail of the distribution function becomes more pronounced [8]. With beam extraction active, this high-energy tail becomes broader, perhaps due to higher discharge voltage oscillations which drive fluctuations in the double layer potential gradient. Axial acceleration of the electrons is observed in the form of a shift to higher energies. In the region of the double-layer potential gradient, a twin-peak distribution is observed, which is not seen without beam extraction [8].

As the computation of the electron energy distribution is important for analysis of the conditions in the plasma, significant work has been devoted to optimizing numerical schemes for the calculation of the second-derivative of the Langmuir probe I-V characteristic. Sawlani and Foster provide a summary of many of the most widely-used techniques [9]. When applying any sort of numerical differentiation, one must take care that the data processing does not mask or otherwise obscure physical features of the EEDF. It is noted that the selection of the smoothing parameters in large part relies on the experience of the analyst to achieve sufficient smoothing without sacrificing important information.

The Savitzky-Golay method has been widely applied in many different applications. This method performs a least-squares polynomial fit to a subset of the data points. The smoothed point is then given by the central point of the calculated polynomial. This process is repeated at each point to be smoothed [9]. For noise reduction, this method is not ideal.

Hayden's method has also been considered for processing of Langmuir probe data. This method attempts to correlate more closely the processed data with the performance of the

measuring instrument. An “instrument function” is defined for the response of the instrument. This function, which is not straightforward to determine, can then be convolved with the measured signal to eliminate some error in the measurement. Because the instrument function is difficult to determine in practice, a Gaussian filter is often assumed [9].

Windowing methods seek to divide a signal into segments over which a smooth periodic function can be fit. Essentially, these functions serve as weights which seek to moderate the excursions caused by the presence of noise in the signal. Many choices for the periodic weighting function are available—a general cosine function is among the most common [9].

Simple polynomial fitting can also be used for smoothing. In contrast to the Savitzky-Golay method, which considers small portions of the data set and performs a least-squares regression analysis for each, general polynomial fitting considers the data set as a whole. Despite this method’s ease of application, it is not ideal for Langmuir probe as accurate reproduction of the signal cannot be achieved [9].

Finally, the free four parameter fitting method seeks to determine four variables that will define the shape of the curve. This method attempts to fit an exponential transformation of a hyperbolic tangent function to the Langmuir probe trace. Unfortunately, the four parameters needed to define the curve are not simple to determine accurately. Trial and error may be necessary to determine how to fit a particular dataset accurately. This makes automation of the processing steps difficult [9].

The research described in this thesis owes its genesis to that begun by Nicholas Behlman in 2007 [10]. The initial experimental setup included a Langmuir probe driven by a Keithley 2410 sourcemeter. The Druyvesteyn method was applied to the I-V characteristics obtained from this instrument to calculate the electron energy distribution function. These were calculated for a

range of radial positions and two discharge current conditions. From the EEDF, the electron temperature and plasma density were also calculated. The EEDF was also compared to both the Maxwellian and Druyvesteyn distributions, which will be discussed in section 1.4. Close to the cathode orifice, the Druyvesteyn distribution was found to be a better description for the electron population. Far from the centerline, the deviation from the Druyvesteyn distribution was found to increase significantly, with a larger proportion of high-energy electrons being present in the tail of the distribution [10]. This result was confirmed by measurements of the electron temperature, which also tended to increase with radial distance from the orifice. The measured distribution function, compared to the Maxwellian and Druyvesteyn distributions for the same mean temperature, are shown in Figure 7 below. This figure shows the deviation from the Druyvesteyn and shift toward higher energies as radial distance increases [10]. The leftmost curve was measured at the centerline and the two others at two off-axis positions.

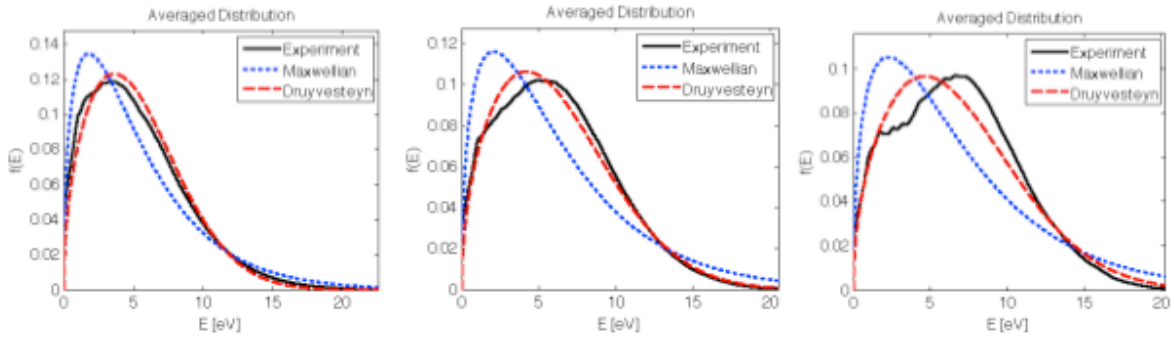

Figure 7: Comparison of Measured EEDF to Maxwellian and Druyvesteyn Distributions for Several Radial Positions (left: 0 mm (centerline), middle: 6.5 mm, right: 10.7 mm) [10]

1.3 Characteristics of Plasmas

The plasma produced in electrostatic thrusters consists of a collection of electrons, neutral gas particles, and positively charged ions. Plasmas are sometimes considered a distinct state of matter and have many unique properties that differentiate them from ordinary neutral

matter. Among these is the concept of collective behavior. While an ordinary neutral gas molecule can interact with its surroundings and other gas molecules only over short ranges through collisions, charged particles produce electromagnetic fields that can influence the motion of other charged particles over very long distances.

Secondly, plasmas exhibit a property known as quasi-neutrality. Over sufficiently long length scales, the plasma behaves as if it were electrically neutral. The number densities of electrons and positive ions (in a sufficiently large volume) are approximately equal ($n_e \approx n_i$). Furthermore, plasmas are able to shield the electromagnetic effects of individual free electric charges or charged surfaces. For example, if a positive charge is placed in a plasma, negative charges will be attracted to it and positive charges repelled. The increased negative space charge in the vicinity of the added charge serves to cancel the electric field that would otherwise be generated by it [11]. This effect is observed throughout the plasma and exists on all scales larger than a characteristic shielding length, called the Debye length. This length becomes important when determining how probes inserted into the plasma to determine its properties may actually perturb the plasma and yield misleading results.

Plasmas generated in electrostatic thrusters are often not in thermal equilibrium. In fact, the electron temperature is often a full order of magnitude higher than the ion temperature. This occurs because the same mechanisms that heat the electrons to high energies often do not act as effectively on the ions. Unlike the electrons, the ions are also not confined to the region of the thruster known as the plasma generator, which consists of the discharge cathode and anode. Instead, the ions are extracted into a beam in order to generate thrust [1].

Maxwell's four governing equations apply to the electric and magnetic fields in a plasma. These fundamental equations are

$$\nabla \cdot \vec{E} = \frac{\rho}{\varepsilon_0} \tag{6}$$

$$\nabla \times \vec{E} = -\frac{\partial \vec{B}}{\partial t} \tag{7}$$

$$\nabla \cdot \vec{B} = 0 \tag{8}$$

$$\nabla \times \vec{B} = \mu_0 \left(\vec{J} + \varepsilon_0 \frac{\partial \vec{E}}{\partial t} \right) \tag{9}$$

where $\vec{E}$ is the electric field, $\vec{B}$ is the magnetic field, ρ is the charge density, $\vec{J}$ is the current density, ε_0 is the permittivity of free space, and μ_0 is the permeability of free space.

Charged particles moving in the presence of a magnetic field travel in a characteristic helical path, which is produced by the Lorentz force. For a particle of charge q and velocity $\vec{v}$ interacting with a magnetic field that is directed along the z-axis, the force is given by the following.

$$\vec{F} = q\vec{v} \times \vec{B} \tag{10}$$

This equation may be solved for each of the three spatial components of the motion. The result is a harmonic oscillator characterized by a cyclotron frequency ω_c [1].

$$\omega_c = \frac{|q|B}{m} \tag{11}$$

The size of the orbit in which the particles move is given by the Larmor radius. This length may be derived by considering the forces acting on a charged particle in a magnetic field. Figure 8 shows the free body diagram of such a particle.

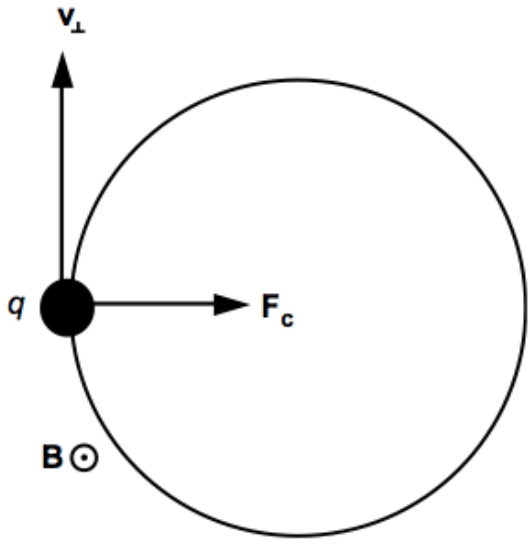

Figure 8: Forces Acting on a Charged Particle in a Magnetic Field [1]

Applying Newton's Second Law to the particle in the centripetal direction, the following equation is obtained.

$$qv_{\perp}B = \frac{mv_{\perp}^2}{r_L} \qquad (12)$$

where r_L is the Larmor radius and $v_{\perp}$ is the velocity component perpendicular to the magnetic field. This equation can then be solved for r_L.

$$r_L = \frac{mv_{\perp}}{qB} \qquad (13)$$

If an electric field is present in addition to the magnetic field, the motion of the particle will be perpendicular to the directions of both $\vec{E}$ and $\vec{B}$ and will have a velocity given by the following equation [1].

$$\vec{v} = \frac{\vec{E} \times \vec{B}}{B^2} \qquad (14)$$

While plasmas are generally electrically neutral, the presence of probes or walls perturbs the plasma and requires that it adjust its properties to match the imposed boundary conditions.

Because the electrons have a much higher mobility and kinetic energy than the ions, the flux of negative charge to the boundary would tend to be higher than for the positive charge. This creates a region of positive charge in the plasma, which serves to slow further loss of electrons. This adjustment, with the associated potential and density gradients, occurs through the presence of sheaths [1].

There are three cases to consider in the discussion of plasma sheaths. The first is when the potential change through the sheath is small compared to $k_B T_e$. In this situation, Debye shielding is the dominant phenomenon. Ordinarily, a single test charge will generate an electric field that decreases radially as $1/r$. However, if this test charge is placed in a plasma, the shielding ability of the plasma will result in a faster than $1/r$ fall-off of the electric field. Poisson's equation can be solved to determine the variation of the plasma potential with radial distance.

$$\nabla^2 \phi = -\frac{\rho}{\varepsilon_0} = -\frac{e}{\varepsilon_0}\left(Z n_i - n_e\right) \qquad (15)$$

where Z is the charge state of the ions.

This equation can be solved for the potential if it is assumed that $e\phi << k_B T_e$, the ion density is fixed, and the electron density follows Boltzmann's relationship. The following approximation is obtained.

$$\phi = \frac{e}{4\pi\varepsilon_0 r}\exp\left(-r \Big/ \sqrt{\frac{\varepsilon_0 k_B T_e}{n_0 e^2}}\right) \qquad (16)$$

This shows the effect of the plasma shielding as an exponential decrease in the potential in the radial direction. The denominator of the exponential is defined as a characteristic length over which these shielding effects are significant and is called the Debye length λ_D [1].

$$\lambda_D = \sqrt{\frac{\varepsilon_0 k_B T_e}{n_0 e^2}} \qquad (17)$$

In the case of the potential difference being of the same order as the electron temperature ($e\phi \approx k_B T_e$), the concept of a presheath is introduced. Ultimately, it is necessary to solve Poisson's equation, which requires expressions for the ion and electron densities. Assuming that the ions fall through a potential of ϕ_0 (representing the difference between the plasma potential and the potential at the sheath edge), conservation of energy at the sheath can be represented by the following [1].

$$\frac{1}{2} M v_0^2 = e\phi_0 \qquad (18)$$

Once in the sheath, the ions will gain additional energy as they continue to fall toward the boundary formed by the electrode surface. From conservation of energy, their velocity at any point x, measured from the sheath edge, can be calculated from

$$v = \sqrt{\frac{2e}{M}} \left[\phi_0 - \phi(x)\right]^{1/2} \qquad (19)$$

Since $v_0 = \sqrt{2e\phi_0 / M}$, Equation (19) can be rewritten as

$$\frac{v_0}{v} = \sqrt{\frac{\phi_0}{\phi_0 - \phi}} \qquad (20)$$

As the ion flux through the sheath must be conserved ($n_i v = n_0 v_0$), the ion density at any point may be represented by

$$n_i = n_0 \sqrt{\frac{\phi_0}{\phi_0 - \phi}} \qquad (21)$$

For the electron density in the sheath, the Boltzmann relationship is used.

$$n_e = n_0 \exp\left(\frac{e\phi}{k_B T_e}\right) \tag{22}$$

Using equations (20) and (21) in Poisson's equation, it is found that the following inequality must be true.

$$\frac{1}{2\phi_0} > \frac{e}{k_B T_e} \tag{23}$$

This is necessary to avoid reflection of ions away from the boundary and to insure that the sheath potential decreases monotonically from its value in the plasma to the value at the boundary. Equation (23) can be rewritten in terms of the required velocity instead of the required potential drop.

$$v_0 \geq \sqrt{\frac{k_B T_e}{M}} \tag{24}$$

This velocity is called the Bohm velocity and is the minimum value for ions entering the sheath. To produce this velocity, the potential drop in the presheath must be at least $T_e / 2$ [1].

Using this result, it is possible to determine the current flowing to the boundary. The so-called Bohm current is given by Equation (25).

$$I_i = \frac{1}{2} ne \sqrt{\frac{k_B T_e}{M}} A \tag{25}$$

where A is the current collection area at the boundary [1].

Finally, for the case of a potential difference much larger than the electron temperature $(e\phi >> k_B T_e)$, the theory developed by Child and Langmuir applies. Here, the potential difference is large enough to repel almost all electrons attempting to reach the boundary. Consequently, the electron density reaches zero at the sheath edge, and only the ion density must

be considered inside the sheath. Using Equation (19) for the ion velocity, the ion density is found to be

$$n_i = \frac{J_i}{e}\left[\frac{M}{2e(\phi_0 - \phi)}\right]^{1/2} \tag{26}$$

Solving Poisson's equation using only the ion contribution yields the following equation, which is known as the Child-Langmuir law.

$$J_i = \frac{4\varepsilon_0}{9}\left(\frac{2e}{M}\right)^{1/2}\frac{V^{3/2}}{d^2} \tag{27}$$

where d represents the sheath thickness and V is the potential across the sheath.

Plasmas, like other fluids, can be also be placed into several broad categories relating to the significance of collisions experienced by the particles. The Knudsen number is a non-dimensional number that is used to make this determination. Defined as the ratio of the mean free path to a characteristic length, Knudsen numbers greater than 10 indicate a free molecular flow, while those less than 0.01 indicate a continuum flow [12]. Ratios between these extremes describe transitional flow regimes. For plasma diagnostics with Langmuir probes, the characteristic length can be taken to be the probe diameter.

Calculation of the mean free path relies on knowledge of the density of the species under consideration and on the collision cross section for the particle. If the particles are neutral, then this cross section is simply the cross-sectional area of the particle. For collisions involving Coulomb forces, such as those encountered in plasma physics, the collision cross-section must account for this complexity. Bittencourt provides a relationship for the collision cross section for electron-ion collisions. (Because of the attractive force, these collisions will have the shortest mean free path and will therefore be the determining parameter for the flow regime.) [13]

$$\sigma_m = 2\pi b_0^2 \ln\left[1 + \left(\frac{\lambda_D}{b_0}\right)^2\right] \tag{28}$$

where λ_D is the Debye length and b_0 is given by Equation (29) for electron-ion collisions.

$$b_0 = \frac{e^2}{12\pi\varepsilon_0 k_B T} \tag{29}$$

Then the mean free path is calculated by Equation (30).

$$\lambda = \frac{1}{n\sigma_m} \tag{30}$$

For collisions involving neutral particles, such as electron-neutral collisions, the mean free path is given by Equation (31).

$$\lambda_{en} = \frac{\sqrt{2}}{n\sigma_{en}} \tag{31}$$

where σ_{en} is typically on the order of $5\times10^{-19} m^2$ [14].

1.4 Energy Distribution Functions

1.4.1 Maxwellian

It is impractical to track individual gas molecules as they travel in the electric and magnetic fields and experience collisions in a thruster. Fortunately, distribution functions have been developed that describe, probabilistically, the range of velocities and energies that a particle may have. For gases in equilibrium, a distribution called the Maxwellian applies. Developed by James Clerk Maxwell and Ludwig Boltzmann, this distribution takes the form of a probability function. In terms of velocity, the Maxwellian distribution is expressed as follows.

$$f(v) = \left(\frac{m}{2\pi k_B T}\right)^{1/2} \exp\left(-\frac{m}{2k_B T}\left(u^2 + v^2 + w^2\right)\right) \quad (32)$$

where m is the particle mass, k_B is Boltzmann's constant, T is the temperature, and u, v, and w are the three velocity components [1].

It is also possible to write the Maxwellian distribution in terms of the particle's speed, C, instead of its individual velocity components.

$$\chi(C) = 4\pi\left(\frac{m}{2\pi k_B T}\right)^{3/2} C^2 \exp\left(-\frac{mC^2}{2k_B T}\right) \quad (33)$$

The width of the distribution is determined by the temperature, with higher temperatures reflecting a wider range of probable velocities. This distribution can also be rewritten in terms of the energy ε by making the substitution $\varepsilon = \frac{1}{2}mv^2$ and noting that $f(\varepsilon) = \chi(C)\frac{dC}{d\varepsilon}$, where $\frac{dC}{d\varepsilon} = \left(\frac{1}{2m\varepsilon}\right)^{1/2}$ [12]. The resulting energy distribution is given in Equation (34).

$$f(\varepsilon) = \frac{2}{(k_B T)^{3/2}}\sqrt{\frac{\varepsilon}{\pi}} \exp\left(-\frac{\varepsilon}{k_B T}\right) \quad (34)$$

From the Maxwellian distribution, several important speeds and energies can be calculated.

The average speed $\overline{C}$, the root-mean-square speed $\left(\overline{C^2}\right)^{1/2}$, and the most probable speed C_{mp} can be derived by integrating or differentiating the distribution function.

$$\overline{C} = \frac{2\sqrt{2}}{\pi^{1/2}}\left(\frac{k_B T}{m}\right)^{1/2} \quad (35)$$

$$\left(\overline{C^2}\right)^{1/2} = \left(\frac{3k_B T}{m}\right)^{1/2} \quad (36)$$

$$C_{mp} = \left(\frac{2k_B T}{m} \right)^{1/2}$$

Similarly, the most probable energy can also be derived.

$$\varepsilon_{mp} = \frac{1}{2} k_B T \qquad (37)$$

In plasmas, it is possible for each species of particle to be characterized by its own temperature. Despite this, the Maxwellian distribution may still apply to each species individually.

1.4.2 Non-Maxwellian

While the Maxwellian has wide applicability, there are many other distributions that may better describe the energies or velocities of a particular collection of molecules. In particular for low-pressure plasmas, the deviation from the Maxwellian may be significant [15]. One such alternate distribution is called the Druyvesteyn distribution. This distribution has its peak shifted toward slightly higher energies than the Maxwellian distribution. In contrast, however, the Maxwellian distribution has a much greater number of fast electrons, as the Druyvesteyn distribution falls off to zero more quickly. Furthermore, this distribution assumes that the free path length of the electrons is independent of energy [16]. The Druyvesteyn distribution is given by

$$f_D(\varepsilon) = A_D \varepsilon^{1/2} \exp\left[- B_D \left(\frac{\varepsilon}{eT} \right)^2 \right] \qquad (38)$$

where A_D and B_D are functions of the average energy lost in each collision, the electric field strength, and the mean free path. Ming Li et al. have developed a version of the Druyvesteyn

distribution, with the constants selected to match the mean kinetic energy to that of the Maxwellian distribution. In that case, the following equation applies [15].

$$f_D(\varepsilon) = \frac{0.5648 n_e}{(k_B T)^{3/2}} \varepsilon^{1/2} \exp\left[-0.243\left(\frac{\varepsilon}{k_B T}\right)^2\right] \qquad (39)$$

The Druyvesteyn distribution differs from the Maxwellian distribution primarily in its use of a higher exponent for ε within the exponential. A comparison of the Maxwellian and Druyvesteyn distributions, plotted for the same temperature, appears in Figure 9.

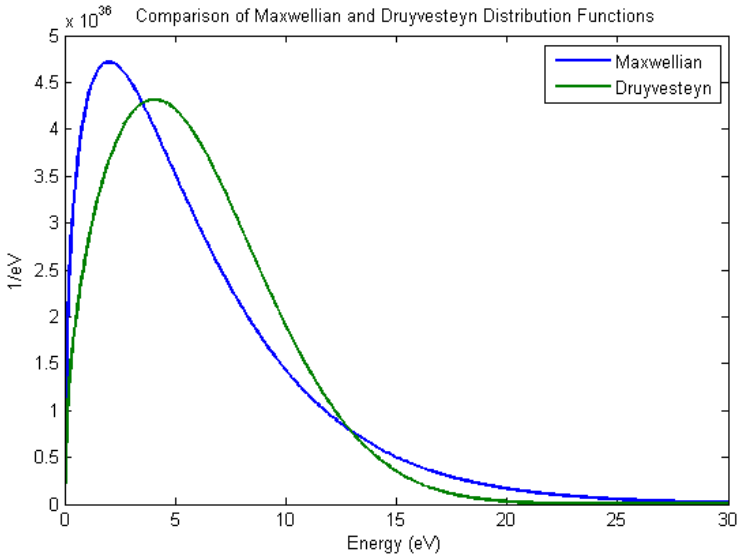

Figure 9: Comparison of Maxwellian and Druyvesteyn Distributions

The Druyvesteyn distribution is often applicable in low-pressure plasmas, in which the electric field strength is sufficiently low such that any inelastic collisions may be ignored [15]. However, the electric field must be high enough such that the electron temperature remains significantly higher than the ion temperature. This is a condition that exists in electrostatic thrusters, where the ratio of electron temperature to ion temperature is typically 10 or more [1].

2 Plasma Diagnostics

2.1 Single Langmuir Probes

2.1.1 Principle of Operation

Electric probes represent a broad category of plasma diagnostics. Irving Langmuir, the eponymous developer of the Langmuir probe, was one of the first to study their properties. The Langmuir probe consists of a single electrode that is inserted into the plasma to be investigated; the current collected by the probe is measured over a range of applied bias potentials. The resulting current-voltage characteristic can then be analyzed and several important plasma properties extracted. Ideally, this I-V characteristic assumes the shape shown in Figure 10 below [17].

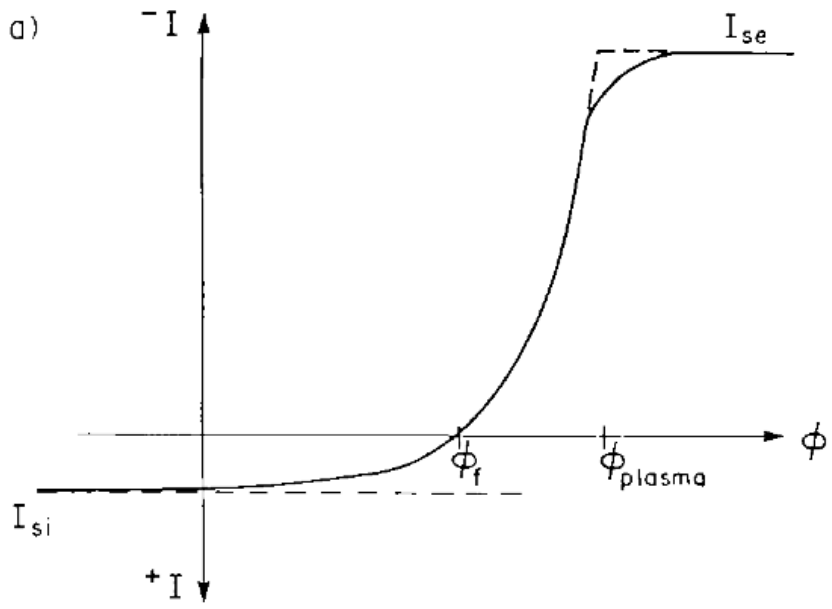

Figure 10: Ideal Langmuir Probe I-V Characteristic [17]

Several regions are immediately apparent in this ideal trace. By convention, electron currents are plotted as positive. For very negative bias voltages, the probe collects only ions and repels all electrons. This is called the ion saturation region, and is characterized by a saturation

ion current, I_{si}. As the probe bias voltage is made more positive, fewer ions are collected and fewer electrons are repelled. When both the ion and electron currents are equal, so that the net current to the probe is zero, the probe is at the floating potential, ϕ_f. As the bias voltage continues to increase, the collected ion current becomes negligible relative to the electron current as fewer electrons are repelled. This is called the transition or exponential region of the trace. Electron saturation is reached for probe bias potentials at or above the plasma potential, ϕ_s [18]. Once the plasma potential has been reached, the probe theoretically collects all of the incident thermal electrons. A gradual increase in the electron current is usually observed beyond this point because the plasma sheath surrounding the probe continues to expand.

Langmuir probes may be used to obtain the electron temperature, the plasma density, and the plasma potential. Of these, the simplest quantity to extract from the I-V characteristic is the electron temperature [18]. In the transition region, the electron current is given by the following:

$$I_e = I_{se} \exp\left[e\left(\phi_p - \phi_s\right)/\left(k_B T_e\right)\right] \qquad (40)$$

where

$$I_{se} = e n_e A \left(\frac{k_B T_e}{2\pi m}\right)^{1/2} \qquad (41)$$

Here, I_e is the electron current, I_{se} is the electron saturation current, e is the elementary charge, ϕ_p is the probe bias voltage (referenced to facility ground), ϕ_s is the plasma potential (also referenced to facility ground), k_B is Boltzmann's constant, T_e is the electron temperature (in kelvin), n_e is the electron density, A is the probe area, and m is the electron mass. It is customary to work with the quantity $k_B T_e / e$, which is the electron temperature in units of electron volts.

This shows that the electron current collected by the probe, when plotted on a semilog plot versus the probe bias potential ϕ_p, should be a straight line whose slope is given by $1/T_{eV}$, where T_{eV} is the electron temperature measured in electron volts.

Before the method outlined above can be used, the ion current must be subtracted from the total current to obtain the electron current. In many cases, this can be done by extrapolating the ion saturation current to the electron region with a straight line. In other cases, more complex ion collection theories may be applied to give better results [18].

In addition to the electron temperature, it is also possible to calculate the plasma potential from the "knee" in the I-V characteristic. This marks the transition from the exponential region of the curve to the electron saturation region. The very pronounced knee shown in the ideal probe trace in Figure 10 is not often obtainable in practical experiments. As shown in Figure 11, the shape of the probe used also has a marked influence on the behavior of the I-V characteristic [19].

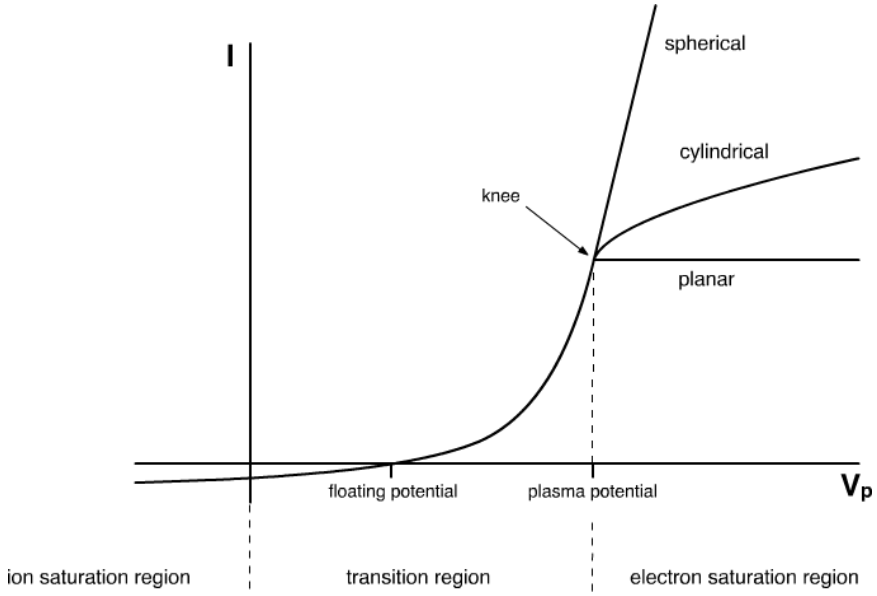

Figure 11: Comparison of I-V Characteristics for Various Probe Shapes [19]

The most pronounced knee occurs for the case of a planar probe. For cylindrical or spherical probes, the knee is much less distinct and may be more difficult to locate precisely. A similar rounding of the knee can be produced by the presence of strong magnetic fields or collisional effects in the plasma.

In such situations, numerical differentiation of the probe trace may be employed to determine the plasma potential. The transition from the exponential region to the electron saturation region is marked by an inflection point, which may be located by finding the maximum of $\frac{dI}{dV}$ or where $\frac{d^2I}{dV^2} = 0$ [18].

2.1.2 Ion Collection Models

Thin-Sheath Theory

More sophisticated methods for characterizing the collected ion current have been developed. Among the earliest and simplest to use is known as thin-sheath theory and was developed by Irving Langmuir [17]. When any probe is inserted into a plasma, the plasma

properties may be perturbed in the vicinity of the instrument, usually over a distance of several Debye lengths. In thin-sheath theory, it is assumed that the Debye length is much less than the size of the probe. Chen suggests that the ratio of probe diameter to Debye length (r_p / λ_D) should be greater than ten for this theory to be applicable [20]. The probe itself is also assumed to be much smaller than the mean free paths for electrons and ions in the plasma. Furthermore, it is assumed that the electron and ion densities are equal (the quasineutrality assumption), that Maxwellian velocity distributions are present far from the probe, that there is no drift velocity associated with the plasma, and that the probe itself is not emitting electrons [17].

To calculate the electron density, the local velocity distribution function is used. Integrating this function over the relevant electron velocities yields

$$n_e(x) = \int_{-\infty}^{v_c} n_0 \left(\frac{m}{2\pi k_B T_e} \right)^{1/2} \exp\left[\frac{-1/2\, mv^2 + e\phi(x)}{k_B T_e} \right] dv \quad (42)$$

where v_c is the critical velocity, below which incoming electrons will not reach the probe, given by

$$v_c = \sqrt{\frac{2e\left[\phi(x) - \phi(x_p)\right]}{m_e}} \quad (43)$$

Here, $\phi(x)$ is the potential at an arbitrary point in the plasma, $\phi(x_p)$ is the potential at the probe surface, and m_e is the electron mass. In Equation (42), x is taken to be zero at the probe surface, and n_0 is the plasma density measured at an infinite distance from the probe. Note that this integration considers planar geometry only; consequently, v refers to the x-component of the particle's velocity.

Completing the integration and simplifying produces the familiar Boltzmann relation

$$n_e(x) = n_0 \exp\left[\frac{e\phi(x)}{k_B T_e}\right] \qquad (44)$$

To determine the current collected by the probe, calculation of the ion and electron fluxes is required [17]. Because of quasineutrality, Equation (44) above also applies to ions. Consequently, using it and conservation of energy to determine the ion velocity (with the assumption that the ion temperature is low enough such that the kinetic energy of the ions far from the probe is zero), the following expression for the ion flux is obtained.

$$\Gamma_i(x) = n_i(x)v_i(x) = n_0 \exp\left[\frac{e\phi(x_s)}{k_B T_e}\right]\left(\frac{-2e\phi(x_s)}{M_i}\right)^{1/2} \qquad (45)$$

For the electrons, the flux is given by the random flux

$$\Gamma_e = \frac{1}{4} n_e v_e \qquad (46)$$

Using the Maxwellian relationship for the electron thermal speed $\left(v_e = \left[\frac{8k_B T_e}{\pi m}\right]^{1/2}\right)$, the electron flux is

$$\Gamma_e = \frac{1}{4} n_0 \exp\left[\frac{e\phi(x_p)}{k_B T_e}\right]\left(\frac{8k_B T_e}{\pi m}\right)^{1/2} \qquad (47)$$

Combining these results yields an expression for the total current, in which A_p and A_s are the areas of the probe and sheath.

$$I = e\left[-\frac{1}{4} A_p n_0 \exp\left[\frac{e\phi(x_p)}{k_B T_e}\right]\left(\frac{8k_B T_e}{\pi m}\right)^{1/2} + A_s n_0 \exp\left[\frac{e\phi(x_s)}{k_B T_e}\right]\left(\frac{-2e\phi(x_s)}{M_i}\right)^{1/2}\right] \qquad (48)$$

Note that this equation contains $\phi(x_s)$, the potential at the edge of the sheath, in addition to $\phi(x_p)$, the potential at the probe itself. The former must be obtained by solving Poisson's

equation inside the sheath. The result, assuming that the plasma potential is much greater than the probe potential is

$$\phi_s = -\frac{k_B T_e}{2e} \tag{49}$$

Making this final substitution into Equation (48) and assuming that $A_p \approx A_s$, we obtain an expression for the total current to the probe.

$$I = -eA_p \left\{ \frac{1}{4} n_0 \left(\frac{8k_B T_e}{\pi m} \right)^{1/2} \exp\left[\frac{e\phi(x_p)}{k_B T_e} \right] - n_0 \left(\frac{k_B T_e}{M_i} \right)^{1/2} \exp(-1/2) \right\} \tag{50}$$

Within this equation, expressions for the saturation currents can be identified.

$$I_{se} = -\frac{1}{4} eA_p n_0 v_e \tag{51}$$

$$I_{si} = eA_p \exp(-1/2) n_0 v_i = 0.61 eA_p n_0 v_i \tag{52}$$

Then,

$$I = I_{se} \exp\left[\frac{e\phi(x_p)}{k_B T_e} \right] + I_{si} \tag{53}$$

Several useful quantities can be extracted from these equations. Firstly, the electron temperature T_e can be obtained by solving for the slope of Equation (50) in the exponential region after the ion current has been subtracted. With this known, Equation (52) allows the plasma density to be calculated. Finally, Equation (50) can be set equal to zero to determine the floating potential. Note that thin-sheath theory makes the implicit assumption that the ion temperature T_i is much less than the electron temperature. If a finite ion temperature is present, the orbital motions of the ions must be accounted for in the model [17].

The calculation of the electron temperature by finding the slope of Equation (50) is not restricted to cases in which thin-sheath theory is applicable. This relationship is in fact very

robust. Consequently, the electron temperature is one of the easiest measurements to obtain from a Langmuir probe trace [18].

Orbital Motion Limited Theory

A model that attempts to account for a finite ion temperature is that of Mott-Smith and Langmuir. Known as the Orbital Motion Limited (OML) theory, the model accounts for particle orbits within the sheath surrounding a probe. An important assumption inherent to OML theory is that particles with any energy can potentially reach the probe surface [21].

For the case of an attracting cylindrical probe, it is possible to define an impact parameter h_p such that electrons approaching at this radial distance will graze the surface of the probe. This geometry is presented in Figure 12 below [21].

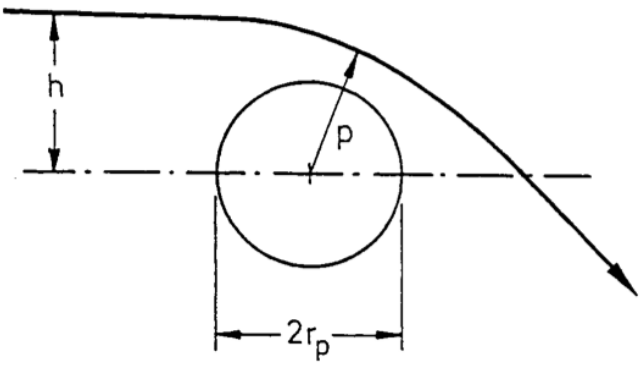

Figure 12: Geometry Associated with Electron Attraction in OML Theory [21]

Conservation of energy and angular momentum for the electrons gives

$$\frac{1}{2}mv^2 = \frac{1}{2}mv_p^2 - e\phi_p \qquad (54)$$

$$mvh_p = mr_p v_p \qquad (55)$$

The impact parameter is given by the following for electrons having initial energy $e\phi_0$.

$$h_p = r_p(1+\phi_p/\phi_0)^{1/2} \qquad (56)$$

The current supplied to the probe by electrons in a differential velocity range dv is given by

$$dI = 2\pi r_p le(1+\phi_p/\phi_0)^{1/2}\frac{v}{\pi}dn \qquad (57)$$

where $\frac{v}{\pi}dn$ represents the flux of electrons moving perpendicular to the probe. (Those moving parallel to the probe are not collected.)

An expression for the differential number density dn can be developed by assuming a Maxwellian distribution of velocities.

$$dn = n_0\left(\frac{m}{2\pi k_B T_e}\right)\exp\left(\frac{-mv^2}{2k_B T_e}\right)2\pi v dv \qquad (58)$$

Integrating Equation (57) yields an expression for the electron current collected by the probe.

$$I_e = 2\pi n_0 r_p le\left(\frac{k_B T_e}{2\pi m}\right)^{1/2}\left[\frac{2\sqrt{\eta}}{\sqrt{\pi}} + \exp(\eta)erfc\left(\sqrt{\eta}\right)\right] \qquad (59)$$

where the non-dimensional probe bias is defined as

$$\eta = \frac{e\phi_p}{k_B T_e} \qquad (60)$$

For values of η greater than 2, the following approximation may be used.

$$I_e = 2\pi n_0 r_p le\left(\frac{k_B T_e}{2\pi m}\right)^{1/2}\frac{2}{\sqrt{\pi}}\left(1+\frac{e\phi_p}{k_B T_e}\right)^{1/2} \qquad (61)$$

This shows that a plot of I^2 versus ϕ_p in the electron saturation region should be a straight line. From this plot, it is possible to determine n_0 from the slope and T_e from the intercept with the current axis [21].

An equation for ion collection can be derived similarly.

$$I_i = 2\pi n_0 r_p l e \left(\frac{k_B T_i}{2\pi M_i} \right)^{1/2} \frac{2}{\sqrt{\pi}} \left(1 - \frac{e\phi_p}{k_B T_i} \right)^{1/2} \qquad (62)$$

Note that if the equation for ion collection is applied, the only quantity that can be obtained from OML theory is the plasma density. This value is again derived from the slope of square of the current versus the probe bias voltage, assuming that the plasma potential is known.

2.1.3 End Effects and Probe Alignment

In some cases, the orientation of the probe relative to the plasma can have a significant effect on the ion current collected by the probe. This effect is most pronounced for short probes operating in plasmas with a significant ion drift velocity in which the Debye length is comparable to or greater in size than the probe diameter.

When the probe is aligned parallel to the flow direction, a significant fraction of ions can reach the probe surface by entering the portion of the sheath surrounding the end of the probe. For an idealized, infinitely long probe, the only path to the probe is through the sheath that surrounds the sides of the probe. A plot of the ion current vs. the probe angle of attack is shown in Figure 14 below, where the angle of attack is defined as in Figure 13 [22].

Figure 13: Probe Angle of Attack in a Plasma with Drift Velocity U [22]

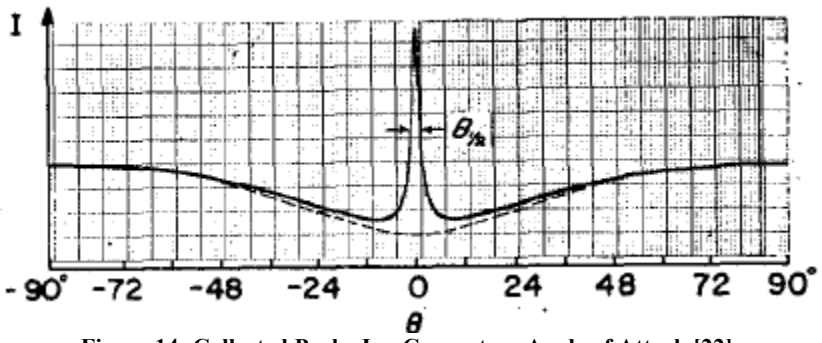

Figure 14: Collected Probe Ion Current vs. Angle of Attack [22]

It is clear that, given the right conditions, direct alignment of the probe with the flow direction of the plasma can cause a significant increase the collected ion current. This occurs because ions approaching the probe from the front and striking the tip are not limited by the orbital motions that would ordinarily repel some ions.

In order to determine whether end effects are significant when applying the various ion collection theories for Langmuir probe analysis, the following non-dimensional parameter is used.

$$\tau_l = \frac{l_p}{\lambda_D} \frac{\sqrt{k_B T_e / m_i}}{U} \qquad (63)$$

where l_p is the length of the probe, λ_D is the Debye length, k_B is Boltzmann's constant, T_e is the electron temperature, m_i is the ion mass, and U is the plasma drift velocity. The term under the radical is the thermal speed of the ions [22]. End effects may be ignored if $\tau_l >> 1$.

For this experiment, the plasma drift velocity is negligible compared to the thermal speed because no beam extraction is employed. Consequently, if the length of the probe is chosen such that it is several times larger than the Debye length, end effects on the collected ion current will be negligible.

Another issue that may affect ion collection is the presence of a perpendicular component of the ion velocity. This may occur when the probe is not aligned parallel to the flow direction, such as when it has been translated radially away from the cathode orifice. This misalignment may adversely affect the calculated values of the electron temperature and plasma density obtained from the probe trace [23]. In order to mitigate these effects, Langmuir probes are often rotated to maintain constant alignment parallel to the flow direction when used with electric thrusters. In the case of this experiment, however, there is no beam extraction. As noted in the discussion of end effects above, the bulk plasma drift velocity is assumed to be negligible compared to the ion thermal speed. Consequently, it is possible to make reliable measurements without maintaining the probe alignment parallel to the flow vector.

2.1.4 Druyvesteyn Method for Determining the EEDF

In many plasmas, the Maxwellian may not be a good description of the distribution of the energies of the constituent particles. Knowledge of the actual electron energy distribution function (EEDF) allows the computation of many other plasma properties, including the density and the electron temperature. Druyvesteyn, working in Holland in the early 20^{th} century, developed a method for determining the EEDF based solely on the collected Langmuir probe I-V characteristic [24].

The derivation of the Druyvesteyn formula is relatively straightforward. What follows is a summary of one presented by Lieberman and Lichtenberg [25]. In order for electrons to be

collected by the Langmuir probe, they must possess sufficient energy. This constraint is given by the following [25]

$$\frac{1}{2}mv^2 > eV \qquad (64)$$

where m is the electron mass, v is the electron velocity, e is the elementary charge, and V is the applied probe bias voltage, measured with respect to the plasma potential ϕ_s ($V = \phi_s - \phi_p$).

Considering electrons approaching from any general angle rather than just normal to the probe surface ($\theta = 0$), the above constraint can be expanded to the following [25]

$$\frac{1}{2}m(v\cos\theta)^2 > eV \qquad (65)$$

Assuming that there is some distribution of velocities $f(v)$, the total current to the probe can be expressed as a triple integral over all angles and velocities.

$$I_e = eA_p \int_0^{2\pi} d\phi \int_{v_{\min}}^{\infty} v^3 f(v) dv \int_0^{\theta_{\max}} \cos\theta \sin\theta \, d\theta \qquad (66)$$

where $v_{\min} = \left(\frac{2eV}{m}\right)^{1/2}$, $\theta_{\max} = \cos^{-1}\left(\frac{v_{\min}}{v}\right)$, ϕ is the azimuthal angle, and A_p is the exposed surface area of the probe. $v_{\min}$ represents the minimum velocity that electrons must have in order to overcome the potential barrier and reach the probe.

By performing the integration over all the angles, the following result is obtained.

$$I_e = \pi e A_p \int_{v_{\min}}^{\infty} \left(1 - \frac{v_{\min}^2}{v^2}\right) v^3 f(v) dv \qquad (67)$$

Because an expression for the energy distribution function is desired, a substitution for v may be obtained from the definition of the particle energy, expressed in electron volts,

$$\varepsilon = \frac{1/2 mv^2}{e} \tag{68}$$

so that

$$I_e = \frac{2\pi e^3}{m^2} A_p \int_V^\infty \varepsilon \left[\left(1 - \frac{V}{\varepsilon} \right) f(v(\varepsilon)) \right] d\varepsilon \tag{69}$$

This expression can then be twice differentiated with respect to V to obtain

$$\frac{d^2 I_e}{dV^2} = \frac{2\pi e^3}{m^2} A_p f(v(V)) \tag{70}$$

However, this expression is in terms of the velocity distribution function and not the energy distribution function. The two may be interchanged with the use of the following relationship [25].

$$F(\varepsilon) = 4\pi v^2 f(v) \frac{dv}{d\varepsilon} \tag{71}$$

Furthermore, from the definition of the kinetic energy, $\frac{dv}{d\varepsilon} = \left(\frac{1}{2m\varepsilon} \right)^{1/2}$. The complete relationship between the energy and velocity distribution functions is then defined.

$$F(\varepsilon) = 4\pi \frac{2\varepsilon}{m} \left(\frac{1}{2m\varepsilon} \right)^{1/2} f(v) \tag{72}$$

From Equation (70), it is possible to solve for the velocity distribution.

$$f(v) = \frac{m^2}{2\pi e^3 A_p} \frac{d^2 I}{dV^2} \tag{73}$$

Combining Equations (70) and (71), and substituting $\varepsilon = eV$,

$$F(\varepsilon) = \frac{4}{e^2 A_p} \left(\frac{mV}{2e} \right)^{1/2} \frac{d^2 I}{dV^2} \tag{74}$$

Equation (74) is the Druyvesteyn formula that relates the probe characteristic to the non-normalized electron energy distribution function. Note that it also requires knowledge of the plasma potential, so that the probe bias may be calculated with respect to it [25]. If the EEDF is known, then several other parameters may be calculated. This method avoids the uncertainties associated with applying the thin-sheath or OML ion collection models but retains the restriction that the plasma must be collisionless (having mean free paths much greater than the probe dimensions) and have negligible magnetic fields.

The number density is easily calculated by

$$n_e = \int_0^\infty F(\varepsilon) d\varepsilon \qquad (75)$$

The electron temperature may be obtained by averaging the energy over the distribution function [25].

$$T_e = \frac{2}{3}\frac{1}{n_e}\int_0^\infty \varepsilon F(\varepsilon) d\varepsilon \qquad (76)$$

2.2 Emissive Probes

The use of Langmuir probes is subject to several caveats. The results may be negatively affected by probe geometry, magnetic fields, and collisional effects in the plasma environment [26]. Plasmas which are flowing may also confuse the collected data by obscuring the true plasma potential or by introducing other knees which are not indicative of the actual value of ϕ_s.

In contrast to a Langmuir probe, an emissive probe uses a hairpin loop of wire heated to a sufficient temperature such that it begins to emit electrons itself [27]. This method avoids many of the problems that plague Langmuir probes when determining the plasma potential; they are relatively immune to geometrical effects and eliminate the need to interpret a possibly

ambiguous I-V characteristic from a Langmuir probe [18]. Instead, the plasma potential can directly be inferred from the floating potential of the emissive probe. This is the simplest method and requires no further data processing, though there are others that can improve accuracy. A cross-section of a typical probe is shown in Figure 15 below [27].

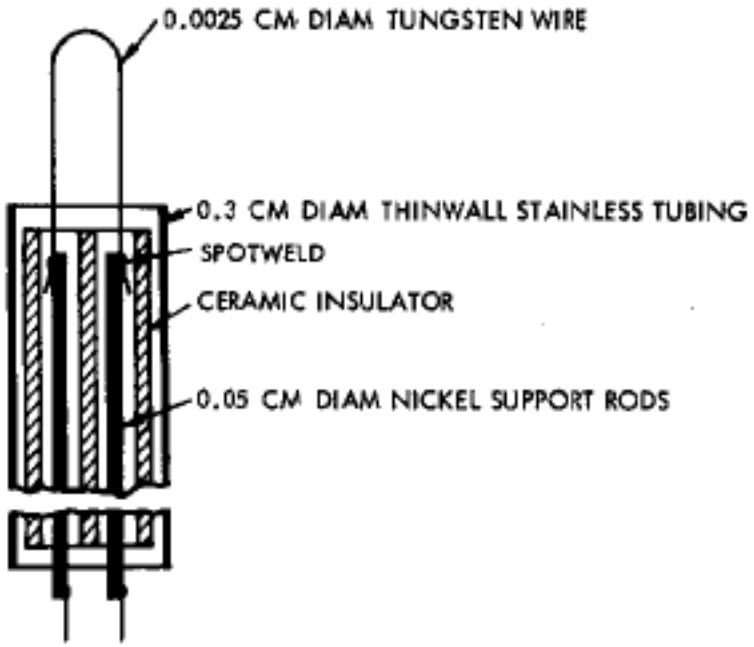

Figure 15: Construction of Typical Emissive Probe [27]

Emissive probes are constructed such that the only portion of the probe exposed to the plasma environment is the emitting part of the tungsten filament. Typical dimensions for the wire are $2-25\times10^{-3}$ cm with a length of approximately 0.5 cm. A DC power supply is used to induce thermionic emission in the tungsten wire, and the emissive probe potential can then be measured using a voltage divider. Alternatively, a half-wave rectified alternating current may be used as a heating current. In this case, data must be taken while the probe is not being heated to avoid nonuniform collection and emission over the exposed filament [28].

Floating Emissive Probes

In a configuration using a floating emissive probe, which was the method employed for this experiment, the probe and its heating circuit are permitted to achieve a floating potential within approximately 1 T_e of the plasma potential [29]. If properly connected through a circuit with high input impedance, the probe will provide a direct measurement of the plasma potential. The advantage of not requiring any post-processing of the collected data has made emissive probes a popular choice for plasma potential measurement. Ideally, the probe data collection circuit must also have a low capacitance to permit a wide frequency response. The characteristics of the probe's own "stray capacitance" mean that emissive probes have a wider frequency response in denser plasmas than in more dilute environments [27]. This is critical when the plasma environment is not quiescent and it is necessary to measure ϕ_s as a function of time, rather than as a steady-state value [26].

When biased to a potential higher than that of the surrounding plasma, emissive probes will not emit any electrons. Conversely, if the plasma potential is higher than the emissive probe bias, an electron current will flow from the probe to the plasma. This phenomenon is independent of many plasma characteristics, including whether the plasma is stationary [26]. An ideal emissive probe trace is shown in Figure 16 below, showing that the probe shifts from emitting electrons (shown as a negative electron current) to collecting electrons (a positive electron current) at the plasma potential [30]. Measurement of this I-V characteristic is used to determine the plasma potential.

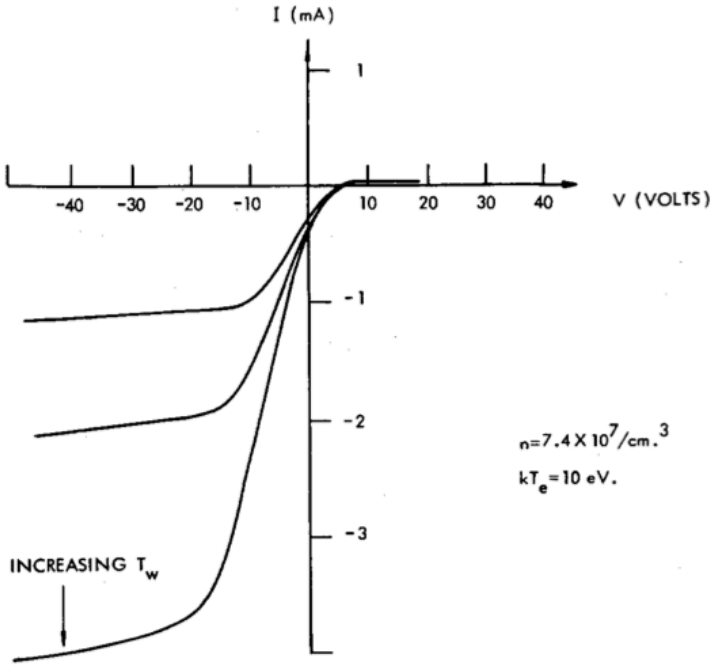

Figure 16: Ideal Emissive Probe Characteristic Curve [30]

Kemp and Sellen were the first to describe the characteristics of strongly emitting probes. They recognized that the plasma potential could be determined by locating the point at which electron emission begins to decay rapidly. According to a result derived by Langmuir, the emitted current decays according to the following [31].

$$\begin{aligned} I_e &= I_{e0}\exp[-e(\phi_w-\phi_s)/T_w]f(\phi_w-\phi_s) \quad && \phi_w \geq \phi_s \\ I_e &= I_{e0} && \phi_w < \phi_s \end{aligned} \tag{77}$$

where e is the fundamental charge, T_w is the emitted electron temperature at the probe surface, ϕ_s is the plasma potential, ϕ_w is the probe bias potential, and I_{e0} is the saturation electron current. Langmuir's results for the electron and ion currents collected by an emissive probe are presented below.

$$\begin{aligned} I_c &= I_{c0}\exp[e(\phi_w-\phi_s)/T_e] && \phi_w \leq \phi_s \\ I_c &= I_{c0}f'(\phi_w-\phi_s) && \phi_w > \phi_s \end{aligned} \tag{78}$$

$$I_i = I_{i0} g \qquad \phi_w < \phi_s$$
$$I_i = I_{io} \exp[-e(\phi_w - \phi_s)/T_i] \qquad \phi_w \geq \phi_s \qquad (79)$$

where I_{c0} and I_{i0} are the saturation currents and $g \approx 1$ [31].

The functions f and f', which account for orbital motion effects along with the value of g, are defined as follows.

$$f = [1 + e(\phi_w - \phi_s)/T_w]^{1/2}$$
$$f' = [1 + e(\phi_w - \phi_s)/T_e]^{1/2} \qquad (80)$$

Emissive probes also have a very wide range of possible applications. The University of Wisconsin-Madison has demonstrated the use of emissive probes in plasmas with pressures ranging from 10^{-6} to 1 torr and densities ranging from $<10^4$ cm^{-3} to 10^{13} cm^{-3} [26]. They have also been used in plasmas with ion and electron temperatures as high as 1 keV and 20 eV respectively [28].

Despite their advantages in measuring the plasma potential, emissive probes are unable to measure the electron temperature or plasma density, making their use often complementary with Langmuir probes. Emissive probes can also be used in this fashion to eliminate some of the ambiguities associated with nonideal Langmuir probe characteristics, providing an independent measurement of the plasma potential.

One application in which emissive probes are not insensitive to plasma properties is the case of an electron beam. The emitted current must be large enough to exceed the sum of the both the plasma current and the beam current [26]. It is also possible for charges to accumulate around the exposed portion of the probe and cause a rounding of the I-V characteristic. The probe is then said to be operating in the space-charge-limited regime. This problem is more pronounced when the emissive probe is being used in a very low density plasma or when the

surrounding electric fields are very weak [26]. This limits the ability to directly measure the plasma potential in many realistic plasma environments; the much lower energy electrons emitted by the probe form an additional sheath around the exposed portion of the probe [20]. It is only when the probe temperature is equal to the plasma electron temperature that the exact plasma potential will be indicated by the floating potential of the probe. Furthermore, contaminants on the probe surface may change the work function for tungsten, invalidating the results [28].

Double-Cross Method

Because the space-charge-limited regime's effects are most pronounced for the portion of the I-V characteristic near the plasma potential, methods have been developed to infer the plasma potential from measurements far from this region. One such method is the double-cross method [32]. The emitted current will be saturated for probe bias potentials less than the plasma potential. Above the plasma potential, the emitted current decays exponentially. When $\ln(I_e / I_{e0})$ is plotted versus the probe bias voltage, the result is shown in Figure 17 below.

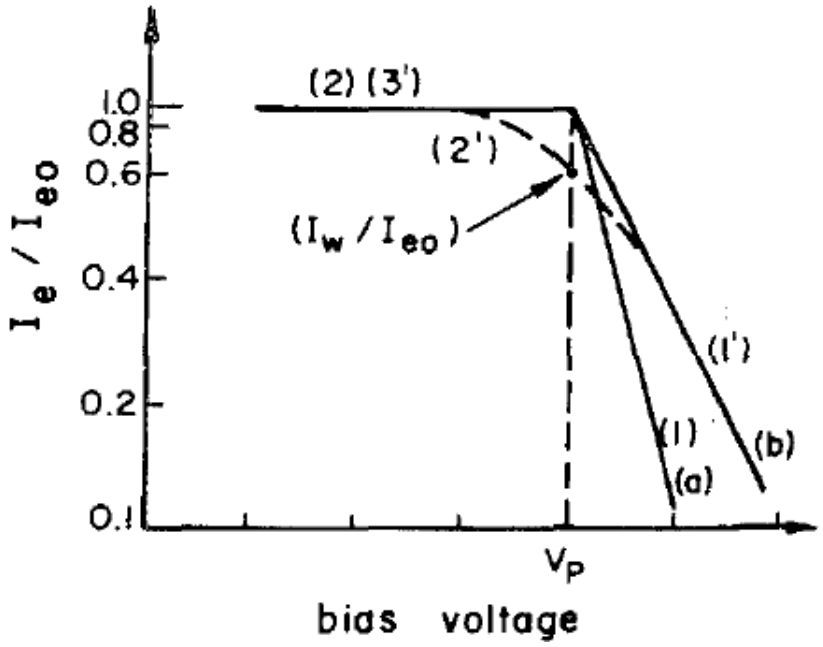

Figure 17: Double-Cross Method Plot [32]

Here, regions 1 and 2 correspond to the exponential and saturation portions of the I-V characteristic for an ideal probe operating outside the space-charge-limited regime. Within this regime, the curve takes on the form of the primed numbers: 1' is exponential decay, 2' is the space-charge effect region, in which the emitted current varies directly with $\left|\phi_s - \phi_w\right|^{3/2}$. The region labeled 3' is again the saturation portion of the curve [32]. Fortunately, however, the curve is asymptotic to two straight lines. The intersection of these lines indicates the plasma potential.

Self-Emitting Probes

Emissive probes also experience limitations when used in plasmas with very high electron current densities. As the probe must be heated sufficiently to achieve what is called "strong emission," melting of the tungsten filament may occur before this state is achieved.

Strong emission for emissive probes is defined as a condition in which the emitted current is much larger than the collected current.

$$\frac{I_e}{I_c} >> 1 \qquad (81)$$

where I_e is the emitted current and I_c is the collected plasma current [26]. For plasmas whose electron current density approaches the maximum achievable for thermionic emission, the conductors required to deliver the several amperes of heating current needed become large enough to perturb the plasma [26]. In these cases, a self-emitting probe may be substituted. In this case, the probes are heated to the point of thermionic emission by the plasma and may actually melt. The electrons emitted provide enough current to permit accurate measurements in plasmas with density up to 2×10^{12} cm^{-3} and electron temperature up to 50 eV. Unfortunately, self-emitting probes are only suited for use in pulsed discharge plasmas, as the melted probe must itself be replaced after each use [26].

Inflection Point Method

Some of the disadvantages inherent to emissive probes may be mitigated by improved data processing techniques. For example, plasmas with beam currents or space-charge rounding of the knee around the plasma potential may be successfully analyzed by the inflection point method. The I-V characteristic curve can be differentiated numerically and its inflection point found either by a routine that locates maximum values or by numerically solving for the zeros of the second derivative. This inflection corresponds to the plasma potential [26]. Using this processing technique eliminates the need for strong emission and opens a wider range of plasmas for study using emissive probes. The major disadvantage of this procedure is the time-consuming

nature of the data collection and processing steps. This data processing may be performed after collection using a differentiation code, or it may be done in real time with appropriate circuitry [32]. The inflection point method works best when operating outside of the space-charge-limited regime.

Differential Emissive Probes

Another way to avoid the need for a strongly emitting probe is to employ two probes in a differential configuration. Because hot and cold probe (i.e. a purely collecting probe) I-V curves tend to diverge when the bias voltage approaches that of the plasma potential, this method can be used to locate this point even if it is not clear from a single emissive probe trace [26]. This characteristic behavior is shown in Figure 18 [30].

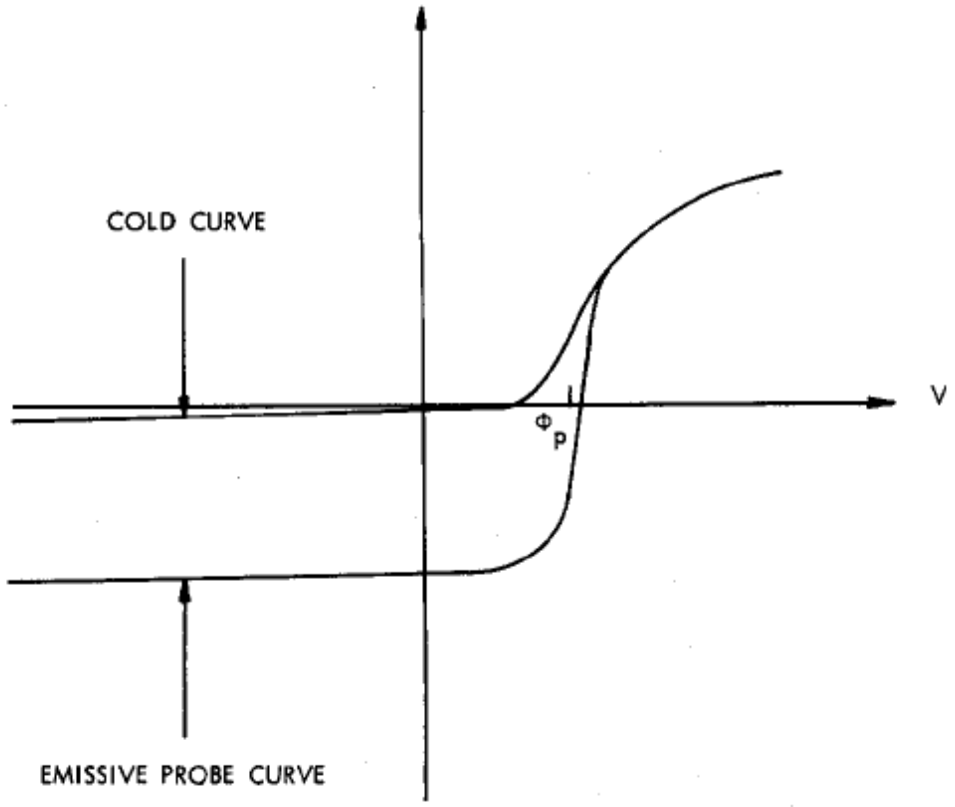

Figure 18: Divergence Between Emitting (Hot) and Collecting (Cold) Probes at Plasma Potential [30]

Droop Method

Finally, another method for determining the plasma potential has been proposed by Makowski and Emmert [33]. This method exploits the fact that the floating potential of the emissive probe varies with the probe temperature. When the probe is allowed to cool, such as when the filament current has been turned off, the floating potential of the probe decreases. Furthermore, the amount of "droop" in the probe floating potential is highly dependent on whether the probe is below or above the plasma potential; it is much more dramatic when above [33]. Consequently, by observing when the transition between these two behaviors occurs, it is possible to locate the plasma potential more accurately than direct indication by the floating

potential and the double-cross method [33]. Experimental results illustrating the application of this method are presented in below.

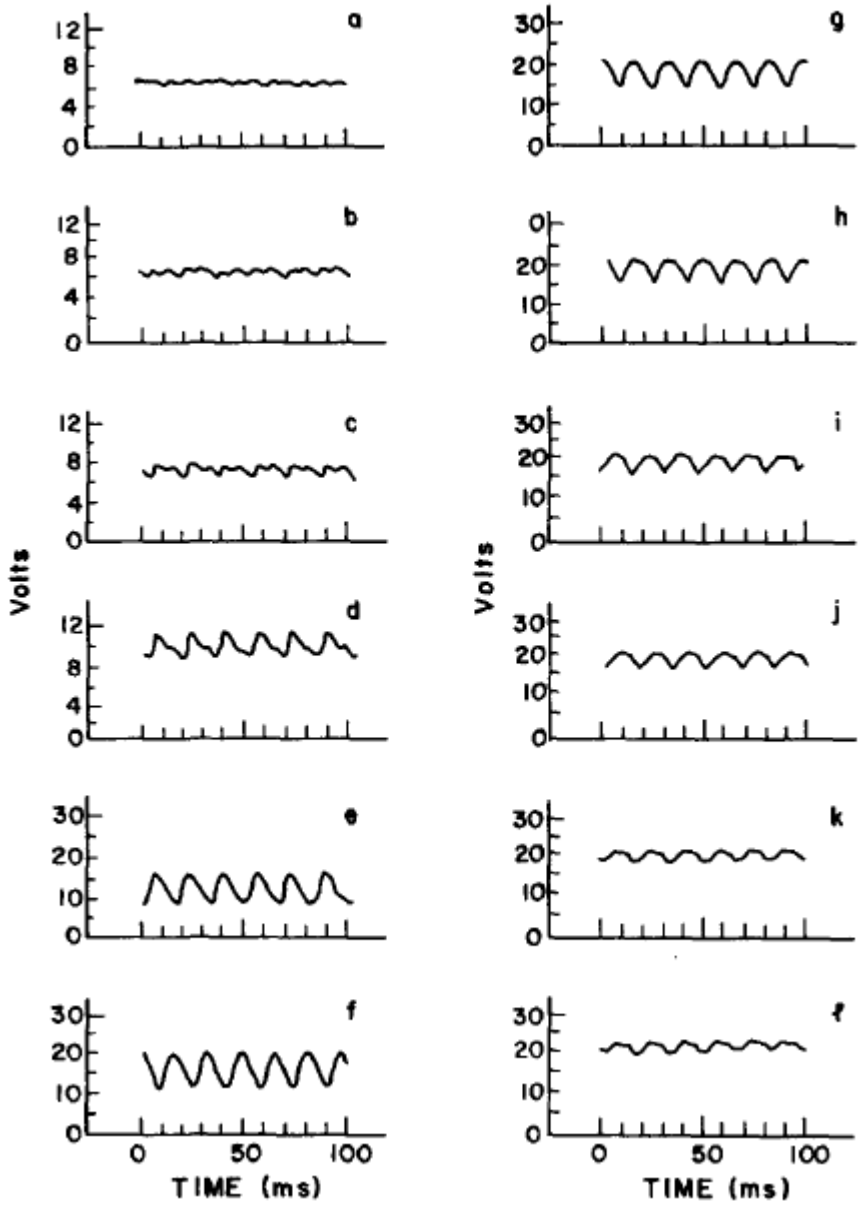

Figure 19: "Droop" Method for Determining Floating Potential [33]

These emissive probe traces show the probe floating potential as a function of time for increasing temperature values. Each oscillation represents one heating cycle of the probe. Graphs a-c show the small drops in floating potential as the probe is permitted to cool between cycles.

As the plasma potential is approached, the magnitude of the "droop" becomes progressively larger [33]. Graphs g and h show that the plasma potential has been reached, visible as a clipping of the signal. Once the plasma potential is reached, no further increase in the floating potential is observed [33].

3 Experimental Setup

3.1 Facility

This experiment was conducted in Worcester Polytechnic Institute's Vacuum Test Facility. This facility consists of a stainless steel vacuum chamber which measures 50 inches wide and 72 inches long. Rough pumping is achieved by a combination rotary mechanical pump and positive displacement Roots blower. The base pressure of the chamber is approximately 10^{-7} torr and is achieved using a CVI TM500 cryopump. This cryopump is capable of achieving a pumping speed of 10,000 liters per second on nitrogen, 8,500 liters per second on argon, and 4,600 liters per second on xenon. Pressure inside the chamber is measured using an MKS Instruments MKS 959 Hot Cathode Controller, which drives both Pirani and hot cathode vacuum gauges. Argon or xenon is supplied to the cathode through a gas supply manifold, and the flow rate is manually controlled using a Swagelok SS-SVCR4 needle valve. Swagelok SS-4-VCR4 diaphragm valves serve as shutoff valves for the gas cylinder and vacuum chamber supply lines. Measurement of the gas flow rate is provided by an MKS systems 179A mass flowmeter. The flowmeter is calibrated for argon using a bubble volumeter.

3.2 Cathode

The cathode used for this experiment is the Busek BHT-1500, which flew in space as part of the first successful Hall thruster demonstration on a U.S. spacecraft [34]. The Busek BHT-200 Hall thruster first flew on the U.S. Air Force's TacSat 2 technology demonstration satellite in 2006. A photograph of the complete Hall thruster, with the BHT-1500 hollow cathode appears below.

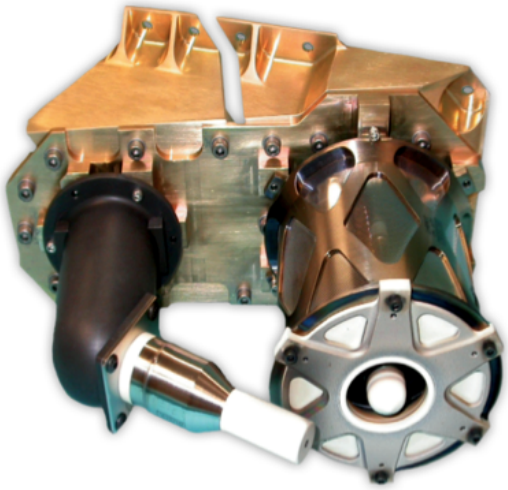

Figure 20: Busek Hall Thruster with BHT-1500 Hollow Cathode [34]

Because this experiment involves flight hardware, International Traffic in Arms Regulations (ITAR) prohibit the publication of exact discharge currents, propellant flow rates, and cathode dimensions. Consequently, all of the data presented in this thesis are normalized to a set of nominal operating conditions. Operation at other conditions is reported as a percent change from the nominal value of the parameter. The operating conditions considered in this experiment are presented in Table 1 below.

Table 1: Cathode Operating Conditions

Propellant	Operating Condition	Propellant Flow Rate (normalized to nominal conditions)	Discharge Current (normalized to nominal conditions)
Argon	Nominal	1	1
	Low-Flow	0.1-0.14	0.69
Xenon	Nominal	1	1
	Low-Flow	0.1	0.95

The cathode is composed of the electron-emitting insert, the cathode tube, the heater coil, and the keeper electrode. Three leads are used to power the cathode. The first supplies power to the cathode heater, the second serves as the primary current return path or cathode common, and

the third supplies power to the keeper. For these tests, the heater was powered by a TDK-Lambda 36V/25A power supply, and the keeper was powered by a Sorenson XFR 600-2 supply.

Startup of the cathode following exposure to atmosphere requires a lengthy conditioning process to remove any trace contaminants from the surface of the insert. Following the completion of this procedure, the cathode may be started and restarted as often as required, provided that a hard vacuum is maintained. To start the cathode, 6.5 A is applied to the heater for a minimum of three minutes. The keeper can then be biased to 600 V to start the discharge. Once the plasma discharge is initiated and current begins to flow between the cathode and the keeper, the keeper power supply transitions to the current-limited mode with an applied potential of approximately 20 V.

To produce an external plasma that can be studied, an anode is required. For this experiment, a cylindrical anode configuration was selected in order to permit easy access for the various diagnostic probes that were employed. The Langmuir probe is able to translate through slots milled in the sides of the anode. This configuration is shown in the figure below and is based on one used by Fossum et al. [35]. The anode is biased to approximately 100 V by a Sorenson DCR150 power supply.

Figure 21: Anode Configuration Allowing Langmuir Probe Traverses [10]

3.3 Instrumentation

3.3.1 Langmuir Probe

A Langmuir probe is mechanically very simple to construct. It consist of a short length of tungsten wire that is allowed to protrude into the plasma environment. For this experiment, a custom Langmuir probe was used. The main body of the probe is a length of 1/4-inch stainless steel tubing which is bent at a 90º angle to access the cathode. Tungsten wire of diameter 0.0035-inch is protected over most of its length by a 1/8-inch diameter alumina tube, which is supported by a 1/4-inch to 1/8-inch Swagelok reducing union. Because the probe wire cannot be allowed to short to the probe body, the tungsten wire is transitioned to 22-gauge magnet wire inside the stainless steel tubing. Magnet wire is sheathed in an enamel coating that is removed only where contact is desired with the tungsten filament. Connection to the data acquisition system is achieved by shielded coaxial cable and BNC connectors. During the experiment, the Langmuir probe is able to translate radially in front of the cathode at an axial distance of approximately 5 mm. This axial distance can be adjusted if necessary between experiments. The Langmuir probe is shown in Figure 22 below.

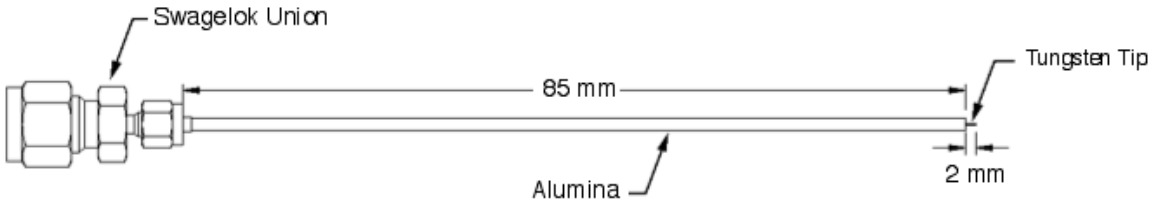

Figure 22: Schematic Showing Langmuir Probe Construction [10]

The bias potential for the Langmuir probe is applied by a Kepco BOP-1M bipolar power supply. This type of power supply can be controlled by an external programming source, allowing the operator to select a range of waveforms, frequencies, and sweep ranges. For this experiment, a Beckman FG2A function generator was used to output a ±4 V triangular waveform to serve as a programming signal. The Kepco power supply then amplifies this input and applies ±40 to the Langmuir probe. The frequency of the sweep is set to provide the required spatial resolution for the probe measurements. The probe positioning system moves at a measured speed of 1.27 mm/s. To provide 0.5-mm resolution, a sweep frequency of approximately 2.5 Hz was needed.

3.3.2 Emissive Probe

Emissive probes consist of a loop of tungsten wire that is exposed to the plasma environment. A current is passed through this loop to heat the wire to a temperature sufficient to begin thermionic emission of electrons.

The emissive probe shares similar construction with the Langmuir probe. The major difference is the use of double-bore alumina to support the loop of tungsten wire. The stainless steel tubing that forms the main body of the emissive probe was found to have a higher inner surface roughness than initially expected, causing the use of magnet wire to be problematic. The

enamel coating covering the magnet wire would abrade as the wire was pulled through the tubing, increasing the probability of a short between the wires or to ground through the probe body. This issue was resolved by switching to copper-constantan thermocouple wire, which is protected by a more robust fabric insulation.

In contrast to the Langmuir probe, the emissive probe for these tests is set to a fixed position, approximately 7 mm downstream of the cathode orifice. The emissive probe accesses the cathode from below via a hole cut into the lower surface of the anode. This is shown in Figure 23.

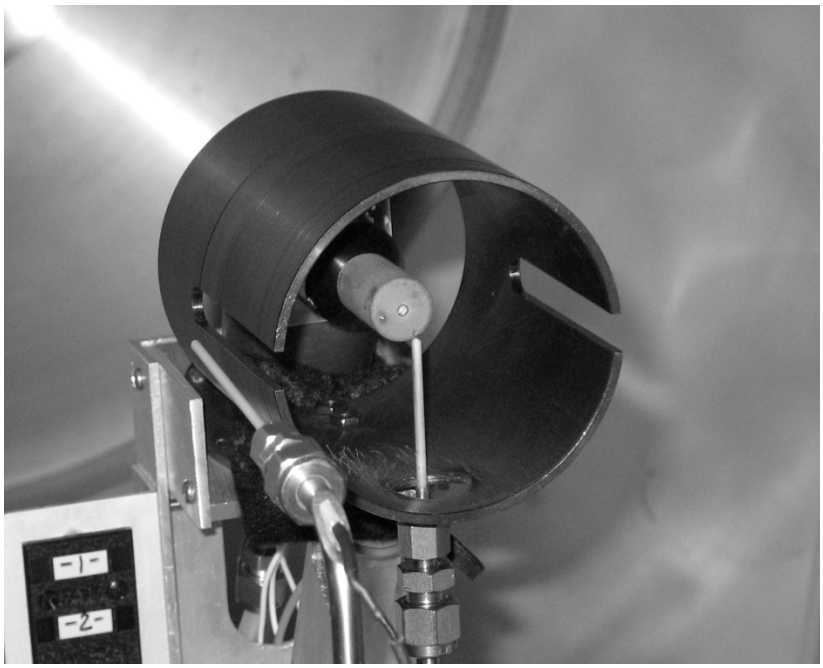

Figure 23: Emissive Probe Configuration

Power for the emissive probe is provided by an OTE HY3005-3 power supply. This power supply is isolated from facility ground by an isolation transformer and is kept behind a Plexiglas enclosure for operator safety. This permits the emissive probe to float to a voltage near the plasma potential.

During typical operation of the emissive probe, a heater current of approximately 2.3 A was used. This heater current was experimentally determined. By monitoring the floating voltage of the probe as the current is increased, strong emission is indicated when the floating voltage ceases to increase. This heater current was then used for all subsequent tests of the emissive probe.

3.3.3 Positioning System

The Langmuir probe is able to translate radially in front of the cathode in order to sample the plasma conditions at several different locations. Its axial position is fixed. Motion is controlled by a Slo-Syn stepper motor which drives a lead screw. The lead screw in turn moves the stage on which the Langmuir probe is mounted. Commanding of the stepper motor is performed by a LabVIEW VI which transmits commands over a serial connection to a Norberg BiStep 2A04 stepper motor controller card. This configuration is shown in the figure below.

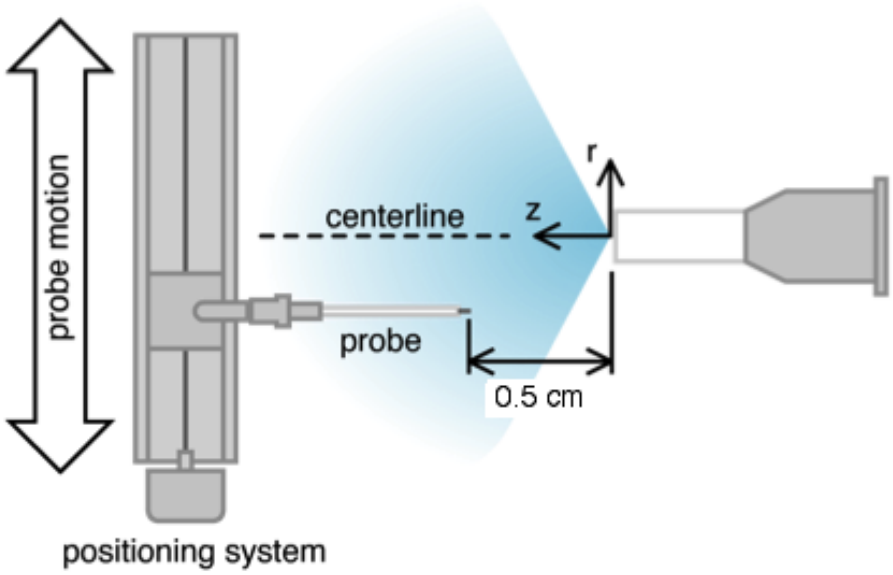

Figure 24: Langmuir Probe Positioning System Schematic [10]

The positioning system does not include any form of encoding or other independent position feedback. Instead, a dead reckoning system is employed. A lever switch is mounted to the track on which the Langmuir probe travels and is actuated when the probe passes over a known position at the start of its traverse. This allows the probe to be reset to the same starting position before every translation across the face of the cathode. The speed of the probe translation is approximately 0.12 cm/s.

This positioning system exhibits high hysteresis, which appears to worsen whenever the discharge is turned on. This means that, while a movement of 9 cm may be commanded, returning to the starting point (as defined by the activation of the limit switch) may require commanding of significantly more or less motion. This makes estimating the position error difficult. The configuration of the vacuum chamber used for these experiments also makes visual confirmation of the probe position uncertain. The only view of the probe is from the radial direction. Instead of relying on knowledge of the absolute position of the Langmuir probe during

the sweeps, the assumption is made that the peak currents will be recorded when the probe is located on-axis in front of the cathode orifice. Measurements at other radial positions are located relative to this point.

3.3.4 Data Acquisition System

Experimental data were recorded for analysis using LabVIEW virtual instruments. A computer fitted with an NI PCI-6024E data acquisition (DAQ) card connected to an SCC-68 terminal block can be used to record high-rate data. The card is capable of collecting up to 250,000 samples per second on a single channel. A GPIB interface is also available which enables communication with a Tektronix TDS-3040 oscilloscope. Measurement circuitry for both the Langmuir and emissive probes is based on that used by Dan M. Goebel at the Jet Propulsion Laboratory. [36].

Use of the Langmuir probe requires collection of both current and voltage. A circuit schematic for the Langmuir probe is presented in Figure 25 below.

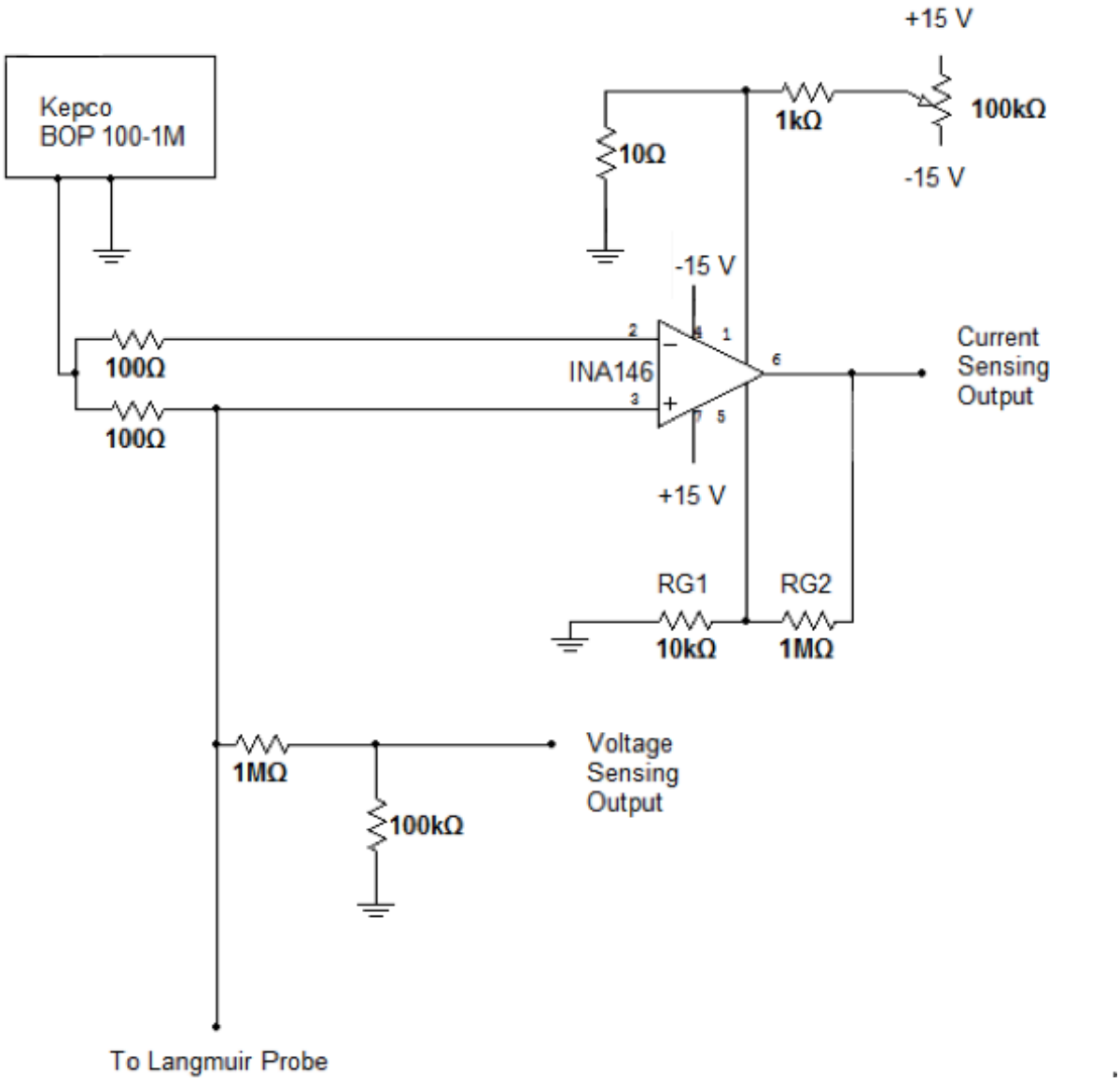

Figure 25: Langmuir Probe Circuit

In this circuit, the probe bias voltage from the Kepco power supply is measured by a simple 10:1 voltage divider. The output from this divider is sent directly to one of the analogue inputs on the National Instruments DAQ card. Current is measured by a 100-Ω shunt resistor and a Texas Instruments INA146 difference amplifier. (For higher bandwidth operation, faster chips such as the Analog Devices AD215 may be substituted.) This difference amplifier measures the voltage drop across the shunt. The output gain is set by the ratio of RG2 to RG1. For these tests,

a gain of approximately 10 was selected. The output of the amplifier is also capable of being trimmed using the 100-kΩ potentiometer. This allows compensation for any bias voltages prior to operation of the probe. The output of the amplifier is connected to a second analogue input on the NI DAQ card. A LabVIEW virtual instrument allows both channels to be sampled at 10 kHz and the results saved to a text file for later analysis. Pertinent parameters for the Langmuir probe data collection are presented in Table 2.

Table 2: Langmuir Probe Operating Data

Probe Translation Rate	0.12 cm/s
Current and Voltage Sampling Rate	10,000 Hz
Spatial Resolution	0.5 mm
Number of Points per Sweep	~2100
Sweep Rate	2.5 Hz

In the case of the emissive probe, presented in Figure 26 below, the circuit consists of an IRF540 MOSFET (metal-oxide semiconductor field effect transistor), capable of supporting a maximum drain to source voltage of 100 V, and a maximum gate to source voltage of 28 V. The MOSFET is connected in the source-follower configuration.. Connected to the gate is the probe input, which runs through a 1-kΩ resistor to protect the probe in the event of failures elsewhere in the circuit [36]. An AA-size battery forward biases the gate so that voltages close to 0 V can be detected. The source of the MOSFET is connected to a 10:1 voltage divider. To prevent improper loading of the MOSFET from the data acquisition system, a buffer amplifier is employed [36]. In this case, an LF411 operational amplifier with noninverting unity gain is used.

Again, the 1-kΩ resistor located on the LF411 output is used to protect against circuit failures that could damage the probe.

The goal of this circuit is have a high input impedance so that the signal recorded from the probe is not perturbed but also to have a low capacitance so that rapid changes in the voltage source can be detected. The circuit achieves this by having an input impedance of more than 10^8 Ω. At the same time, the gate-to-source capacitance is low, allowing the circuit to detect oscillations up to 1 MHz [36].

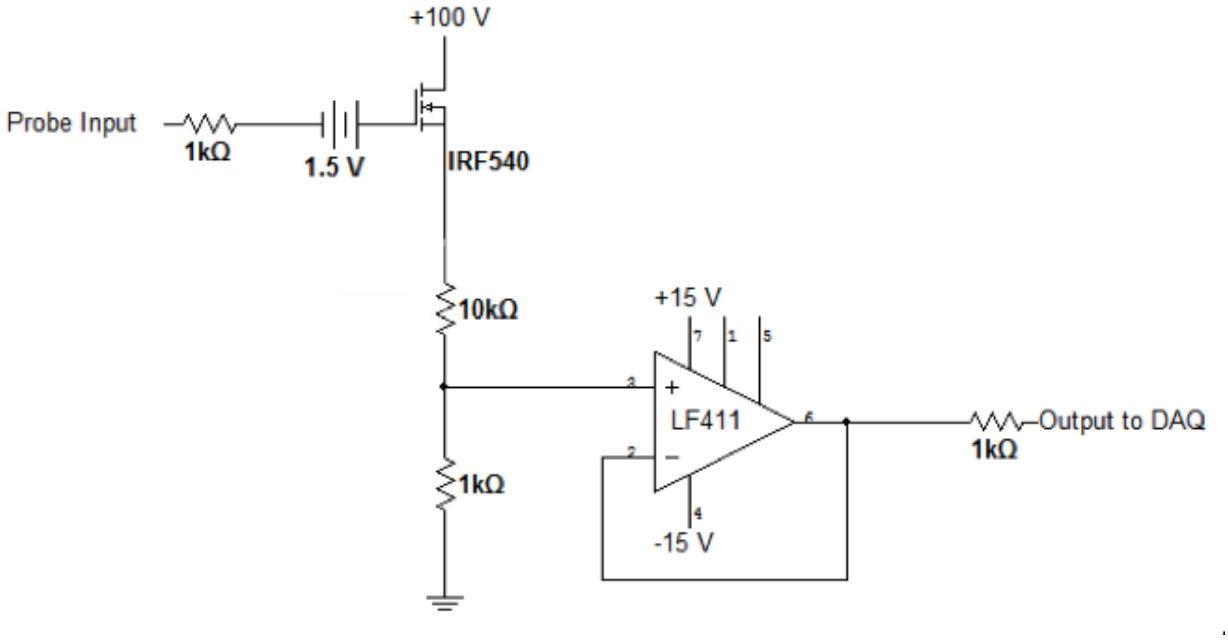

Figure 26: Emissive Probe Circuit

Data from the emissive probe are sampled by a Tektronix TDS-3040 oscilloscope at up to 1 MHz. These data are then downloaded periodically to the computer over a GPIB connection.

4 Results

4.1 Calculation of Distribution Functions

From the Langmuir probe current-voltage characteristic curves, it is possible to compute the electron energy distribution function using the Druyvesteyn method, described in section 2.1.3. This method requires the second derivative of the probe characteristic to be known, which is then directly proportional to the electron energy distribution function by the Druyvesteyn formula.

$$F(\varepsilon) = \frac{4}{e^2 A_p}\left(\frac{mV}{2e}\right)^{1/2} \frac{d^2 I}{dV^2} \qquad (82)$$

where e is the elementary charge, A_p is the exposed area of the Langmuir probe, m is the electron mass, and V is the applied probe bias voltage, measured with respect to the plasma potential. The units of this non-normalized distribution are $J^{-1}m^{-3}$.

Numerical differentiation of the collected probe signal is an inherently noisy process, and smoothing and filtering techniques are often required to extract a usable data set. A typical Langmuir probe I-V trace obtained from this cathode and containing approximately 2100 data points appears in Figure 27 below.

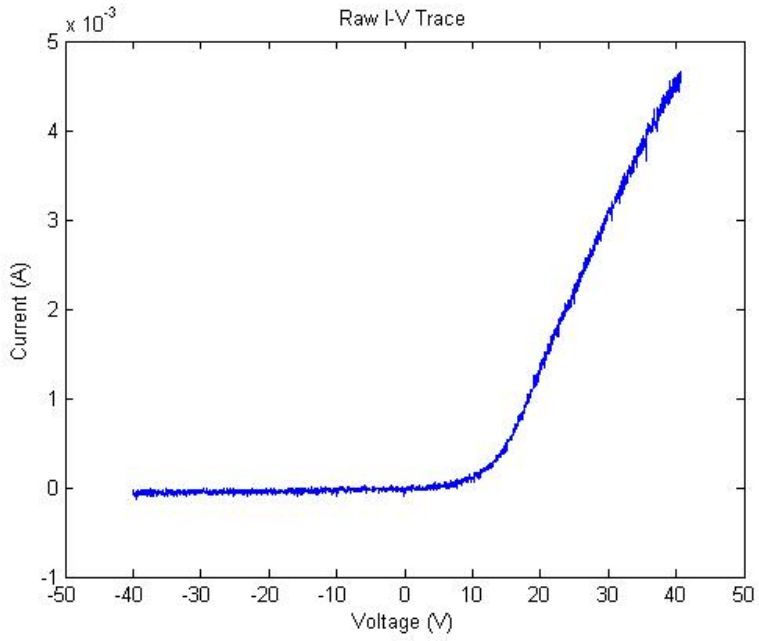

Figure 27: Current-Voltage Trace before Processing

Two features are immediately apparent in these raw data. First, there is a significant amount of noise superimposed on the signal. This takes the form of a visible "hash." Attempting to numerically differentiate the data in this form produces extremely noisy results, which makes the EEDF computed by the Druyvesteyn method virtually useless. Consequently, some means of eliminating this noise had to be developed. Using MATLAB's signal processing toolbox, a nine-stage Butterworth low-pass filter with a cutoff frequency of 350 Hz was implemented to provide the initial filtering of the data (MATLAB function `butter`). A software filter was selected over a hardware filter both for ease of implementation and for the ability to adjust the filtering parameters quickly during processing. The Butterworth filter design provides the flattest possible frequency response in the passband, which is desirable in order to prevent distortion of the desired signal [37]. Ordinarily, Butterworth filters have a relatively slow response roll-off rate in the stopband. Because this filter was implemented in software, this disadvantage could be compensated for by selecting a very high-order filter, which would otherwise be impractical to

build in hardware. The cutoff frequency was selected in order to filter as much of the noise as possible without changing the shape of the underlying I-V curve. This was determined by visual inspection of the processed the data with multiple filter designs. Fourier analysis also revealed a large peak at 800 Hz, which is successfully eliminated by this filter. After filtering, a typical I-V trace takes the following form.

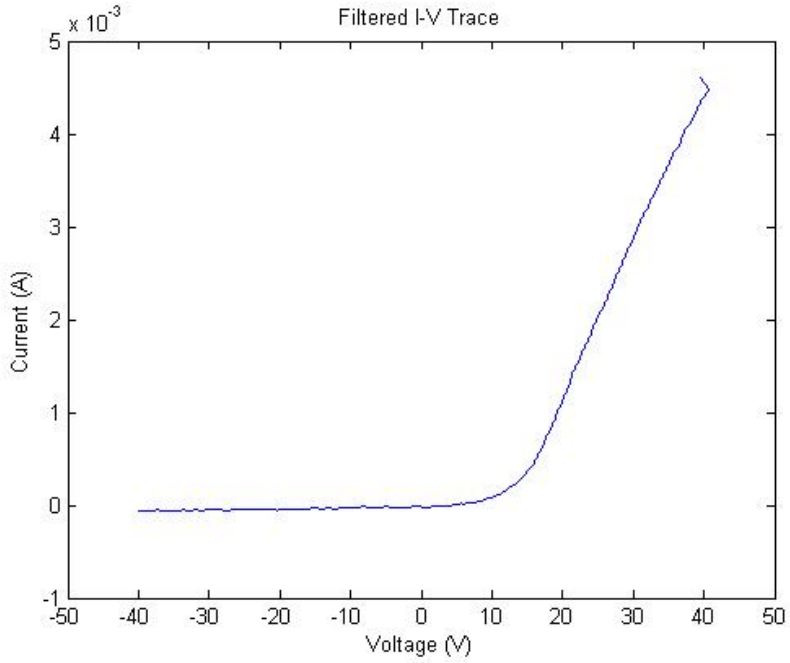

Figure 28: Filtered I-V Trace

It is apparent that much of the visible "hash" in the data has been eliminated just by applying the Butterworth filter. However, ripples are still plainly visible, particularly in the ion saturation region, that will disrupt the process of numerical differentiation. Consequently, prior to differentiation, a smoothing algorithm was needed. In this case, a simple boxcar moving-average algorithm using 120 points (out of approximately 2,100 points collected in each sweep) was used (MATLAB function `smooth`) [38]. Other techniques, such as Savitzky-Golay smoothing, were tried but were found to produce inferior results. The I-V curve following the application of smoothing is shown in Figure 29.

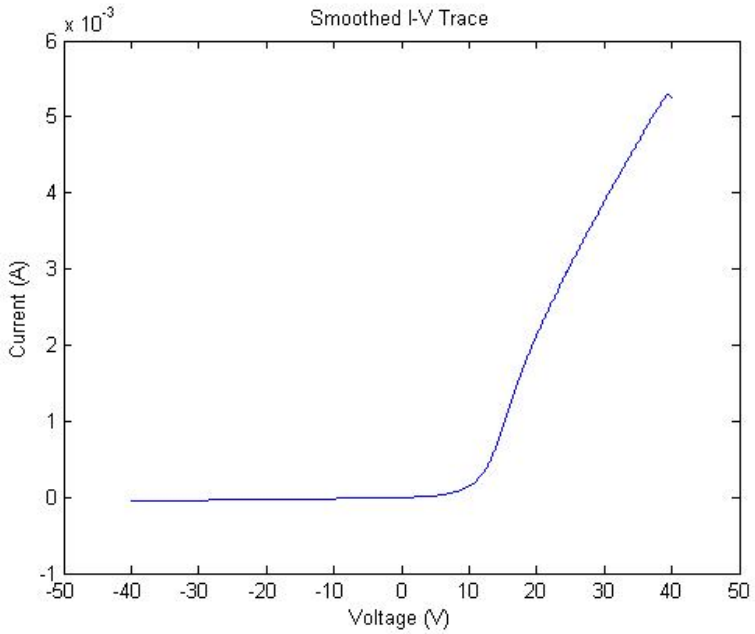

Figure 29: Smoothed I-V Trace

Next, the I-V characteristic was numerically differentiated using second-order finite difference approximations. As numerical differentiation has the unfortunate tendency to amplify any noise present in the signal, the I-V characteristic was smoothed again using the same algorithm after the first differentiation step. The following figures illustrate this process. Figure 30 shows the first derivative, and Figure 31 shows the first derivative after smoothing has been applied. The noise removed by the smoothing process is clearly visible.

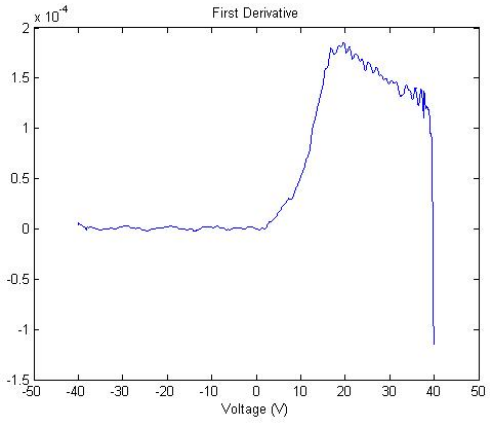

Figure 30: First Derivative of I-V Trace

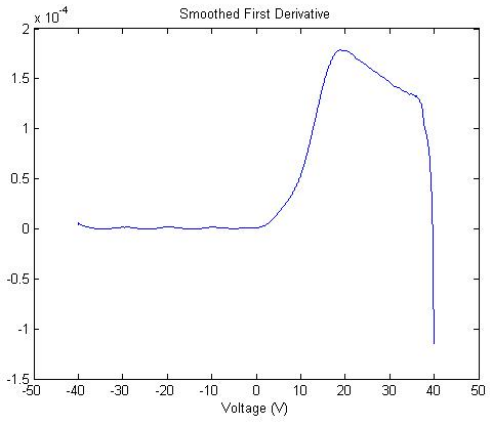

Figure 31: Smoothed First Derivative

The final step before calculation of the electron energy distribution function can proceed is the calculation of the second derivative. This is again performed numerically using second-order finite difference approximations. A typical second derivative appears in Figure 32 below.

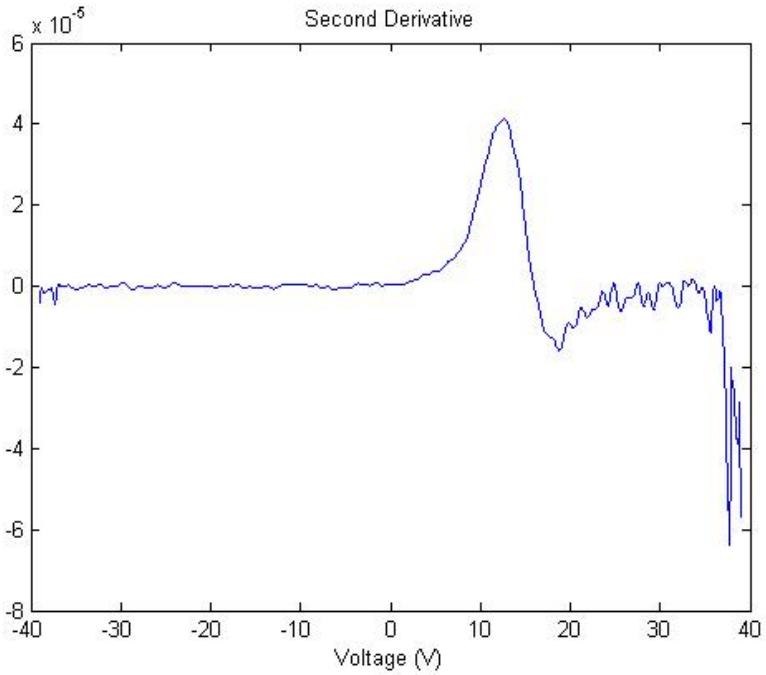

Figure 32: Second Derivative of I-V Trace

Finally, further smoothing is applied to the second derivative in order to eliminate the noise that was amplified during the differentiation process In order to preserve as many features

as possible, this level of smoothing is much less than that applied to the first derivative and includes only 50 points. A typical smoothed second derivative is shown below.

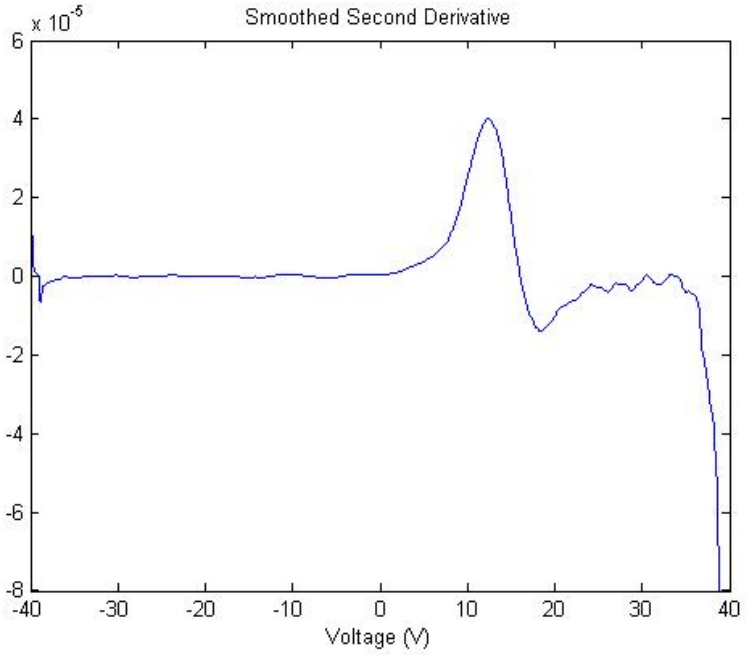

Figure 33: Smoothed Second Derivative

With the second derivative known, the Druyvesteyn formula is applied to calculate the electron energy distribution function.

4.2 Determination of Plasma Parameters

There are several probe analysis methods that can be used to calculate the plasma potential, the plasma density, and the electron temperature. The three that were used in this analysis were thin-sheath theory, orbital motion limited (OML) theory, and the direct application of kinetic theory to the electron energy distribution function.

In order to apply the thin-sheath method, the Langmuir probe I-V trace must be plotted on a semilog plot. This allows the determination of the electron temperature from the slope of the exponential region of the curve. Because the thin-sheath method relies on a relationship for the electron current only, accurate calculations must include the subtraction of the ion saturation

current, extrapolated to the electron collection region of the curve. After this current has been subtracted, the natural logarithm of the current is plotted against the probe bias voltage. The resulting plot is approximately a straight line. The slope of this line is then computed, which yields the electron temperature in eV directly. A sample plot showing the electron saturation region and the best fit line is shown in Figure 34 below.

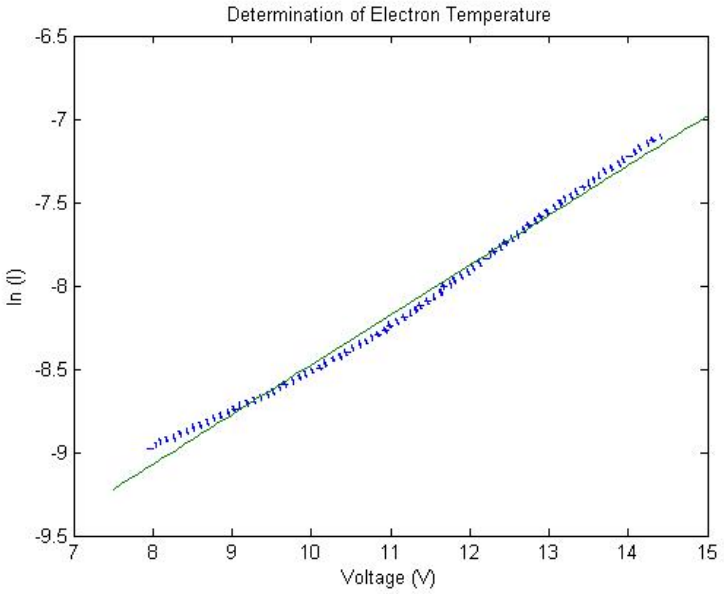

Figure 34: Electron Temperature Determination

As discussed previously, thin-sheath theory has a limited region of applicability. Chen suggests that the ratio of the probe radius to the Debye length should be greater than ten to obtain reliable results [20]. For the two argon propellant flow rates, the following plasma parameters were obtained. The density is calculated using Equation (52) and the Debye length from Equation (17).

Table 3: Debye Length and Mean Free Path Calculated Using Thin Sheath Theory (argon)

Case	n_e (m^{-3})	T_e (eV)	$\lambda_D(m)$	r_p / λ_D	λ_{ei} / d_p	λ_{en} / d_p
Nominal Flow	3.09×10^{17}	2.99	2.31×10^{-5}	1.65	8.90×10^{3}	1.03×10^{5}
Low Flow	3.14×10^{17}	3.53	2.49×10^{-5}	1.53	1.19×10^{4}	1.01×10^{5}

While the collisionality condition is met (the mean free path for electron-ion and electron-neutral collisions is much larger than the probe diameter), the probe radius is just barely larger than the Debye length itself. Consequently, the sheath cannot be assumed to be thin, and the requirements for thin-sheath theory are not met.

The second ion collection theory that may apply to this situation is the orbital motion limited (OML) theory. Because the available I-V traces do not display an electron saturation region, the theory must be applied to the ion saturation region of the I-V trace. In that case, the square of the collected current is plotted against the applied probe bias voltage. From equation (62), the slope of this curve may be solved for the ion density. Since the quasineutrality condition is assumed to hold throughout the bulk plasma, this gives the electron density directly. Equation (83) is the applicable expression for the ion density, derived from the slope of equation (62).

$$n_i = \sqrt{\frac{d\left(I^2\right)}{dV_p}}\sqrt{\frac{M_i}{2e}}\frac{\pi}{eA_p} \qquad (83)$$

A typical plot of the square of the collected current in the ion saturation region of the probe characteristic appears in Figure 35.

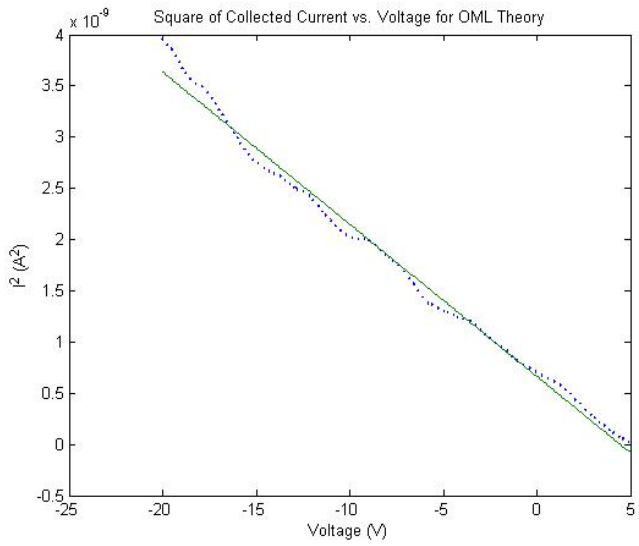

Figure 35: Curve Fit to Square of Ion Saturation Current for OML Theory

The implementation of OML theory is more difficult than for the thin-sheath theory. In the ion saturation region, the currents are extremely small, and squaring them makes them smaller still. Consequently, any noise present in the collected I-V characteristic may serve to introduce uncertainty in the slope calculation. In some collected traces, this region shows two or more distinct linear regions, and it is sometimes unclear which is most applicable to the OML method. An example of this phenomenon appears in Figure 36.

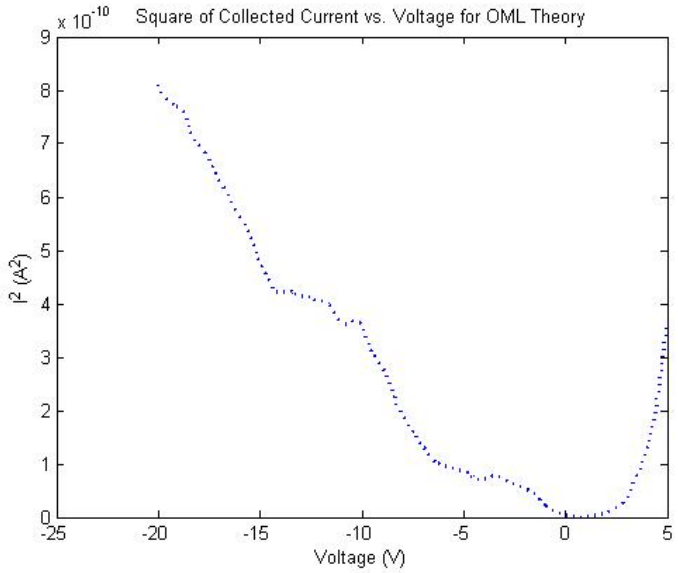

Figure 36: Difficult to Interpret Ion Saturation Region

Another important limitation of the OML theory is its inability to compute the electron temperature for the conditions encountered in this experiment. Because the only region suitable for analysis is the ion saturation part of the I-V curve, there is no capacity to extract the electron temperature based purely on the OML theory. If an electron saturation region were present in the collected I-V traces, then equation (61) could be applied to this region as described in section 2.1.2. In order to determine whether OML is a valid theory, the Debye length must again be computed. For this computation, the electron temperature was taken to be equal to the value derived from the slope of the exponential region of the curve as described above and presented in Table 3. For two different propellant flow rates, the following results were obtained.

Table 4: Debye Length and Mean Free Path Calculated Using OML Theory (argon)

Case	n_e (m^{-3})	T_e (eV)	$\lambda_D(m)$	r_p / λ_D	λ_{ei} / d_p	λ_{en} / d_p
Nominal Flow	6.80×10^{16}	n/a	4.93×10^{-5}	0.773	3.78×10^{4}	4.68×10^{5}
Low Flow	1.00×10^{17}	n/a	4.40×10^{-5}	0.866	3.56×10^{4}	3.18×10^{5}

Again, the collisonality condition is met, and the calculated ratio of the probe radius to the Debye length is less than three. This indicates that OML is a valid theory for these plasma conditions.

A third method for the computation of the plasma parameters is to use the electron energy distribution function, which may be calculated from the Druyvesteyn formula and the second derivative of the probe characteristic as described in Section 2.1.4. This method has the advantage of being applicable regardless of the size of the sheath. The primary disadvantage of the Druyvesteyn method is the need to calculate the second derivative of the I-V curve numerically. This process amplifies any noise present in the signal and requires repeated applications of smoothing in order to obtain usable results.

In order to use the Druyvesteyn formula, the plasma potential must be known. This is necessary because the Druyvesteyn method assumes that the applied probe bias potential is measured with respect to the plasma potential. In many cases, it is possible to determine the plasma potential directly from the I-V characteristic by locating the knee that marks the transition from the exponential region to the electron saturation region. In the case of this cathode, however, the collected I-V traces do not display an easily discernable knee. Consequently, additional processing is needed to extract an estimate of the plasma potential. Several methods can be used.

The first method applied involves plotting the natural logarithm of the measured current against the probe bias voltage. This allows the exponential region to be more easily observed. Lines drawn to fit the exponential and electron saturation regions are then plotted. Their intersection can be used to obtain an estimate of the plasma potential. A typical I-V trace showing the application of this method is shown in Figure 37 below.

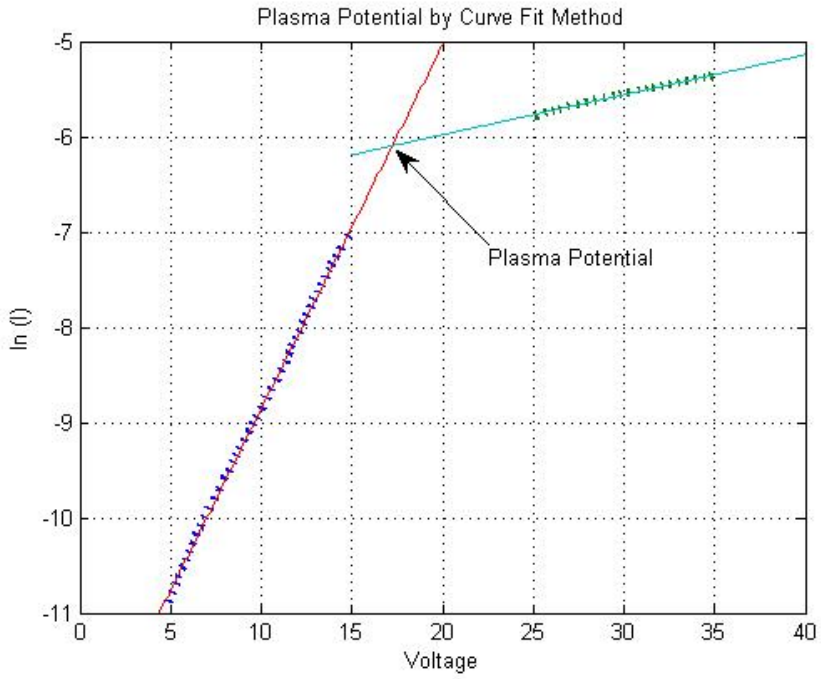

Figure 37: Determination of Plasma Potential by Curve Fit Method

The plasma potential may also be located by finding the maximum of the computed first derivative. This method may not always produce reliable results due to the presence of noise in the data. To reduce this possibility, the search area for the plasma potential was restricted to a relatively small window around the value computed from the curve fit method described above. A sample first derivative plot is available in Figure 38 below, with the location of the maximum and probable plasma potential labeled.

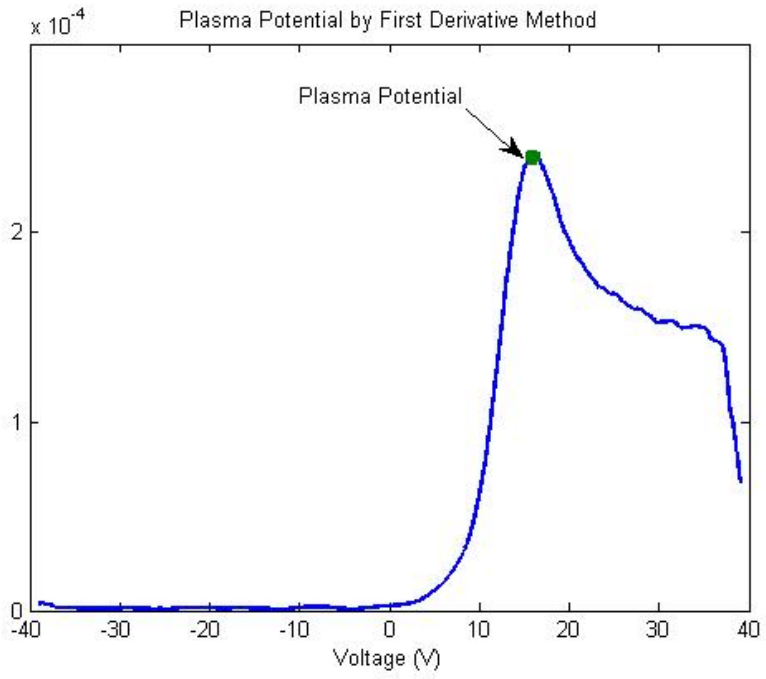

Figure 38: Determination of Plasma Potential by First Derivative Method

Finally, the computed second derivative may also be used to determine the plasma potential. Unfortunately, as this represents the most heavily processed data set, the reliability of this method is sometimes less than the other two. This method is illustrated in Figure 39.

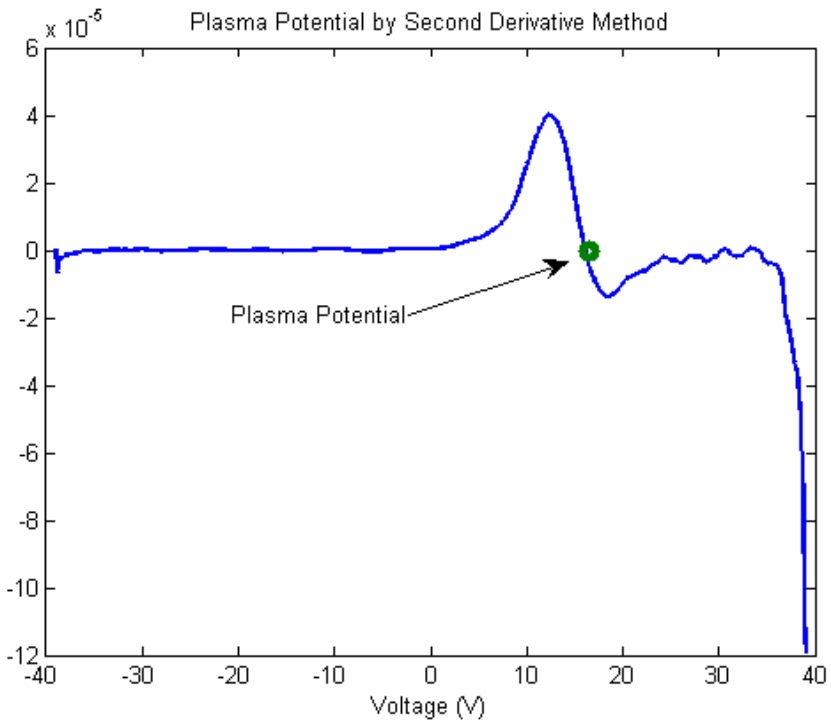

Figure 39: Determination of Plasma Potential by Second Derivative Method

In general, the estimated plasma potential is taken to be the average of the values produced by these three methods. If one measurement happens to disagree significantly with those from the other two methods, it is discarded, and the analysis proceeds using the mean of the remaining estimates. The plasma potential calculated by the curve fit method becomes significantly more unreliable as radial distance from the cathode is increased. Consequently, this processing technique is not used except for the on-axis centerline position. Conversely, the plasma potentials calculated by the first- and second-derivative methods show good agreement, typically within 1 V, and these methods were used for all of the data presented in the following sections.

In addition to using the Langmuir probe I-V characteristic to obtain the plasma potential, the emissive probe can also be used for this purpose. The emissive probe has the added advantage of requiring no complex data processing to extract the potential measurement. Instead,

the probe will naturally float to a potential near that of the plasma, and this value can be read directly from the recorded voltage vs. time curve. Because the emissive probe is mounted in a different location and does not translate with the Langmuir probe, however, it is not possible to use the measured plasma potential from the emissive probe in the calculation of the other plasma properties. The plasma potential can change dramatically with both radial and axial position relative to the cathode orifice, and it is therefore necessary to rely solely on the Langmuir probe data in order to keep the analysis internally consistent.

Once the plasma potential is known and the electron energy distribution function has been calculated, it is possible to obtain the electron temperature and the plasma density by integrating the distribution function. A typical EEDF, calculated using Equation (82), appears in Figure 40 below.

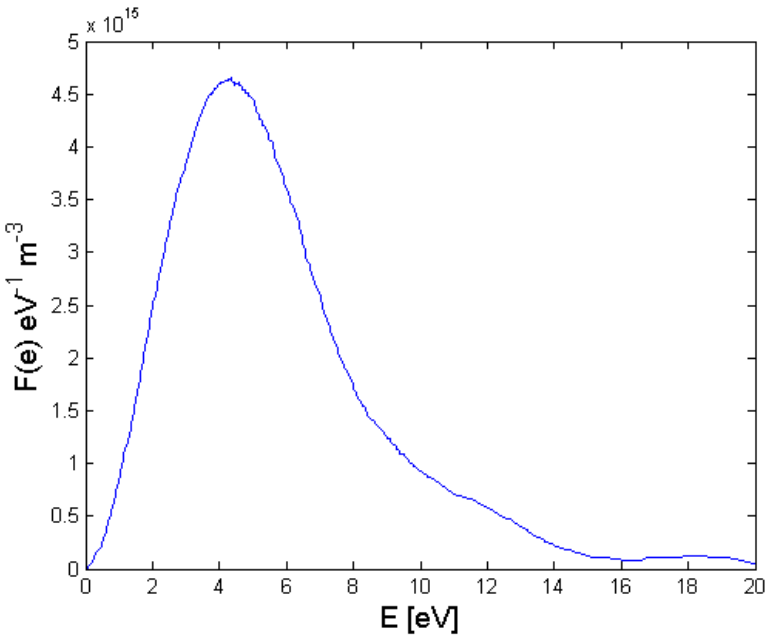

Figure 40: Example Electron Energy Distribution Function

Once the EEDF is known, the plasma density and electron temperature follow from kinetic theory, where the energy distribution function has units of $J^{-1}m^{-3}$, the density is in m^{-3}, and the temperature is in eV.

$$n_e = \int_0^\infty F(\varepsilon)d\varepsilon \tag{84}$$

$$T_e = \frac{2}{3}\frac{1}{n_e}\int_0^\infty \varepsilon F(\varepsilon)d\varepsilon \tag{85}$$

4.3 Uncertainty in Measured Plasma Parameters

All of the methods used to determine the plasma potential, electron temperature, plasma density, and electron energy distribution function have some inherent uncertainties. The accuracy of the results obtained from the thin-sheath and OML theories can be difficult to determine precisely. A common practice is to assume errors of up to 20% for the electron temperature and 50% for the number density [39]. While these appear to be very high, it is important to note that

the errors are expected to be consistent across all of the measurements. Consequently, these methods can be used to compare the densities and electron temperatures for various radial positions and propellant flow rates, with the reasonable expectation that the trends appearing in the data will be true, even if the absolute values are not known to a high degree of accuracy.

For emissive probes used to measure the plasma potential by the floating probe technique, it is anticipated that the floating potential will be within 1 T_e of the actual plasma potential. Consequently, as the electron temperature varies, so will the uncertainty of the plasma potential indicated by this method. From the measurements of the electron temperature presented, the uncertainty in the plasma potential measured by the emissive probe is approximately 5-10 V. For this experiment, however, it is of greater interest to observe changes in the plasma potential as a function of time and propellant flow rate—the absolute value is of lesser significance.

The electron energy distribution functions were calculated by the Druyvesteyn method, which requires that numerical differentiation be used. This process tends to amplify any noise present in the measured signal. In many studies, this problem is mitigated by averaging several probe traces or distribution functions collected in the same location. For example, Herman averaged a minimum of 20 probe traces for each location when calculating the electron energy distribution function [40]. This proved impossible for this research because of the inability to position the Langmuir probe accurately and repeatedly. Consequently, the distribution functions shown in the following sections contain a significant amount of noise, especially in the high-energy tail. This has implications for the calculation of the electron temperature and plasma density as well as the ionization instability frequency. In this region of the distribution function, it is likely that any usable signal is overwhelmed by the presence of this noise. In many cases, the

distribution function even becomes negative. For a typical EEDF calculated for this experiment, the total negative area is approximately 10% of the total area under the distribution function. Negative probabilities are certainly nonphysical, and this feature represents a significant source of uncertainty for the results calculated from the EEDF.

Also affecting the use of the Druyvesteyn method is the uncertainty associated with the plasma potential. The lack of a distinct knee in the I-V trace makes interpretation of this data set more difficult. While the first- and second-derivative methods used to determine the plasma potential agreed well with each other (usually within 1 V), the plasma potential itself is still not known to high degree of accuracy. There is no independent means of verifying this parameter.

4.4 Results for Argon Propellant

For this experiment, the Langmuir probe was used to collect data at several different radial positions. The resulting I-V traces were analyzed to obtain the electron energy distribution functions, the plasma potential, the electron temperature, and the plasma density. In addition to the variation with spatial position, variations with propellant flow rate were also considered. Two cases were considered, one at "nominal" operating conditions and another at approximately 10-14% of the nominal propellant flow rate. These flow rates were the lowest at which the cathode could reliably be operated. The majority of the testing was done using argon, and the axial position of the Langmuir probe was fixed at approximately 5±1 mm from the keeper orifice.

For the nominal case, Figure 41 presents the electron energy distribution function for several radial positions. The gray labels indicate the radial position of the probe in centimeters. The center position, aligned with the orifice, is at 0 cm.

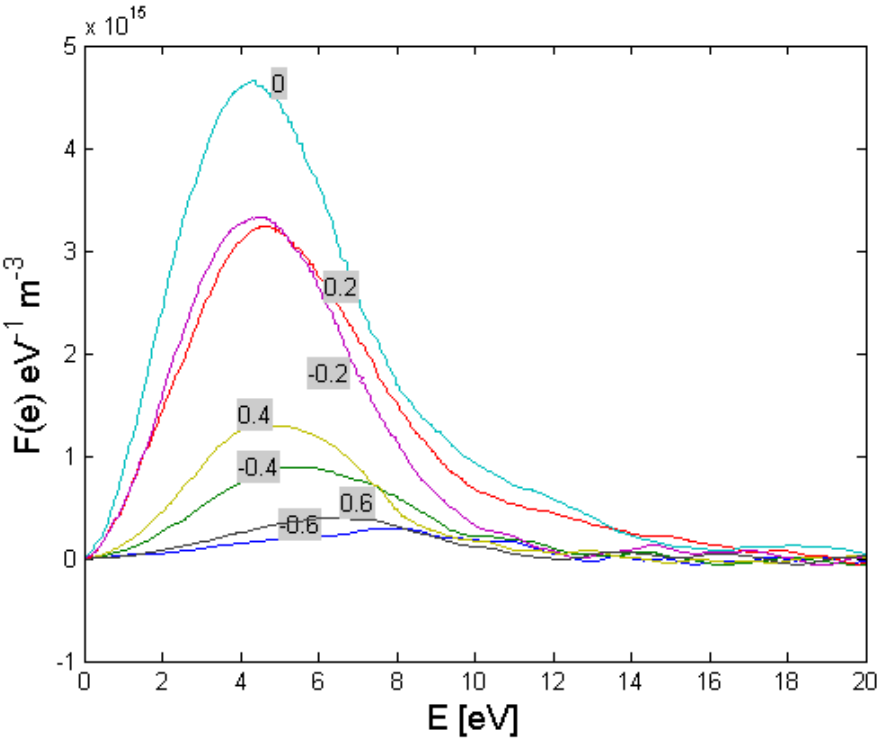

Figure 41: Radial Variation of Electron Energy Distribution Function (Ar Nominal Case)

The peak of the distribution shifts toward higher energies as radial distance from the orifice increases. This corresponds to an increase in the average electron temperature.

For the lower flow rate Case 2, a similar plot can be obtained.

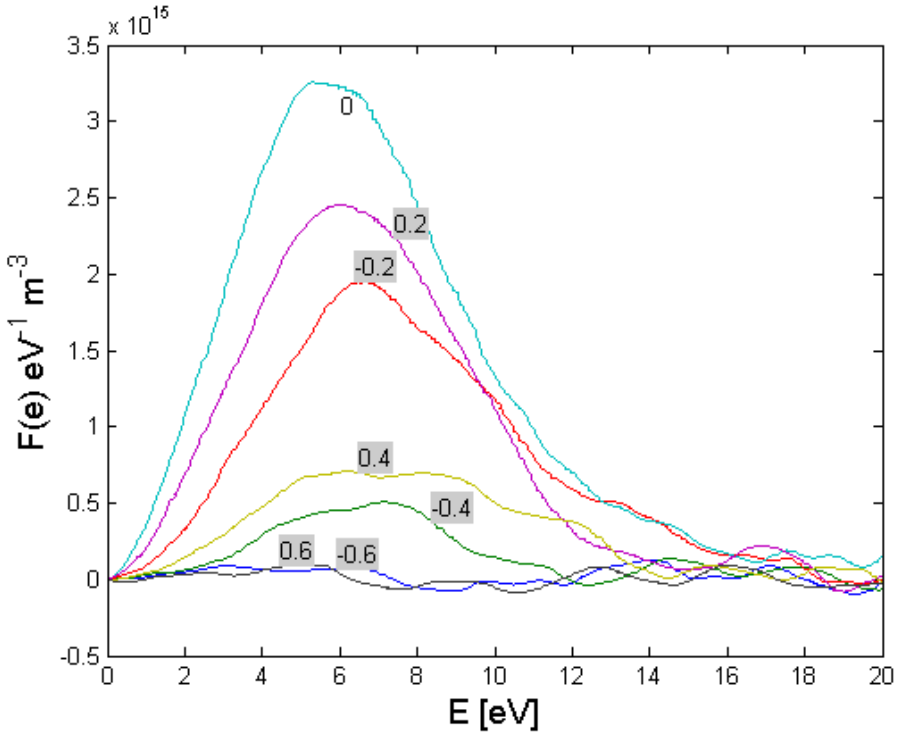

Figure 42: Radial Variation of Electron Energy Distribution Function (Ar Low-Flow Case)

There is some asymmetry present in both plots—distribution functions measured at the same radial offset but in opposite directions have a significant difference in their magnitudes. Here, it is apparent that the main peak of the distribution function has been shifted to higher energies. This trend is more readily apparent in Figure 43, in which the distribution function at the two different propellant flow rates for the same (centerline) radial position is plotted. All measurements were taken at the centerline position.

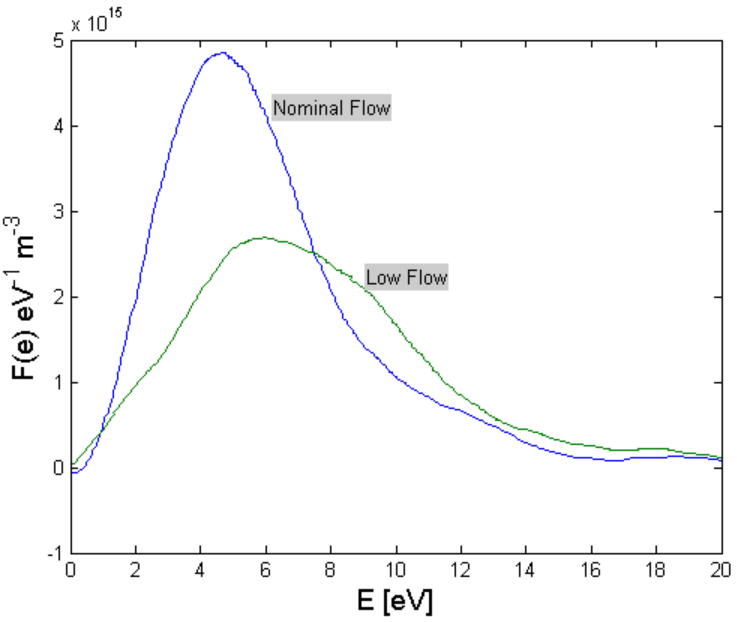

Figure 43: Comparison of EEDF at Two Argon Flow Rates

It is very clear that the mode of the distribution function is shifted to higher energies as the flow rate is reduced. The peak moves from approximately 4.2 eV to 6 eV.

It is also possible to examine the behavior of the plasma potential as a function of radial position. Measurements were made at ±5 mm from the cathode centerline, as data collected from beyond this point proved too noisy to process reliably. Figure 44 and Figure 45 below show this variation for both of the cathode operating conditions considered in this experiment. The trend in each case is largely comparable, with the lowest plasma potentials being measured for probe positions on the centerline of the cathode. The plasma potential there is approximately 16 V for the nominal flow case, rising to nearly 17 V for the low flow case. Greater differences in the magnitude of the plasma potential are observed as the probe translates radially. For the nominal flow case, the maximum observed was less than 20 V, while the low flow case shows potentials greater than 21 V for the same radial distance from the cathode. Also interesting is that both cases show an abrupt increase in the plasma potential near the centerline. Furthermore, the side of the cathode on which this abrupt increase occurs is inverted for the low flow-rate case.

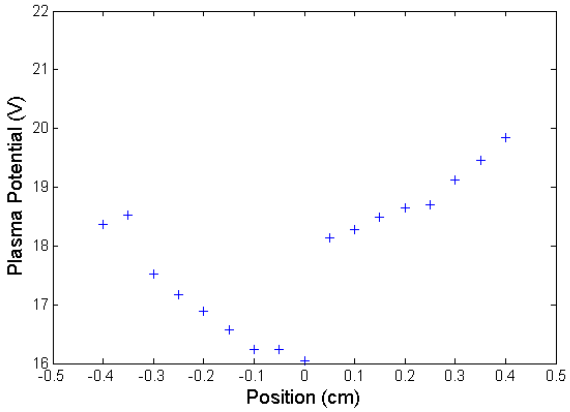

Figure 44: Plasma Potential vs. Radial Position (Ar Nominal Flow Case)

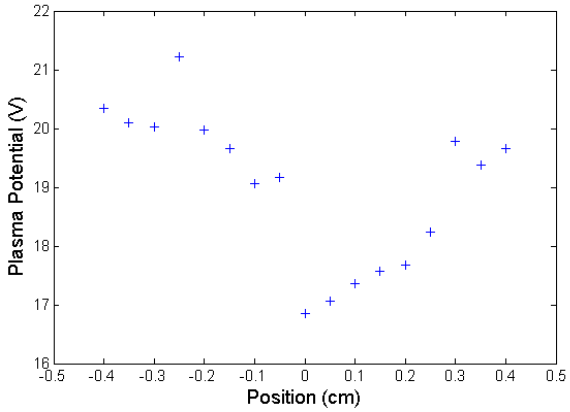

Figure 45: Plasma Potential vs. Radial Position (Ar Low-Flow Case)

The electron temperature was computed using two different methods. The first applies classical probe theory to the exponential region of the I-V characteristic. The slope of the natural logarithm of the current in this region gives the electron temperature directly (the "Slope Method"). From Equation (85), it is also possible to compute the electron temperature from the EEDF by integration (the "EEDF Method"). The variation of the electron temperature with radial position for the two cathode operating regimes, computed using the two available methods, is shown in the following figures.

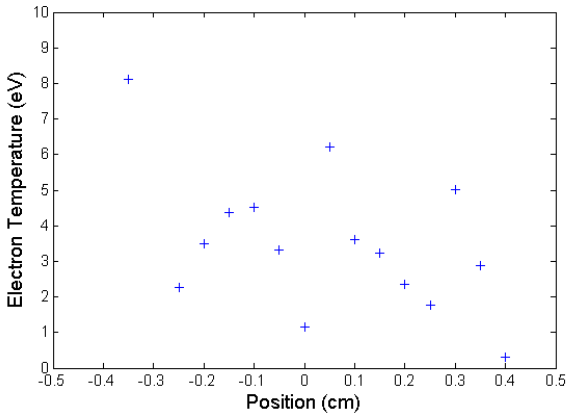

Figure 46: Electron Temperature vs. Radial Position (EEDF Method for Ar Nominal Flow Rate)

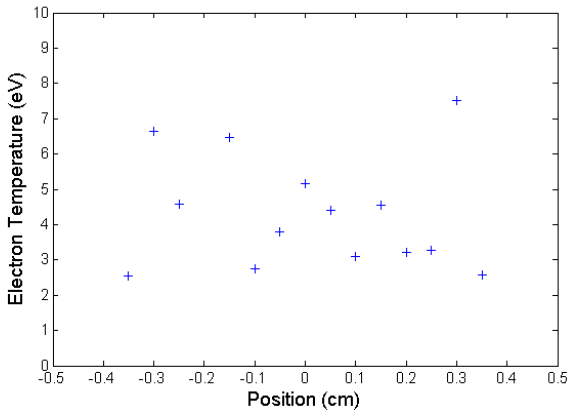

Figure 47: Electron Temperature vs. Radial Position (EEDF Method for Ar Low Flow Rate)

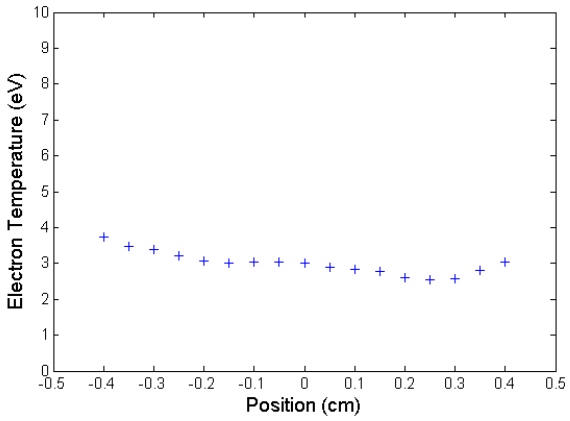

Figure 48: Electron Temperature vs. Radial Position (Slope Method for Ar Nominal Flow Rate)

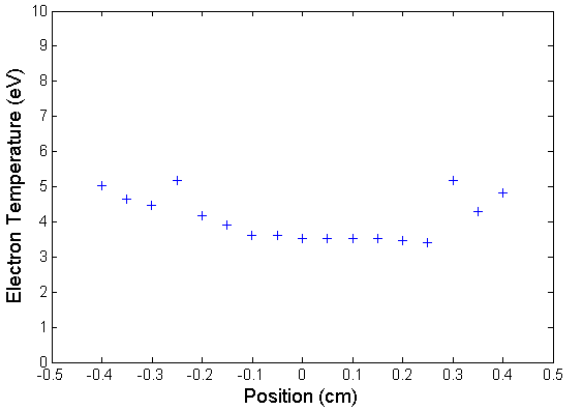

Figure 49: Electron Temperature vs. Radial Position (Slope Method for Ar Low Flow Rate)

Significant differences in the estimated temperature are apparent, particularly with respect to the amount of scatter. There is much more variation in the electron temperatures computed by the EEDF method. Interestingly in the curves produced by the slope method, the minimum electron temperature is reached nearly 2 mm beyond the assumed centerline. The curves are somewhat asymmetric. The lower flow rate operating point shows generally higher electron temperatures. This trend is visible in the electron temperatures obtained by both methods. Both methods also agree on the general magnitude of the electron temperature, which is approximately 3 eV in front of the orifice for the nominal case, and a bit higher, between 3.5

and 4 eV, for the low-flow case. Moving radially from the centerline, the electron temperature increases to above 5 eV in the low-flow rate case.

The plasma density was also computed using two different methodologies. As OML theory was deemed to be applicable to these measurements, it can be used to estimate the plasma density. Kinetic theory also allows the density to be computed through integration of the electron energy distribution function, as shown in Equation (84). The variation of plasma density with radial position is shown for the two flow rate cases, computed by the two analysis methods.

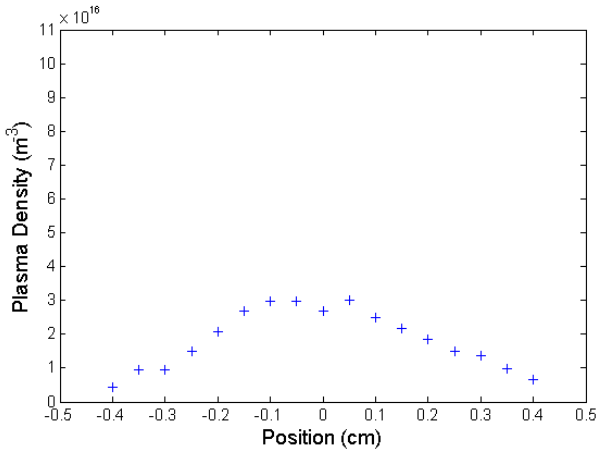

Figure 50: Plasma Density vs. Radial Position (EEDF Method for Ar Nominal Flow Rate)

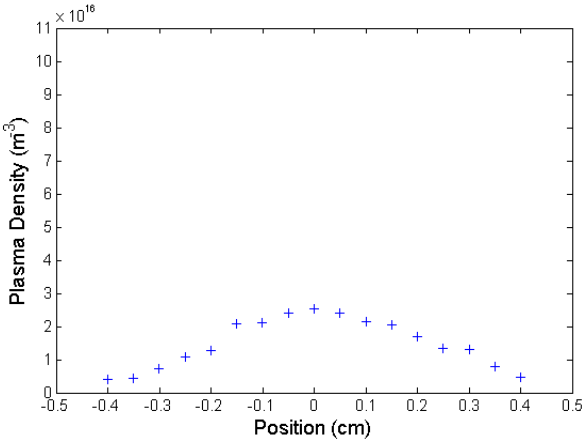

Figure 51: Plasma Density vs. Radial Position (EEDF Method for Ar Low Flow Rate)

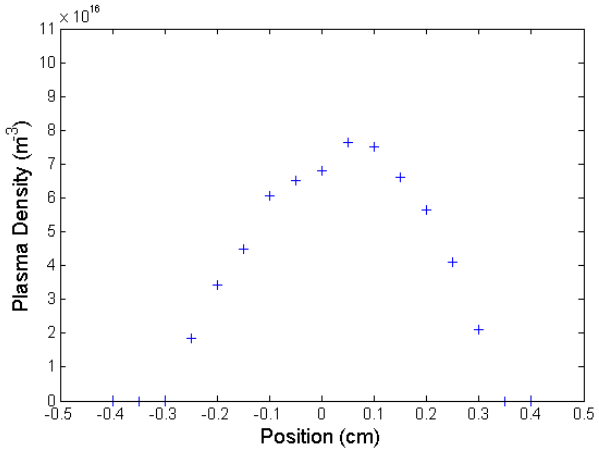

Figure 52: Plasma Density vs. Radial Position (OML Method for Ar Nominal Flow Rate)

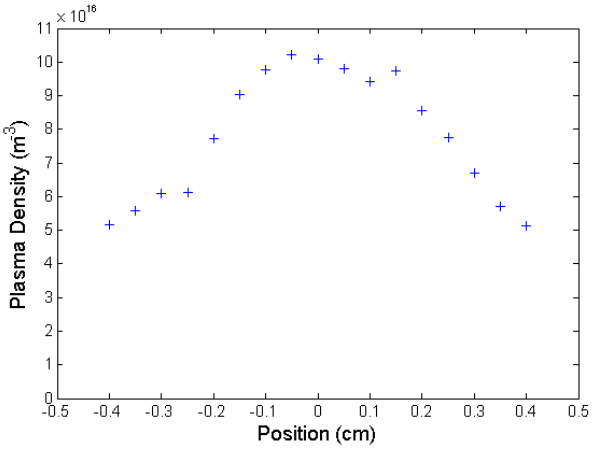

Figure 53: Plasma Density vs. Radial Position (OML Method for Ar Low Flow Rate)

The plasma density variation is symmetric about the presumed centerline position as expected. The densest parts of the plume should be near the cathode orifice. Analysis using the OML theory produces results that show higher plasma densities overall. As the flow rate is reduced, the density decreases according to the analysis computed with the electron energy distribution function. When OML theory is used, the density trend is reversed, showing increased densities for a lower flow rate. However, all of the density measurements are of the same order of magnitude—approximately 10^{16} m^{-3}. Given the inherent uncertainty associated with

processing the energy distribution functions and applying OML theory, it may be assumed that there is very little change in plasma density associated with the propellant flow rate.

While the Langmuir probe can be used to extract information about the plasma potential at several positions relative to the cathode orifice, it is unable to measure any high-frequency oscillations in the plasma potential. It has been theorized and observed that the magnitude of these oscillations may lead to the production of high-energy ions which contribute to the erosion of cathode surfaces [5]. To determine whether such oscillations exist, the emissive probe with a high-speed data acquisition system was used. For approximately the same cathode operating conditions as previously described for the Langmuir probe measurements, the emissive probe was used in the floating mode to record the plasma potential as a function of time at an axial distance of approximately 7±1 mm from the cathode orifice. It was expected that reductions in the propellant flow rate would lead to noisier operation. This transition would be manifested as an increased peak-peak voltage measured by the emissive probe.

In order to produce accurate measurements of the plasma potential, it is necessary for the emissive probe to be strongly emitting electrons. The floating potential of the probe will asymptotically approach the plasma potential as the heater current through the emissive probe is increased. Prior to any data being collected, the heater power was gradually increased and the floating potential monitored to ensure this condition was satisfied. A plot of the floating potential as a function of heater current is shown in Figure 54.

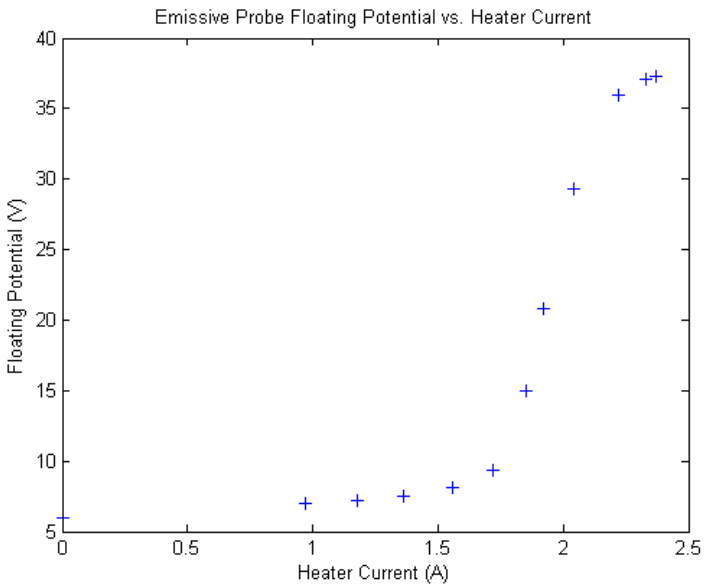

Figure 54: Emissive Probe Floating Potential vs. Heater Current (Argon)

The heater current was not increased very far into the asymptotic region in order to preserve the life of the filament. From experience, it was known that a current of approximately 2.7 A was required to melt the 0.0035-inch (88.9-micron) tungsten wire used as a filament. The current required for strong emission was approximately 2.4 A.

For the nominal operating conditions, the plasma potential as a function of time is displayed in Figure 55. The corresponding power spectral density estimate (in decibels referenced to 1 V^2) is shown in Figure 56.

The mean plasma potential measured by the emissive probe was 38.2 V for this case. The maximum peak-to-peak voltage was 31.2 V. The frequency spectrum is unremarkable, with few features of interest.

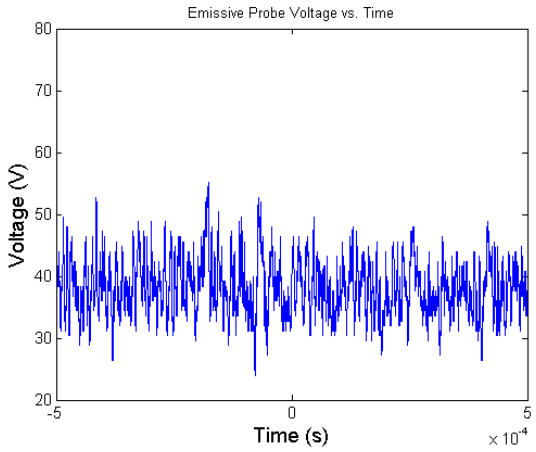

Figure 55: Plasma Potential vs. Time (Ar Nominal Case)

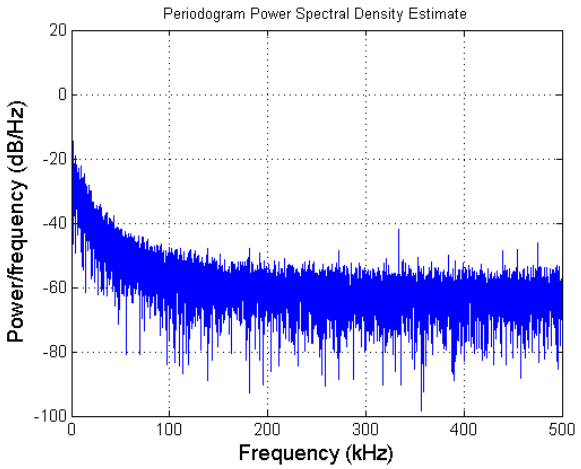

Figure 56: Power Spectral Density Estimate for Plasma Potential (Ar Nominal Case)

When the flow rate was reduced to the low-flow case, however, the behavior of the plasma potential changed quite dramatically. Figure 57 shows the time history of the measured plasma potential, and Figure 58 shows the power spectral density estimate.

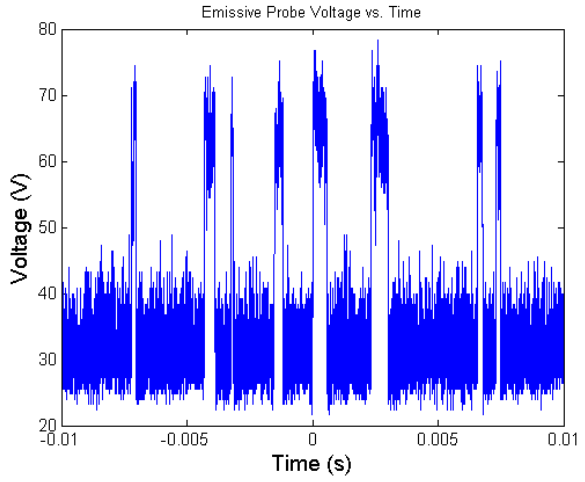

Figure 57: Plasma Potential vs. Time (Ar Low-Flow Case)

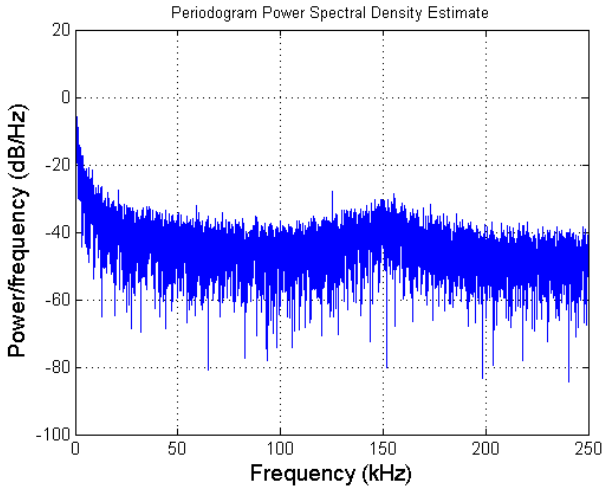

Figure 58: Power Spectral Density Estimate for Plasma Potential (Ar Low-Flow Case)

Here, the mean plasma potential is measured to be 35.8 V, and the maximum peak-to-peak voltage was 56.8 V, nearly double that of the more quiescent nominal operating condition. These very large oscillations are clearly visible in the time history, and the frequency spectrum shows a peak at approximately 150 kHz which was not present at the nominal operating point.

In order to characterize the transition of the cathode from the quiescent mode to the noisier mode at lower flow rates, emissive probe data were recorded at several intermediate flow rates. Figure 59 shows the variation of the maximum peak-to-peak voltage with flow rate, normalized to the nominal operating condition.

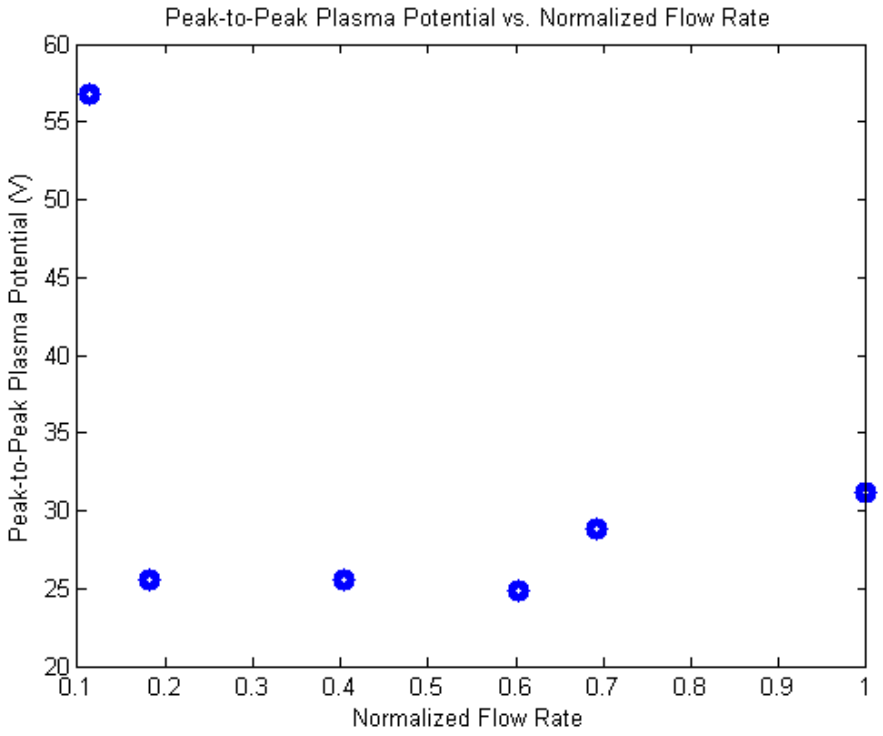

Figure 59: Peak-to-Peak Plasma Potential vs. Flow Rate (Argon)

The transition from the relatively quiescent mode of operation to the noisier mode is relatively abrupt, occurring at about 11% of the nominal flow rate. Until that point, the maximum peak-to-peak voltage remains within the range of 25-32 V. This transition may represent the switching of the cathode from spot mode to plume mode. Future tests will include monitoring of the discharge voltage oscillations on an oscilloscope to confirm whether the transition to plume mode has in fact occurred.

4.5 Results with Xenon Propellant

Xenon is much more commonly employed than argon in operational electric thrusters. A limited quantity of xenon was available, and both the Langmuir and emissive probes were operated to determine what differences in cathode performance this change in propellant causes. Again, two operating conditions were considered, one at a nominal flow rate, and another at a low flow rate. Similar to the experiments run with argon, the low flow-rate case represented approximately 10% of the nominal flow rate.

As with the argon data, the applicability of the thin-sheath and OML methods was evaluated for the cathode running on xenon. Table 5 and Table 6 show the results calculated with each probe theory for the two different operating conditions.

Table 5: Debye Length and Mean Free Path Calculated Using Thin-Sheath Theory (xenon)

Case	n_e (m^{-3})	T_e (eV)	$\lambda_D(m)$	r_p / λ_D	λ_{ei} / d_p	λ_{en} / d_p
Nominal Flow	1.69×10^{18}	7.95	1.61×10^{-5}	2.37	1.09×10^{4}	1.88×10^{4}
Low Flow	2.71×10^{18}	3.05	7.89×10^{-6}	4.84	1.15×10^{3}	1.17×10^{4}

For the thin-sheath theory, the collisionality assumption is satisfied, but the Debye length is still too large to meet the second criterion. Consequently, the thin-sheath theory will not apply to the xenon plasma either.

Table 6: Debye Length and Mean Free Path Calculated Using OML Theory (xenon)

Case	n_e (m^{-3})	T_e (eV)	$\lambda_D(m)$	r_p / λ_D	λ_{ei} / d_p	λ_{en} / d_p
Nominal Flow	5.79×10^{17}	n/a	2.76×10^{-5}	1.38	3.04×10^{4}	5.49×10^{4}
Low Flow	5.84×10^{17}	n/a	1.70×10^{-5}	2.24	4.99×10^{3}	5.45×10^{4}

With the OML theory, both the collisionality and sheath thickness criteria are met, and OML will also be applicable to the xenon plasma, as it was for the argon plasma.

The cathode is easier to start when running on xenon than on argon. The total heating time required before initiation of the plasma discharge is less. It is also capable of running at lower absolute flow rates. Furthermore, there is also less variation in the discharge current. Reducing the flow rate by 90% changed the discharge current by only 5%. A plot of the electron energy distribution function for the nominal flow rate case, measured as a function of radial position, is presented in Figure 60.

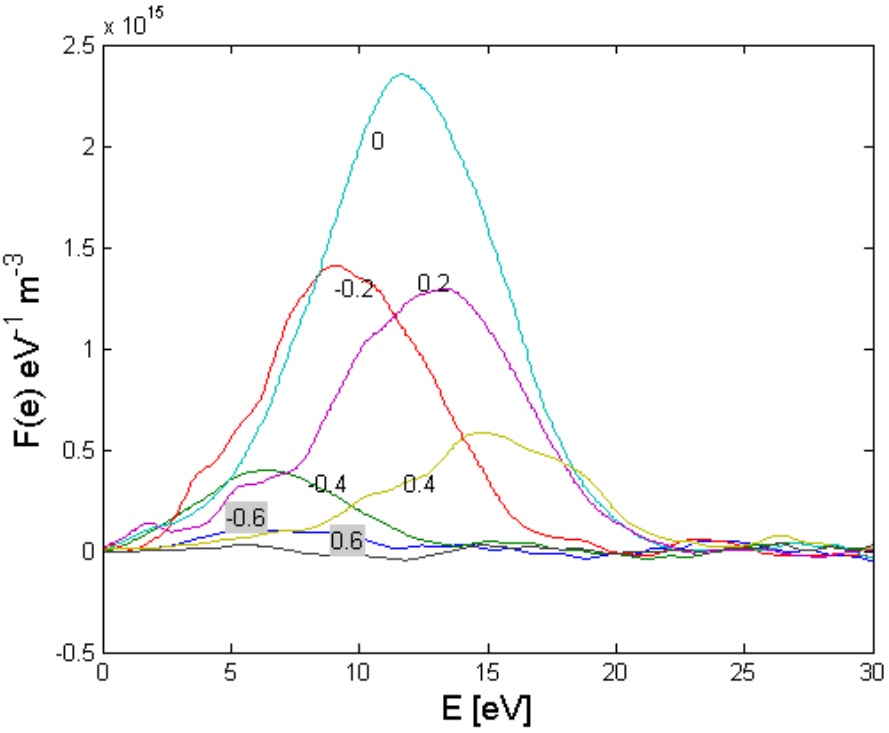

Figure 60: Radial Variation of Electron Energy Distribution Function (Xe Nominal Case)

Compared to the EEDFs obtained for the cathode running on argon, the main peak in these distribution functions is shifted significantly toward higher energies. There is also an apparent asymmetry. At 0.2 cm radial offset from the centerline in each direction, the peaks are

located at very different energies. This behavior was present in multiple runs at the nominal flow rate and at flow rates near the nominal case.

At the reduced flow rate, electron energy distribution functions were measured and are displayed in Figure 61.

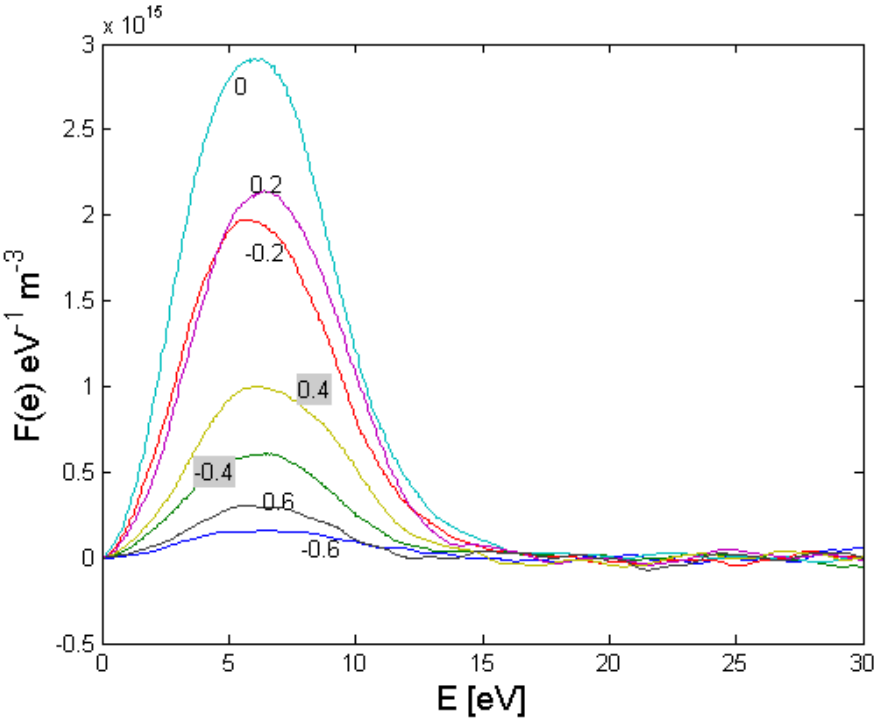

Figure 61: Radial Variation of Electron Energy Distribution Function (Xe Low-Flow Case)

The asymmetry that was apparent at the nominal flow rate has disappeared here, and the peaks have shifted back toward lower energies, more comparable to those calculated for argon.

Examining the plasma potential variation in Figure 62 and Figure 63, the potential is significantly higher at the nominal flow rate, ranging between 22 V and 28 V. At the reduced flow rate, the range is lower, between 16 V and 20 V. There is also a clearer trend in the low-flow case—the plasma potential decreases substantially as the centerline is approached. This trend is not as easy to discern at the higher flow rate. The reduced flow rate more closely resembles the operation of the cathode on argon.

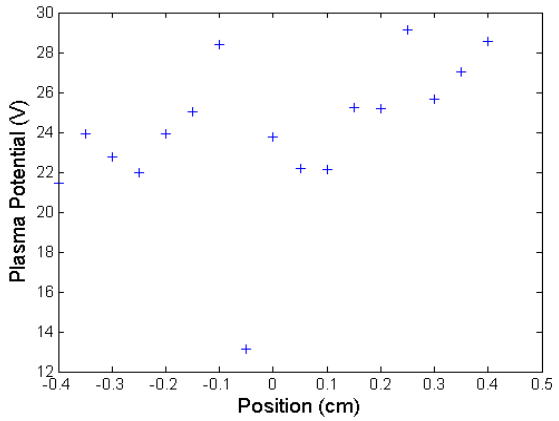

Figure 62: Plasma Potential vs. Radial Position (Xe Nominal Flow Case)

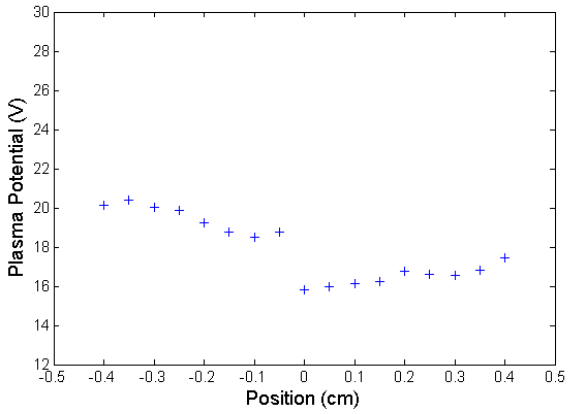

Figure 63: Plasma Potential vs. Radial Position (Xe Low-Flow Case)

As with the argon plasma, the electron temperature was calculated both by integration of the energy distribution function and by finding the slope of the exponential region of the I-V characteristic. Figures 64, 65, 66, and 67 show these calculated temperatures as functions of radial position for both operating conditions.

At the nominal operating condition, the electron temperatures are significantly higher than those measured for argon, primarily in the range of 5 eV to 10 eV. The electron temperature also increases as the probe is moved in one direction across the orifice of the cathode. This was expected, as the peak of the electron energy distribution function is also shifted to higher energies on one side of the cathode orifice. Both the EEDF and slope methods display this trend. At the lower flow rates, the measured electron temperatures are similar to those measured while the cathode was operating on argon. Their magnitudes are generally under 5 eV, and there is no asymmetry observed for this operating condition. The temperatures calculated with the slope method for the low flow-rate case show a temperature minimum when the probe is aligned with the cathode orifice. The temperature increases with radial distance from the orifice.

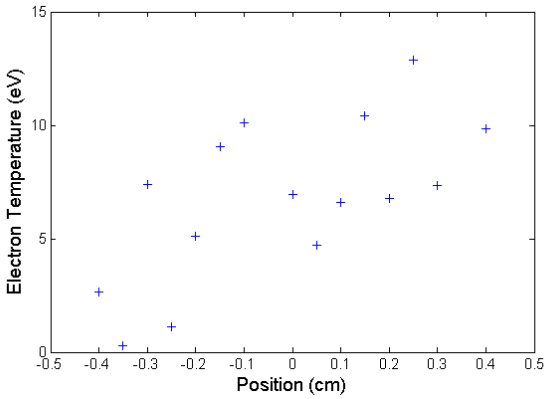

Figure 64: Electron Temperature vs. Radial Position (EEDF Method for Xe Nominal Flow Rate)

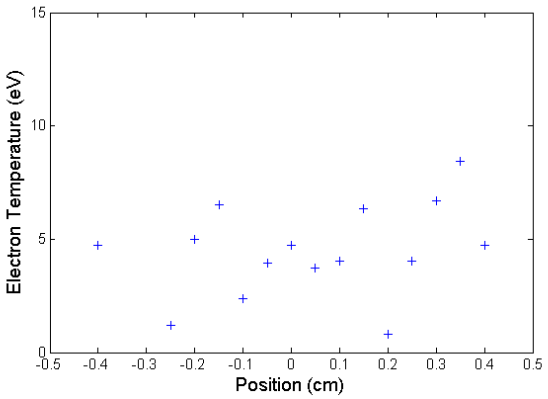

Figure 65: Electron Temperature vs. Radial Position (EEDF Method for Xe Low Flow Rate

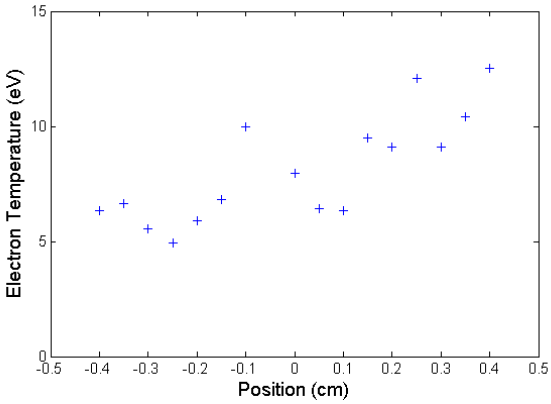

Figure 66: Electron Temperature vs. Radial Position (Slope Method for Xe Nominal Flow Rate)

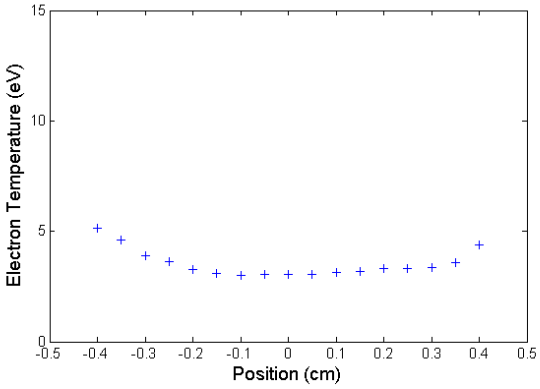

Figure 67: Electron Temperature vs. Radial Position (Slope Method for Xe Low Flow Rate)

Finally, the plasma densities were also calculated, again by integration of the electron energy distribution function and by OML theory. Results from these calculations are shown in Figures 68, 69, 70, and 71.

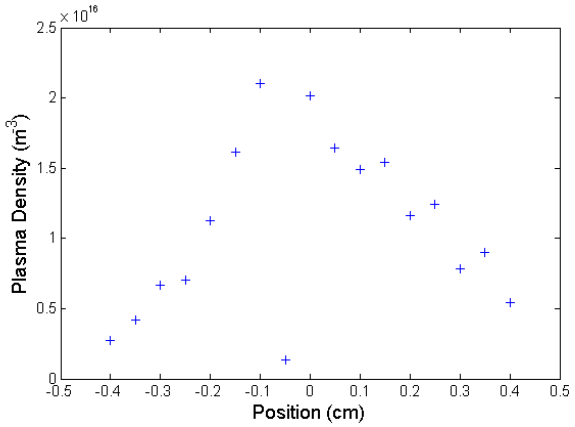

Figure 68: Plasma Density vs. Radial Position (EEDF Method for Xe Nominal Flow Case)

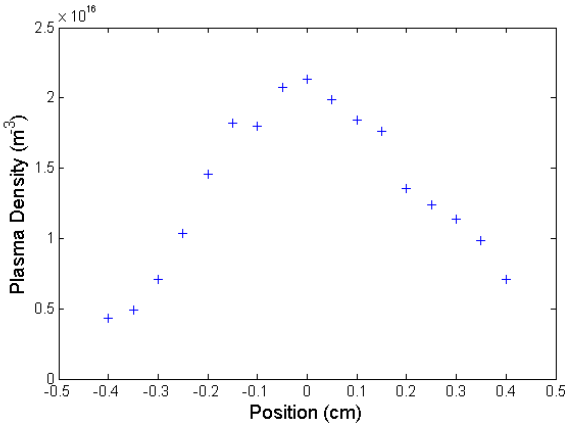

Figure 69: Plasma Density vs. Radial Position (EEDF Method for Xe Low Flow Case)

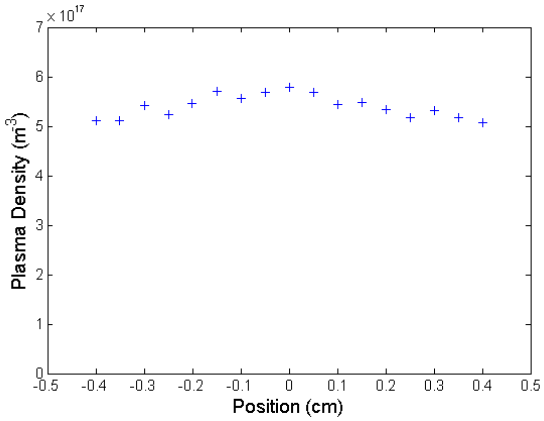

Figure 70: Plasma Density vs. Radial Position (OML Method for Xe Nominal Flow Case)

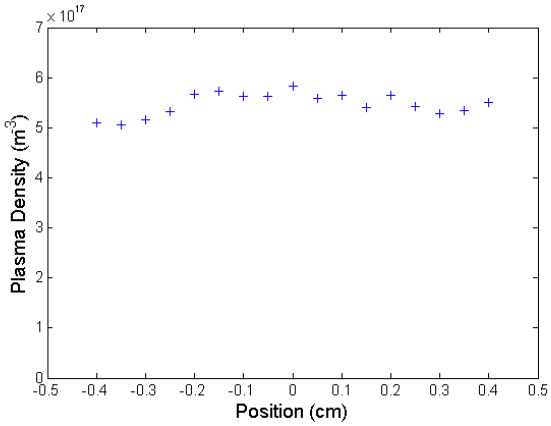

Figure 71: Plasma Density vs. Radial Position (OML Method for Xe Low Flow Case)

Unlike the density data collected for argon, the two estimation methods do not agree. OML theory predicts a plasma density a full order of magnitude higher than that obtained from the EEDF. Furthermore, the OML results do not display the characteristic parabolic shape that is seen in the EEDF calculation. Despite this contradiction, some observations can still be made. As with the data measured in the argon plasma, the propellant flow rate appears to have a negligible effect on the plasma density. Both data sets confirm this. Furthermore, the location of maximum density again appears to be directly in front of the orifice, which is consistent with physical intuition.

The emissive probe was again used to investigate the presence or absence of oscillations in the plasma potential. Data were collected at the nominal and low flow-rate conditions. The heater current for strong emission was again established by observing the asymptotic behavior of the floating potential as the heater current was increased. A plot showing this behavior appears in Figure 72.

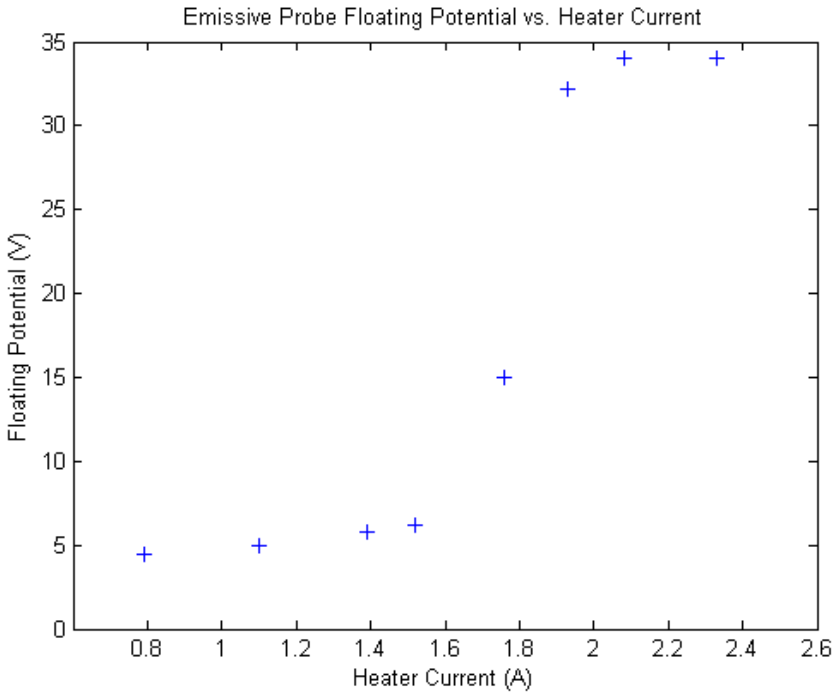

Figure 72: Emissive Probe Floating Potential vs. Heater Current (Xenon)

Once the emissive probe was established in the strongly emitting mode, data were collected for several different flow rates. Time histories and power spectral densities for the nominal and low-flow cases are presented in the figures below.

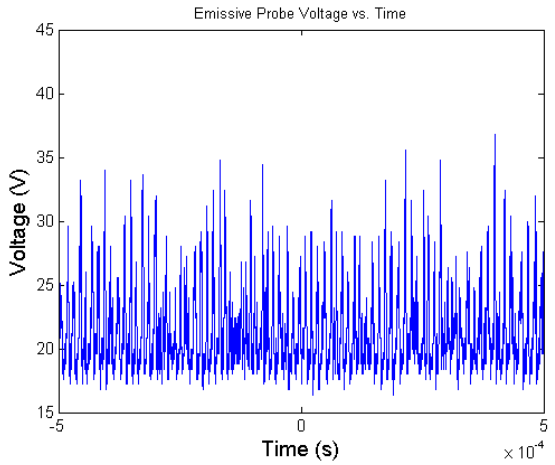

Figure 73: Plasma Potential vs. Time (Xe Nominal Flow Case)

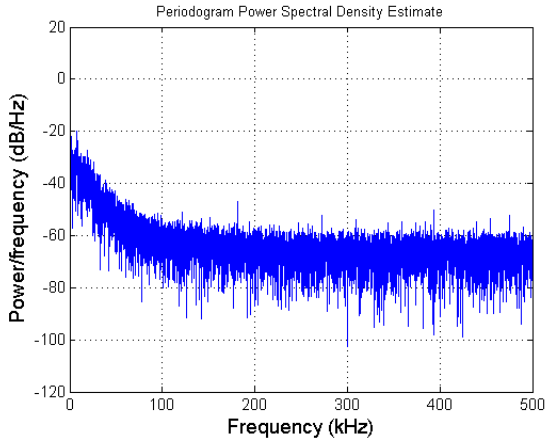

Figure 74: Power Spectral Density Estimate for Plasma Potential (Xe Nominal Flow Case)

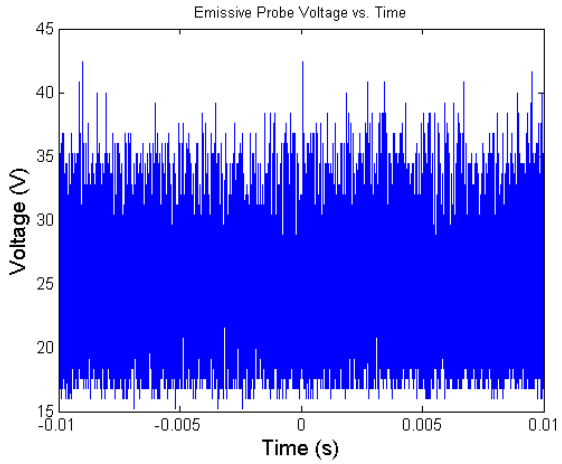

Figure 75: Plasma Potential vs. Time (Xe Low-Flow Case)

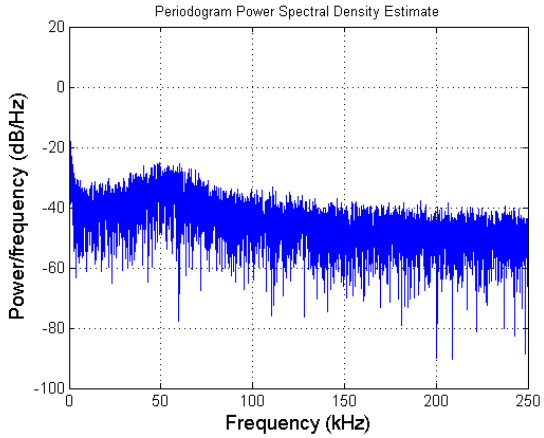

Figure 76: Power Spectral Density Estimate for Plasma Potential (Xe Low-Flow Case)

Under the nominal operating conditions, the maximum peak-to-peak voltage was approximately 20.4 V, and the power spectral density estimate does not show any interesting features. At the lower flow rate, however, the peak-to-peak voltage was 27.2 V. This increase in peak-to-peak voltage was much less for xenon than for argon. The primary feature in the frequency spectrum is a peak at approximately 50-60 kHz, which is also less than that observed for argon. In practice, the cathode appeared to run more reliably and more quiescently on xenon than it did when using argon.

Finally, the behavior of the maximum peak-to-peak voltage as a function of the flow rate was investigated. The peak-to-peak voltage at several different flow rates was recorded and plotted against the normalized flow rate. This figure appears in .

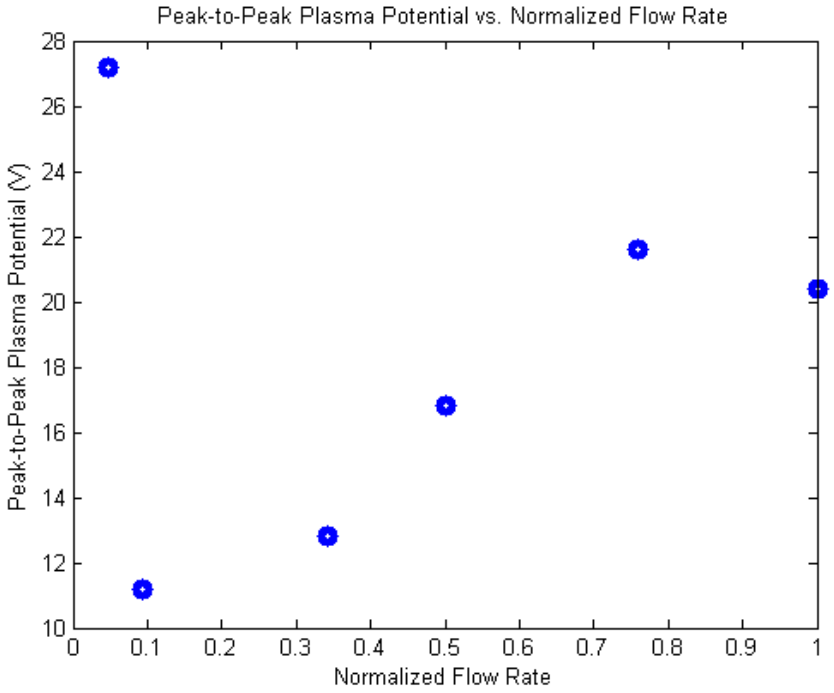

Figure 77: Peak-to-Peak Plasma Potential vs. Flow Rate (Xenon)

Compared to the same data set for argon, a trend is much less apparent here. There is wide variation in the peak-to-peak voltage at higher flow rates. In general, the peak-to-peak voltage tends to decrease with the flow rate until very low rates are reached. Then there is an abrupt transition to a peak-to-peak voltage well above any others measured. As with the data presented for argon, this transition may mark the entrance to plume mode, although this cannot be asserted with certainty.

5 Conclusions and Recommendations for Future Work

The performance of the cathode was analyzed when running on both argon and xenon. Two instruments, a Langmuir probe and an emissive probe, and several different probe analysis techniques were applied in order to extract information about the plasma potential, the electron temperature, the plasma density, and the electron energy distribution function. The emissive probe was also used in order to collect temporally resolved data for the plasma potential. This was done to search for transient effects during low flow-rate operation of the cathode.

Results indicate that there are few significant changes associated with the electron temperature and plasma density with decreasing propellant flow rate. The density was essentially unchanged given the accuracy limitations of the probe theory applied. The electron temperature typically reached a minimum value on the cathode centerline and otherwise was flat until the very edges of the plume were reached.

The electron energy distribution function displayed a shift in its peak toward higher energies both with decreasing flow rate and with increasing radial distance. With xenon, asymmetries were observed in the EEDF during operation at the higher flow rates that were not evident at low flow-rate operation.

Among the most important changes observed as the flow rate was decreased was a large increase in the maximum peak-to-peak plasma potential recorded with the emissive probe. This parameter nearly doubled between the two operating conditions for the argon plasma, and oscillations were observed at approximately 150 kHz. This effect was less pronounced for the xenon plasma, but oscillations were observed at 50-60 kHz when running at low flow rates that were not present when the cathode was operated at higher flow rates. When the radial variation of the plasma potential was measured, the minimum value was located on the centerline of the

cathode. However, there was also an abrupt increase in the plasma potential near this position. This occurred when the cathode was operating on argon as well as xenon and for both flow rates that were considered.

Because the positioning system used to move the Langmuir probe in the radial direction lacks the required precision, spatial averaging of many distribution functions or I-V traces was impossible. This led to the presence of significant noise in the high-energy tail of the distribution functions. The presence of this noise can significantly affect the utility of the calculated energy distribution function. Certainly the integration of these functions to calculate the plasma density and electron temperature will suffer from increased uncertainty. The electron temperature calculation is more seriously affected as it involves both the integration of the energy distribution function and division by the density, also calculated from the distribution function. It is likely that this combination of uncertainties results in the large scatter seen in the electron temperature measurements made by integrating the EEDF.

In addition to creating additional uncertainty with the plasma density and electron temperature measurements made using the EEDF, the presence of noise in the tail made computations of the ionization instability frequency impossible. This frequency is given by equation (86) and relies on the calculation of the ionization rate coefficient. This coefficient is averaged over the energy distribution function for all energies greater than the first ionization energy for the propellant under consideration. For argon, where the first ionization energy is 15.77 eV, and xenon, where the first ionization energy is 12.13 eV, this means that nearly the entire integration is performed in a region with significant noise. Consequently, this experiment was unable to confirm independently the frequency of plasma potential oscillations observed by the emissive probe.

$$f \approx \frac{n_e < \sigma v_e >}{\left(n_i / n_0\right)} \qquad (86)$$

Experimentally, these results represent the product of many improvements made to the instrumentation and other hardware over previous efforts. Among the most important was the addition of a high-speed power supply system for the Langmuir probe. Previous work was conducted using a sourcemeter to provide the voltage sweeps and to record the current [10]. This setup was limiting in that the sourcemeter was unable to sweep the voltage as quickly as desired; consequently, the spatial resolution of the probe measurements was significantly reduced. Furthermore, the need for the sourcemeter to stop sweeping periodically in order to transfer the contents of its memory to the computer would result in the loss of portions of the probe characteristic during critical periods of the probe's motion. This effect, combined with the hysteresis of the positioning system, meant that many passes at the same cathode operating conditions were necessary in order to ensure full coverage of the radial envelope being investigated.

For this experiment, the sourcemeter was substituted by a bipolar operational amplifier power supply driven by a function generator. This allows many and higher sweep rates to be selected. Data were also recorded continuously by the computer's data acquisition card, eliminating any chance of losing portions of the I-V characteristic.

The most significant problem associated with the experimental hardware remains the positioning system. The mechanical "backlash" present in this system makes it very difficult to achieve verifiable, spatial repeatability from test to test and to average many probe traces to reduce the noise present in the calculated EEDFs. The experimental results would be improved significantly by the addition of true and reliable position feedback. The speed of the positioning system is also problematic. This limits the ability of the Langmuir probe to be placed close to the

cathode orifice. During operation on xenon, the cathode discharge current had to be reduced to a level that would not cause the Langmuir probe to reach temperatures sufficient to cause thermionic emission. The ability of the probe to move more quickly through the densest and most energetic areas of the plume would allow measurements to be made much closer to the cathode orifice.

The flow control system for this apparatus is also rudimentary and hinders the repeatability of the experiment. There is no automatic control over the propellant feed system. All adjustments to the flow rate are made manually through the actuation of a needle valve. This can cause significant drift during the course of a given experiment and is also difficult to adjust precisely to a desired flow rate. The addition of an active flow controller would enable a flow rate to be selected and maintained more reliably throughout the duration of a test.

The type of anode used in these experiments may affect the results as well. Most studies of hollow cathodes use either a planar or conical anode to produce the plume plasma. The cylindrical anode used here makes it difficult to compare these measurements to those collected in other studies. The alignment of the anode was not precise, and it is also possible that some of the asymmetries seen in the data are a result of a physical asymmetry in the alignment of the anode and cathode. Future work should consider the use of a more traditional anode geometry to improve the ability of these results to be interpreted in the context of other research.

Processing of these data sets also introduces some uncertainty into the measurements. The technique chosen for the computation of the electron energy distribution function requires numerical differentiation of the probe characteristic, a procedure inherently amplifies the noise present in the probe signal. In order to obtain usable results, the signal must be smoothed at many points during the processing procedure. This introduces some risk of obscuring important

features that are desirable to preserve. The amount of smoothing was selected in order to minimize this possibility, but it cannot be entirely eliminated.

Calculation of the electron energy distribution function also requires knowledge of the plasma potential. This is difficult to determine from the I-V characteristics obtained from this cathode. Cylindrical probes have an inherent tendency to lack a well-defined knee in the transition to the electron saturation region. In addition, the plasma studied here does not reach electron saturation at the probe sweep range used in this experiment. Because the cathode is fundamentally an electron source, it is unlikely that electron saturation could be achieved with a practical probe sweep bias potential. This gives some uncertainty in the calculation of the plasma potential, which directly affects the EEDF. A possible independent technique to verify the plasma potential using the emissive probe floating voltage was unable to be applied to the Langmuir probe data due to the fixed location of the emissive probe. Future studies involving this experimental hardware may find it beneficial to translate the emissive probe with the Langmuir probe so that collocated measurements could be made.

Of the three analysis techniques considered for this experiment, neither thin-sheath theory nor OML theory were entirely satisfactory in characterizing the plasma environment. Only the Druyvesteyn method to obtain the electron energy distribution function and subsequent integration of the EEDF was able to determine all of the required plasma parameters. Thin-sheath theory was entirely inapplicable due to the sheath thickness, and OML theory was only useful for determination of the plasma density due to the lack of an electron saturation region of the probe trace.

6 References

[1] Goebel, D.M. and Katz, I. *Fundamentals of Electric Propulsion*. JPL Space Science and Technology Series; 2008.

[2] Sutton, G.P. and Biblarz, O. *Rocket Propulsion Elements.* New York: Wiley; 2001.

[3] Sengupta, A., Brophy, J.R., and Goodfellow, K.D. Status of the Extended Life Test of the Deep 1 Flight Spare Ion Engine After 30,352 Hours of Operation. 2003. AIAA Paper 2003-4558.

[4] Mikellides, I.G. and Katz, I. Wear Mechanisms in Electron Sources for Ion Propulsion, 1: Neutralizer Hollow Cathode. *Journal of Propulsion and Power*. [Online] 2008;24(4): pp. 855-865. Available from : doi: 10.2514/1.33461.

[5] Goebel, D.M., Jameson, K.K., Katz, I., and Mikellides, I.G. Potential Fluctuations and Energetic Ion Production in Hollow Cathode Discharges. *Physics of Plasmas.* [Online] 2007;14. Available from: doi: 10.1063/1.2784460.

[6] Boeuf, J.P. and Garrigues, L. Low Frequency Oscillations in a Stationary Plasma Thruster. *Journal of Applied Physics*. [Online] 1998;84(7): pp. 3541-3554.

[7] Katz, I., Mikellides, I.G., Goebel, D.M., Jameson, K.K., Wirz, R., and Polk, J.E. Production of High Energy Ions Near an Ion Thruster Discharge Hollow Cathode. In: 42nd AIAA/ASME/SAE/ASEE Joint Propulsion Conference, 2006, Sacramento, CA. AIAA Paper 2006-4485.

[8] Herman, D.A. and Gallimore, A.D. Discharge Cathode Electron Energy Distribution Functions in a 40-cm NEXT-type Ion Engine. In: 41st AIAA/ASME/SAE/ASEE Joint Propulsion Conference, 2005, Tucson, AZ. AIAA Paper 2005-4252.

[9] Sawlani, K.U. and Foster, J.E. Comparison of Various Numerical Schemes to Obtain EEDF with High Accuracy. In: 31st International Electric Propulsion Conference, 2009, Ann Arbor, MI. IEPC Paper 2009-043.

[10] Behlman, N.J. *Electron Energy Distribution Measurements in the Plume Region of a Low-Current Hollow Cathode.* Master's Thesis. Worcester Polytechnic Institute; 2009.

[11] Piel, A. *Plasma Physics*. Heidelberg: Springer; 2010.

[12] Vincenti, W.G., and Kruger, C.H. *Introduction to Physical Gas Dynamics*. Krieger; 1965.

[13] Bittencourt, J.A. *Fundamentals of Plasma Physics*. New York: Pergamon Press; 1986.

[14] Hastings, D. and Garrett, H. *Spacecraft-Environment Interactions*. Cambridge: Cambridge University Press; 1996.

[15] Li, M., Dew, S.K., and Brett, M.J. Effects of Electron Distribution Functions on the Floating Potential of Particles in the Plasma: Thin Plasma Sheaths. *Journal of Physics D: Applied Physics.* [Online] 1999;32: pp. 2056-2059.

[16] Raizer, Y.P. *Gas Discharge Physics*. Berlin: Springer-Verlag; 1991.

[17] Lipschultz, B., Hutchinson, I., LaBombard, B., and Wan, A. Electric Probes in Plasmas. *Journal of Vacuum Science and Technology A: Vacuum, Surfaces, and Films*. [Online] 1986;4(3): pp. 1810-1816. Available from: doi: 10.1116/1.573945.

[18] Chen, F. *Langmuir Probe Diagnostics.* Mini-Course on Plasma Diagnostics, IEEE-ICOPS Meeting, Jeju, Korea. 2003.

[19] Hershkowitz, N. How Langmuir Probes Work. *Plasma Diagnostics*. 1989.

[20] Chen, F. Electric Probes. In: Huddlestone, R.H., Leonard, S.L (eds.) *Plasma Diagnostic Techniques*. Academic Press; 1965. pp. 113-200.

[21] Allen, J.E. Probe Theory—The Orbital Motion Approach. *Physica Scripta*. [Online] 1991;45: pp. 497-503.

[22] Hester, S.D. and Sonin, A.A. Ion Temperature Sensitive End Effect in Cylindrical Langmuir Probe Response at Ionosphere Satellite Conditions. *The Physics of Fluids*. 1970;13(5): pp. 1265-1274.

[23] Tilley, D.L., Kelly, A.J., and Jahn, R.G. The Application of the Triple Probe Method to MPD Thruster Plumes. In: 21st International Electric Propulsion Conference, 1990, Orlando, FL. AIAA Paper 90-2667.

[24] Druyvesteyn, M.J. Der Niedervoltbogen. *Zeitschrift für Physik*. 1930: pp. 781-797.

[25] Lieberman, M.A. and Lichtenberg, A.J. *Principles of Plasma Discharges and Materials Processing*. Hoboken: Wiley; 2005.

[26] Hershkowitz, N. and Cho, M.H. Measurement of plasma potential using collecting and emitting probes." *Journal of Vacuum Science and Technology*. 1988;6: pp. 2054-2059.

[27] Kemp, R.F. and Sellen, J.M. Plasma Potential Measurements by Electron Emissive Probes. *Review of Scientific Instruments*. 1966;37: pp. 455-461.

[28] Yao, W.E., Intrator, T., and Hershkowitz, N. Direct indication technique of plasma potential with differential emissive probe. *Review of Scientific Instruments*. 1985;56: pp. 519-524.

[29] Hobbs, G.D. and Wesson, J.A. Heat Flow through a Langmuir Sheath in Presence of Electron Emission. *Plasma Physics*. 1967;9.

[30] Schuss, J.J. and Parker, R.R. Behavior of electron-emitting plasma probes in the space-charge-limited regime. *Journal of Applied Physics*. 1974;45: pp. 4778-4783.

[31] Hershkowitz, N, Nelson, B., Pew, J., and Gates, D. Self-emissive probes. *Review of Scientific Instruments*., 1983;54: pp. 29-34.

[32] Smith, J.R., Hershkowitz, N., and Coakley, P. Inflection-point method of interpreting emissive probe characteristics. *Review of Scientific Instruments*. 1979;50: pp. 210-218.

[33] Makowski, M.A. and Emmert, G.A. New method to measure plasma potential with emissive probes. *Review of Scientific Instruments*. 1983;54: pp. 830-836.

[34] Busek, Co., Inc. *Hall Effect Thruster Systems.* [Online]. Available from: http://www.busek.com/halleffect.html

[35] Fossum, E.C., Sommerville, J.D., and King, L.B. Characterization of Near Field Plasma Environment of a Hollow Cathode Assembly. In: 40th AIAA/ASME/SAE/ASEE Joint Propulsion Conference, 2004, Fort Lauderdale, FL.

[36] Goebel, D.M. (dan.m.goebel@jpl.nasa.gov) *Emissive Probe Circuit*. Email to: Blandino, J. (blandino@wpi.edu) 8 October 2009.

[37] The Mathworks, Inc. *Butterworth filter design*. [Online]. Available from: http://www.mathworks.com/help/toolbox/signal/butter.html

[38] The Mathworks, Inc. *Smooth Response Data*. [Online]. Available from: http://www.mathworks.com/help/toolbox/curvefit/smooth.html

[39] Linnell, J.A. and Gallimore, A.D. Internal Langmuir Probe Mapping of a Hall Thruster with Xenon and Krypton Propellant. In: 42nd AIAA/ASME/SAE/ASEE Joint Propulsion Conference, 2006, Sacramento, CA. AIAA Paper 2006-4470

[40] Herman, D.A. *The Use of Electrostatic Probes to Characterize the Discharge Plasma Structure and Identify Discharge Cathode Erosion Mechanisms in Ring-Cusp Ion Thrusters.* Ph.D. Dissertation. University of Michigan; 2005.

7 Bibliography

[1] Polk, J.E., Mikellides, I.G., Caprece, A.M., and Katz, I. Barium Depletion in Hollow Cathode Emitters. In: 45th Joint Propulsion Conference, 2009, Denver, CO. AIAA Paper 2009-5197.

[2] Jameson, K.K., Goebel, D.M., Hofer, R.R., and Watkins, R.M. Cathode Coupling in Hall Thrusters. In: 30th International Electric Propulsion Conference, 2007, Florence. IEPC Paper 2007-278.

[3] Kolasinski, R.D. and Polk, J.E. Characterization of Cathode Keeper Wear by Surface Layer Activation. In: 39th AIAA/ASME/SAE/ASEE Joint Propulsion Conference, 2003, Huntsville, AL.

[4] Polk, J.E., Goebel, D.M., Watkins, R., Jameson, K., Yoneshige, L., Pryzbylowski, J., and Cho, L. Characterization of Hollow Cathode Performance and Thermal Behavior. In: 42nd AIAA/ASME/SAE/ASEE Joint Propulsion Conference, 2006, Sacramento, CA. AIAA Paper 2006-5150.

[5] Katz, I., Polk, J.E., Mikellides, I.G., Goebel, D.M., and Hornbeck, S.E. Combined Plasma and Thermal Hollow Cathode Insert Model. In: 29th International Electric Propulsion Conference, 2005, Princeton, NJ. IEPC Paper 2005-228.

[6] Goebel, D.M. and Watkins, R.M. Compact Lanthanum Hexaboride Hollow Cathode. *Review of Scientific Instruments*. 2010;81. Available from: doi: 10.1063/1.3474921.

[7] Hofer, R.R., Johnson, L.K., Goebel, D.M., and Wirz, R.E. Effects of Internally-Mounted Cathodes on Hall Thruster Plume Properties. *IEEE Transactions on Plasma Science*. 2008;36(5): pp. 2004-2014.

[8] Pryzbylowski, J.N., Polk, J.E., Shepherd, J.E., and Caprece, A.E. Effects of Varied Propellant Compositions on the Ion Energy Distributions in Hollow Cathodes. In: 30th International Electric Propulsion Conference, 2007, Florence. IEPC Paper 2007-174.

[9] Mikellides, I.G., Katz, I., Goebel, D.M., and Jameson, K.K. Evidence of Nonclassical Plasma Transport in Hollow Cathodes for Electric Propulsion. *Journal of Applied Physics*. 2007;101(6). Available from: doi: 10.1063/1.2710763.

[10] Goebel, D.M., Katz, I., Polk, J., Mikellides, I.G., Jameson, K.K., and Liu, T. Extending Hollow Cathode Life for Electric Propulsion in Long-Term Missions. In: Space 2004 Conference, 2004, Phoenix, AZ. AIAA Paper 2004-5911.

[11] Goebel, D.M. and Watkins, R.M. High Current Hollow Cathodes for High Power Ion and Hall Thrusters. In: 41st AIAA/ASME/SAE/ASEE Joint Propulsion Conference, 2005, Tucson, AZ. AIAA Paper 2005-4239.

[12] Jameson, K.K., Goebel, D.M., and Watkins, R.M. Hollow Cathode and Thruster Discharge Chamber Plasma Measurements Using High-Speed Scanning Probes. In: 29th International Electric Propulsion Conference, 2005, Princeton, NJ. IEPC Paper 2005-269.

[13] Tighe, W.G., Chien, K., Goebel, D.M., and Longo, R.T. Hollow Cathode Emission and Ignition Studies at L-3 ETI. In: 30th International Electric Propulsion Conference, 2007, Florence. IEPC Paper 2007-023.

[14] Tighe, W.G., Chien, K., Goebel, D.M., and Longo, R.T. Hollow Cathode Ignition Studies and Model Development. In: 29th International Electric Propulsion Conference, 2005, Princeton, NJ. IEPC Paper 2005-314.

[15] Goebel, D.M., Jameson, K.K., Watkins, R.M., Katz, I., and Mikellides, I.G. Hollow Cathode Theory and Experiment. I. Plasma Characterization Using Fast Miniature scanning Probes. *Journal of Applied Physics*. 2005;98(11). Available from: doi: 10.1063/1.2135417.

[16] Mikellides, I.G., Katz, I., Goebel, D.M., and Polk, J.E. Hollow Cathode Theory and Experiment. II. A Two-Dimensional Theoretical Model of the Emitter Region. *Journal of Applied Physics*. 2005;98(11). Available from: doi: 10.1063/1.2135409.

[17] Katz, I., Mikellides, I.G., Goebel, D.M., and Polk, J.E. Insert Heating and Ignition in Insert-Gas Hollow Cathodes. *IEEE Transactions on Plasma Science*. 2008;36(5): pp. 2199-2206.

[18] Goebel, D.M., Watkins, R.M., and Jameson, K.K. LaB_6 Hollow Cathodes for Ion and Hall Thrusters. *Journal of Propulsion and Power*. 2007;23(3): pp. 552-558. Available from: doi: 10.2514/1.25475.

[19] Jameson, K.K., Goebel, D.M., Mikellides, I., and Watkins, R.M. Local Neutral Density and Plasma Parameter Measurements in a Hollow Cathode Plume. In: 42nd AIAA/ASME/SAE/ASEE Joint Propulsion Conference, 2006, Sacramento, CA. AIAA Paper 2006-4490.

[20] Mikellides, I.G., Katz, I., Goebel, D.M., and Polk, J.E. Model of a Hollow Cathode Insert Plasma. In: 40th AIAA/ASME/SAE/ASEE Joint Propulsion Conference, 2004, Pasadena, CA. AIAA Paper 2004-3817.

[21] Katz, I., Anderson, J.R., Polk, J.E., and Goebel, D.M. Model of Hollow Cathode Operation and Life Limiting Mechanisms. In: 28th International Electric Propulsion Conference, 2003, Toulouse. IEPC Paper 2003-0243.

[22] Katz, I., Mikellides, I.G., and Goebel, D.M. Model of the Plasma Potential Distribution in the Plume of a Hollow Cathode. In: 40th AIAA/ASME/SAE/ASEE Joint Propulsion Conference, 2004, Pasadena, CA. AIAA Paper 2004-4108.

[23] Mikellides, I.G., Goebel, D.M., Snyder, J.S., Katz, I., and Herman, D.A. Neutralizer Hollow Cathode Simulations and Validation with Experiments. In: 45th AIAA/ASME/SAE/ASEE Joint Propulsion Conference, 2009, Denver, CO. AIAA Paper 2009-5196.

[24] Mikellides, I.G., Snyder, J.S., Goebel, D.M., Katz, I., and Herman, D.A. Neutralizer Hollow Cathode Simulations and Comparisons with Ground Test Data. In: 31st International Electric Propulsion Conference, 2009, Ann Arbor, MI. IEPC Paper 2009-20.

[25] Mikellides, I.G., Katz, I., and Goebel, D.M. Numerical Simulation of the Hollow Cathode Discharge Plasma Dynamics. In: 29th International Electric Propulsion Conference, 2005, Princeton, NJ. IEPC Paper 2005-200.

[26] Mikellides, I.G., Katz, I., Jameson, K.K., and Goebel, D.M. Numerical Simulations of a Hall Thruster Hollow Cathode Plasma. In: 30th International Electric Propulsion Conference, 2007, Florence. IEPC Paper 2007-018.

[27] Katz, I., Anderson, J.R., Goebel, D.M., Wirz, R., and Sengupta, A. Plasma Generation Near an Ion Thruster Discharge Chamber Hollow Cathode. In: 39th AIAA/ASME/SAE/ASEE Joint Propulsion Conference, 2003, Huntsville, AL. AIAA Paper 2003-5161.

[28] Katz, I., Mikellides, I.G., Goebel, D.M., and Polk, J.E. Plasma Heating of Inert Gas Hollow Cathode Inserts. In: 30th International Electric Propulsion Conference, 2007, Florence. IEPC Paper 2007-017.

[29] Goebel, D.M., Jameson, K.K., Katz, I., and Mikellides, I.G. Plasma Potential Behavior and Plume Mode Transitions in Hollow Cathode Discharges. In: 30th International Electric Propulsion Conference, 2007, Florence. IEPC Paper 2007-277.

[30] Katz, I., Mikellides, I.G., Goebel, D.M., Jameson, K.K., Wirz, R., and Polk, J.E. Production of High Energy Ions Near an Ion Thruster Discharge Hollow Cathode. In: 42nd AIAA/ASME/SAE/ASEE Joint Propulsion Conference, 2006, Sacramento, CA. AIAA Paper 2006-4485.

[31] Mikellides, I.G., Katz, I., Goebel, D.M., and Polk, J.E. Theoretical Model of a Hollow Cathode Plasma for the Assessment of Insert and Keeper Lifetimes. In: 41st AIAA/ASME/SAE/ASEE Joint Propulsion Conference, 2005, Tucson, AZ. AIAA Paper 2005-4234.

[32] Katz, I., Mikellides, I.G., Polk, J.E., Goebel, D.M., and Hornbeck, S.E. Thermal Model of the Hollow Cathode Using Numerically Simulated Plasma Fluxes. *Journal of Propulsion and Power*. 2007;23(3): pp. 522-527. Available from: doi: 10.2514/1.21103.

[33] Polk, J.E., Mikellides, I.G., Katz, I., and Capece, A.M. Tungsten and Barium Transport in the Internal Plasma of Hollow Cathodes. *Journal of Applied Physics*. 2009;105(11). Available from: doi: 10.1063/1.3111970.

[34] Polk, J.E., Goebel, D.M., and Tighe, W. XIPS 25-cm Thruster Cathode Life Qualification for Use on Deep Space Missions. In: 30th International Electric Propulsion Conference, 2007, Florence. IEPC Paper 2007-193.

Appendix A MATLAB Programs

Langmuir Probe Data Analysis

```
%Read Data

clc
clear all

filename='030911_079_666_4.csv';
data=load([filename]);

%Time is stored in the first column, voltage in the second, and current in
%the third. Voltage and current and corrected based on the 10:1 voltage
%divider, and the INA146's gain of 10, respectively. The position is
%calculated using the speed of the probe travel (0.12 cm/s)
time=data(:,1);
voltage=10*data(:,2);
current=-0.001*data(:,3);
position=0.118872*time;

%Define a butterworth filter (ninth order low-pass)
[z,p,k]=butter(9,0.07,'low');
[sos,g]=zp2sos(z,p,k);
Hd=dfilt.df2tsos(sos,g);

%Filter current
currentf=filter(Hd,current);



%Find Center Using Maximum Current
[maxi,index]=max(currentf);
minv=min(voltage);

i=index;
centerp=position(index);

%Extract the trace that was recorded in the center position
while voltage(i)>-40
    i=i-1;
end

centerv=zeros(1,index-i+1);
centeri=zeros(1,index-i+1);
centerif=zeros(1,index-i+1);
k=0;
for j=i:index
    k=k+1;
```

```
    centerv(1,k)=voltage(j);
    centerif(1,k)=currentf(j);
    centeri(1,k)=current(j);
end


%% Introduce Constants, Import Data
e=1.60217646e-19;               %Elementary Charge (Coulombs)
kb=1.3806503e-23;                %Boltzmann Constant (m^2*kg)/(s^2*K)
e_o=8.85418782e-12;             %Permittivity of Freespace (s^4*A^2)/(m^3*kg)
m_e=9.10938188e-31;             %Mass of electron (kg)
m_ar=6.634e-26;                 %Mass of Argon atom (kg)
D_p=.003*.0254;                 %Probe Diameter (m)
L_p=.003;                       %Probe Length (m)

A_p=pi*D_p*L_p+pi*D_p^2/4;      %Probe Area
r_p=D_p/2;                      %Probe Radius

%Split I-V characteristic into individual sweeps
posi=centerp-0.4;   %Initial position
dpos=0.05;          %Step
posf=centerp+0.4;   %Final Position
middle=1;
l=0;
%Define position array and offset so that the center is 0.
positionarray=posi:dpos:posf;
centerparray=ones(1,length(positionarray));
centerparray=centerparray*centerp;
positionarray=positionarray-centerparray;
for pos=posi:dpos:posf
    %Extract individual sweeps
    while position(middle)<pos
        middle=middle+1;
    end

    high=middle;
    low=middle;
    highlimit=40;
    lowlimit=-40;
    if  voltage(middle+10)>voltage(middle)
        while voltage(high)<highlimit
            high=high+1;
        end
        while voltage(low)>lowlimit
            low=low-1;
        end
    else
        while voltage(high)>lowlimit
            high=high+1;
        end

        while voltage(low)<highlimit
            low=low-1;
        end
    end
```

```
    k=0;
    sweepv=zeros(1,high-low+1);
    sweepi=zeros(1,high-low+1);
    for i=low:high
        k=k+1;
        sweepv(1,k)=voltage(i);
        sweepi(1,k)=currentf(i);
    end

    if voltage(middle+10)<voltage(middle)
        sweepv=fliplr(sweepv);
        sweepi=fliplr(sweepi);
    end

%Sweepv and sweepi are the original I-V traces. V and I will be modified
%later during processing
V=sweepv;
I=sweepi;


%calculate dV
dVarray=zeros(length(V)-1);
for i=1:length(V)-1
    dVarray(i)=V(i+1)-V(i);
end

dVarray=mean(dVarray);
dV=dVarray(1);

n=(max(V)-min(V))/dV;

%define domain of interest (not applied until very end)
Vmin=-39;
Vmax=39;

%Guess range for plasma potential
phi_min=10;
phi_max=30;

[~,cut1]=min(abs(V-Vmin));
[~,cut2]=min(abs(V-Vmax));

%% Differentiate I(V)
%Smooth the current
I=smooth(I,120);
Ismooth=I; %Save smoothed curve for later processing methods
Vsmooth=V;

%Take first derivative
for i=2:length(V)-1
   dI(i)=(I(i+1)-I(i-1))/2/dV;
end
```

```
i=1; dI(i)=(-3*I(i)+4*I(i+1)-I(i+2))/2/dV;
i=length(V); dI(i)=(3*I(i)-4*I(i-1)+I(i-2))/2/dV;


%% Differentiate dI(V)/dV
%Smooth the first derivative.
dI=smooth(dI,120);

%Find second derivative
for i=2:length(V)-1
   dI2(i)=(dI(i+1)-dI(i-1))/2/dV;
end

i=1; dI2(i)=(-3*dI(i)+4*dI(i+1)-dI(i+2))/2/dV;
i=length(V); dI2(i)=(3*dI(i)-4*dI(i-1)+dI(i-2))/2/dV;

%Smooth second derivative
dI2=smooth(dI2,50);

    I=I(cut1:cut2);
    dI=dI(cut1:cut2);
    dI2=dI2(cut1:cut2);
    V=V(cut1:cut2);

%% cut off tail of distribution function
[~,cut3]=min(abs(V-phi_min));
[~,cut4]=min(abs(V-phi_max));
%Peak detection algorithm finds the plasma potential by the maximum of the
%first derivative.
    locs = peakdet(dI(cut3:cut4),1e-8);
    cut5=round(min(locs(:,1)))+cut3;


%% Store Plasma Parameters
phi_p_1st=V(cut5); %Plasma Potential from 1st derivative
l=l+1;
phi1starray(l)=phi_p_1st; %Store plasma potential from 1st derivative.
%Calculate Plasma Potential by Curvefit method
[~,cut11]=min(abs(Vsmooth-8));
[~,cut21]=min(abs(Vsmooth-15));
V1=Vsmooth(cut11:cut21);
I1=Ismooth(cut11:cut21);
I1=I1';
coeffp1=polyfit(V1,log(I1),1);
[~,cut31]=min(abs(Vsmooth-25));
[~,cut41]=min(abs(Vsmooth-35));
V2=Vsmooth(cut31:cut41);
I2=Ismooth(cut31:cut41);
I2=I2';
coeffp2=polyfit(V2,log(I2),1);
phi_pcurve=-(coeffp1(2)-coeffp2(2))/(coeffp1(1)-coeffp2(1));
phicurvearray(l)=phi_pcurve;
%Calculate Plasma Potential from Second Derivative
start=min([phi_pcurve phi_p_1st]);
[~,index]=min(abs(V-(start-5)));
```

```
count=0;
dI2save=dI2;
if dI2(index+count)>0
while dI2(index+count)>0
    count=count+1;
end
else
    while dI2(index+count)<0
        count=count+1;
    end
end
phi_p_2nd=V(index+count);
phi2ndarray(l)=phi_p_2nd;
[a,mostprob]=max(dI2);

phi_p=mean([phi_p_1st phi_p_2nd]);

phi_parray(l)=phi_p; %Save overall estimate of plasma potential
%Make cut
[~,cut5]=min(abs(V-phi_p));
dI2(cut5:length(V))=0;
V=phi_p-V;
%Calculate F(e)
F=zeros(1,length(V));
for i=1:length(V)
F(1,i)=4/e^2/A_p*sqrt(m_e*V(i)/2/e)*dI2(i);
end
% Integrate distribution to determine density and electron temp
ne=0; E_avg=0;
for i=1:length(V)
    ne=ne+e*dV*F(i);                    %Number density [m^-3]
    E_avg=E_avg+e*V(i)*e*dV*F(i);       %Avg Energy
end


Eavgarray(l)=E_avg/ne/e;
F=F*e;
f=F/ne;                                 %Normalized Distribution
Te=2/3*E_avg/ne;                         %Te [Joules]
Te=Te/e; %Te [eV]
nearray(l)=ne;
Tearray(l)=Te;

%Thin Sheath Theory
    Ii_sat=min(Ismooth);
    Ie=Ismooth-Ii_sat;
    Vstart=phi_p-6;
    V3=phi_p-2;
    [~,cut2]=min(abs(Vsmooth-Vstart));
    [~,cut3]=min(abs(Vsmooth-V3));
    Ithin=Ie(cut2:cut3);
    Ithin=Ithin';
    Vthin=Vsmooth(cut2:cut3);
    lnIthin=log(Ithin);
    coeff3=polyfit(Vthin,lnIthin,1);
```

```
    Tethin=1/coeff3(1);
    nethin=-Ii_sat/e/A_p/exp(-.5)*sqrt(m_ar/Tethin/e);
    l_d=sqrt(e_o*Tethin/nethin/e);
    ratio=r_p/l_d;
    Tethinarray(l)=Tethin;
    nethin=-1*Ii_sat/(0.61*e*A_p*(kb*Tethin*11605/m_ar)^0.5);


%OML Theory
    IOML=Ismooth.^2;
    Vstart=-20;
    Vend=5;
    [~,cut12]=min(abs(Vsmooth-Vstart));
    [~,cut22]=min(abs(Vsmooth-Vend));
    VOML=Vsmooth(cut12:cut22);
    IOML=IOML(cut12:cut22);
    IOML=IOML';
    coeffo1=polyfit(VOML,IOML,1);
    slope=coeffo1(1);
    neOML=sqrt(-slope)*sqrt(m_ar/(2*e))*pi/(e*A_p);
    l_d=sqrt(e_o*Tethin/neOML/e);
    ratioOML=r_p/l_d;
    neOMLarray(l)=neOML;

%Calculate Ionization Frequency
if pos==centerp
    crosssections=load('Xe CS MATLAB.csv');
    energy=crosssections(:,1);
    crosssection=crosssections(:,2);
    dE=0.01;
    E=12.12984:dE:30;
    TK=Te*11605; %Electron temperature in kelvin
    csint=0;
    fi=f/e;
    for i=1:length(E)
        loe=log10(E(i));
        [b,m,n]=unique(V);
        eedf=interp1(b,fi(m),E(i),'pchip');
        cs=interp1(energy,crosssection,loe,'pchip');
        csint=csint+dE*e*cs*eedf*sqrt(2*E(i)*e/m_e);
    end
    ionfraction=0.2;
    ionfreq=ne*csint/ionfraction;
end

Vmin=0; Vmax=phi_p;
% plot
figure(4)
plot(V,F)
xlabel('E [eV]')
ylabel('F(e) eV^-^1 m^-^3')
axis([0,30,0,100])
axis 'auto y'
r=8*rand(1)-2;
i=length(V);
while V(i)<(r+5)
```

```
    i=i-1;
end
roundedpos=round((pos-centerp)*100)/100;
text(5+r,F(i),num2str(roundedpos),'HorizontalAlignment','left','VerticalAlign
ment','bottom','BackgroundColor',[.8 .8 .8],'Margin',1)
set([get(gca,'XLabel'),get(gca,'YLabel')],'FontSize',14)
hold all
end

figure
plot(positionarray,Tearray,'+')
xlabel('Position (cm)')
ylabel('Electron Temperature (eV)')
%title('Electron Temperature vs. Position')
set(gca,'FontSize',11)
set(get(gca,'XLabel'),'FontSize',14)
set(get(gca,'Ylabel'),'FontSize',14)
figure
plot(positionarray,nearray,'+')
xlabel('Position (cm)')
ylabel('Plasma Density (m^-^3)')
%title('Plasma Density vs. Position')
set(gca,'FontSize',11)
set(get(gca,'XLabel'),'FontSize',14)
set(get(gca,'Ylabel'),'FontSize',14)
figure
plot(positionarray,phi_parray,'+')
xlabel('Position (cm)')
ylabel('Plasma Potential (V)')
%title('Plasma Potential vs. Position')
set(gca,'FontSize',11)
set(get(gca,'XLabel'),'FontSize',14)
set(get(gca,'Ylabel'),'FontSize',14)
```

Emissive Probe Data Analysis

```
clear all
clc

%Load data file and preamble from oscilloscope
data=load(['033011_531_685_1.txt']);
preamble=load(['preamble1.txt']);

%Read in preamble data
xzero=preamble(1,1);
xincr=preamble(2,1);

yzero=preamble(3,1);
ymult=preamble(4,1);
yoff=preamble(5,1);

time=zeros(length(data),1);
voltage=zeros(length(data),1);
%Correct data file to voltage and time values using preamble data
for i=1:length(data)
```

```
    time(i)=xzero+xincr*i;
end

for i=1:length(data)
    voltage(i)=yzero+ymult*(data(i)-yoff);
end
voltage=10*voltage; %Correct for 10:1 divider.
plot(time,voltage)
title('Emissive Probe Voltage vs. Time')
xlabel('Time (s)')
ylabel('Voltage (V)')
set(gca,'FontSize',11)
set(get(gca,'XLabel'),'FontSize',14)
set(get(gca,'Ylabel'),'FontSize',14)

%Power spectral density estimate
Fs=500000;
NFFT = 2^nextpow2(length(voltage)); % Next power of 2 from length of y
Y = fft(voltage,NFFT)/length(voltage);
f = Fs/2*linspace(0,1,NFFT/2+1);

figure(3)
%Periodogram
periodogram(voltage,[],NFFT,Fs);
set(gca,'FontSize',11)
set(get(gca,'XLabel'),'FontSize',14)
set(get(gca,'Ylabel'),'FontSize',14)
pk=max(voltage)-min(voltage);
```

Appendix B LabVIEW Programs

Stepper Motor Serial Control

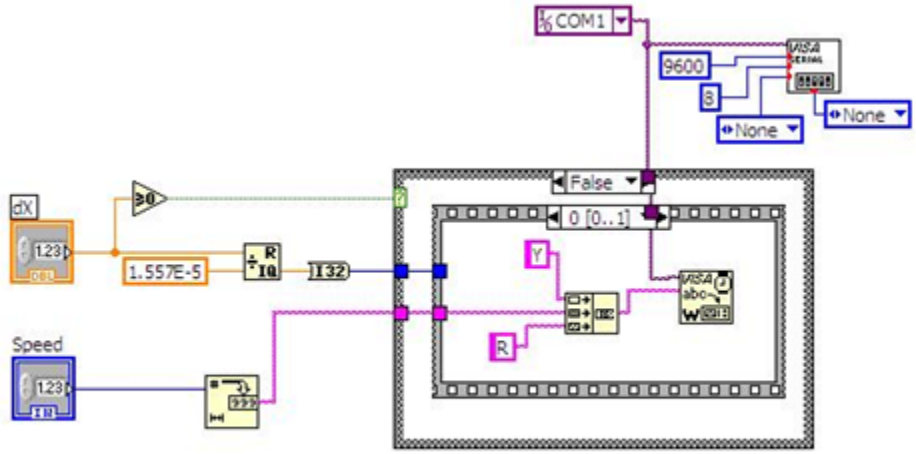

Read Langmuir Probe Data

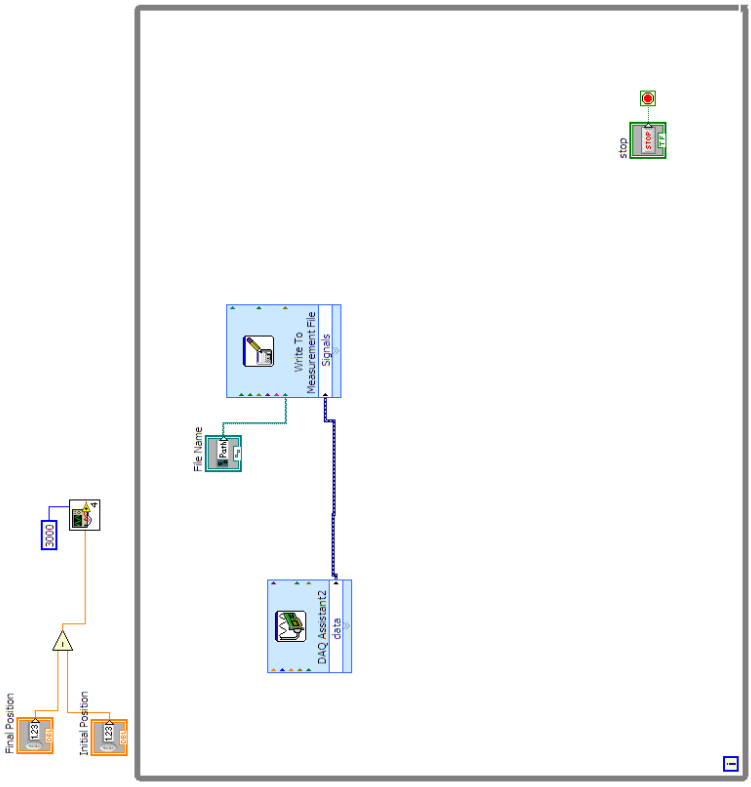

Read Oscilloscope Data